MASTERARBEIT / MASTER’S THESIS

Titel der Masterarbeit / Title of the Master’s Thesis

„Origin and age of the Carina young local association“

verfasst von / submitted by

Nora Wagner, BSc

angestrebter akademischer Grad / in partial fulfilment of the requirements for the degree of

Master of Science (MSc)

Wien, 2023 / Vienna, 2023

Studienkennzahl lt. Studienblatt / degree programme code as it appears on the student record sheet:	UA 066 861
Studienrichtung lt. Studienblatt / degree programme as it appears on the student record sheet:	Masterstudium Astronomie
Betreut von / Supervisor:	Dr. Núria Miret-Roig, MSc

Acknowledgements

During the course of this thesis, I was fortunate to receive invaluable advice and encouragement from individuals who hold a special place in my heart. I am immensely grateful to my supervisor, Núria Miret-Roig, for her unwavering support and guidance. Her dedication and willingness to engage in discussions about the project's progress at every stage of its development have been truly invaluable. I extend my heartfelt thanks for her valuable suggestions and for always offering guidance whenever I encountered stubborn obstacles, pushing me to persevere even when I doubted myself.
Moreover, I am deeply appreciative of the opportunity to undertake this project as a student within the esteemed research group led by João Alves at the Department of Astrophysics. Being a part of this team has provided me with firsthand experience in astronomical project work and exposed me to a highly motivated and supportive working environment. In particular, I want to express my gratitude to Sebastian for assisting me with the isochronal ages and to Efrem for always providing me with chocolate, brightening even the most challenging days.
Additionally, I would like to convey my deepest gratitude to my parents, whose unwavering support of my aspirations has been a constant source of strength. Their tireless encouragement and active involvement in my journey have meant the world to me.

Abstract

Ages of young local associations are crucial for understanding star and planet formation processes. However, they often still have significant uncertainties of up to 50%. The dynamical traceback method allows precise age estimates by using backward integration to determine the time of the closest spatial location of the members. Nevertheless, accurate 3D positions and velocities are crucial for the success of the traceback analysis. *Gaia* DR3 data provide precise 3D positions and 2D tangential motions, but uncertainties in *Gaia* radial velocities are still too large for an accurate orbital traceback analysis.
In this thesis, I use new high-precision radial velocity measurements from the UVES high-resolution optical spectrograph to determine the age and origin of the Carina young local association. I apply the dynamical traceback method to different samples of Carina members and integrate the current mean positions of Carina and 16 other nearby associations back in time to investigate potential common formation among them.
I determine an age estimate for the Carina young local association of $32.7^{+3.1}_{-1.9}$ Myr. Exploring the origin of nearby associations reveals two regions of star formation. One region includes younger associations connected to Scorpius-Centaurus, while the second region comprises Carina, Columba, Tucana-Horologium, and χ^1 Fornacis, which are suggested to share a common origin.
This outcome significantly advances the establishment of a self-consistent age scale for young local associations, relying on the 3D spatial motion of stars.

Kurzfassung

In den letzten 20 Jahren wurden einige junge Sternassoziationen in der solaren Umgebung entdeckt. Aufgrund ihrer Nähe und Jugend eignen sich diese hervorragend für die Erforschung von Stern- und Planetenentstehung. Um die frühen Prozesse der Sternentstehung besser zu verstehen, müssen die Eigenschaften dieser Assoziationen bekannt sein. Carina ist eine junge Sternassoziation, die sich etwa 75 pc von der Sonne entfernt befindet, deren genaues Alter jedoch bislang unbekannt ist. Es gibt Schätzungen, die von 13 bis zu 45 Myr reichen.

Um eine Altersbestimmung unabhängig von Sternentwicklungsmodellen zu ermöglichen, die besonders für junge Sterne oft unzuverlässig sind, verwende ich in dieser Arbeit eine Methode, bei der die Positionen der Sterne rückwirkend integriert werden, um den Zeitpunkt zu bestimmen, an dem die Sterne am engsten beieinander waren. Dies liefert eine Schätzung für das Alter der Assoziationen, da davon ausgegangen wird, dass die Sterne gemeinsam entstanden sind und sich im Laufe der Zeit voneinander entfernt haben. Die sehr präzisen astrometrischen Daten, die ich verwende, stammen aus der dritten Datenveröffentlichung der *Gaia* Mission. Um genaue Geschwindigkeitsberechnungen der Sterne zu ermöglichen, sind Radialgeschwindigkeiten erforderlich, die mit geringer Unsicherheit behaftet sind. Dies stellt eine große Herausforderung bei der Bestimmung des kinematischen Alters dar. Für diese Arbeit hat N. Miret-Roig neue Radialgeschwindigkeitsmessungen zur Verfügung gestellt, die aus Beobachtungen mit dem UVES-Spektrografen stammen. Einige der bereitgestellten Radialgeschwindigkeiten wurden auch unter Verwendung von archivierten Beobachtungen mit dem FEROS- oder dem HARPS-Spektrografen berechnet, wobei dieselbe Methode angewendet wurde.

Für diese Arbeit habe ich eine Kandidatenliste mit potenziellen Mitgliedern von Carina erstellt. Hierfür habe ich bestehende Kandidatenlisten, die aus den Untersuchungen von Gagné et al. (2018, 2018, und 2018c) und denen aus der kürzlich erschienen Studie von Kerr et al. (2022) hervorgehen, kombiniert.

Ich habe das kinematische Alter von Carina für drei verschiedene Ensembles potenzieller Mitglieder unter Verwendung verschiedener Assoziationsmaße bestimmt: 1) Sterne mit verfügbaren Radialgeschwindigkeiten von UVES+, 2) Sterne mit Radialgeschwindigkeiten von UVES+, *Gaia* DR3 oder APOGEE und 3) Sterne, die von Kerr et al. (2022) für ihre Berechnungen verwendet wurden.

Als endgültiges Ergebnis dieser Arbeit für die Altersbestimmung verwende ich das Ergebnis aus dem ersten Szenario, da dieses eine homogene Radialgeschwindigkeiten mit geringen Unsicherheiten bietet (der Median beträgt 0.4 km s^{-1}). Basierend auf diesen Überlegungen ergibt sich ein Alter für Carina von $32.7^{+3.1}_{-1.9}$ Myr. Außerdem habe ich die mittleren Positionen von Carina und 16 weiteren jungen lokalen Sternassoziationen zurückverfolgt, um festzustellen, ob einige von ihnen einen gemeinsamen Entstehungsort teilen. Dabei habe ich zwei Cluster von Sternentstehung erkannt. Der erste umfasst einige Assoziationen, die mit Scorpius-Centaurus in Verbindung stehen. Der zweite Cluster besteht aus Carina, Columba, Tucana-Horologium und χ^1 Fornacis.

Contents

Acknowledgements **i**

Abstract **iii**

Kurzfassung **v**

List of Tables **ix**

List of Figures **xi**

1. Introduction **1**
- 1.1. Young local associations 1
  - 1.1.1. Member identification of YLAs 3
  - 1.1.2. Carina 3
- 1.2. Age determination methods 5
  - 1.2.1. Lithium Evolution 5
  - 1.2.2. Isochronal fitting 6
  - 1.2.3. Gyrochronology 7
  - 1.2.4. Stellar activity 7
  - 1.2.5. Dynamical traceback method 8
- 1.3. Coordinate systems 9
  - 1.3.1. The *Gaia* mission 9
  - 1.3.2. Equatorial coordinates 9
  - 1.3.3. Galactic coordinates 10
  - 1.3.4. Galactic Cartesian coordinates 10
  - 1.3.5. Galactocentric coordinates 10
  - 1.3.6. Local Standard of Rest (LSR) frame 10

2. Data **13**
- 2.1. Compilation member literature 13
  - 2.1.1. Torres et al. (2008) 13
  - 2.1.2. Malo et al. (2013) 14
  - 2.1.3. Gagné et al. (2018a, b, and c) 14
  - 2.1.4. Schneider et al. (2019) 15
  - 2.1.5. Booth et al. (2021) 15
  - 2.1.6. Kerr et al. (2022) 16
- 2.2. Astrometry 16

2.3. Radial velocities . . . 17
2.3.1. UVES . . . 17
2.3.2. *Gaia* . . . 18
2.3.3. APOGEE . . . 18
2.3.4. Literature sources . . . 18
2.3.5. Comparison of radial velocities between different catalogs . . . 19
2.4. 6D phase space parameters . . . 20
2.4.1. Coordinate transformation . . . 21
2.5. Master table . . . 24

3. Methods **27**
3.1. Sample selection . . . 27
3.1.1. Quality selection . . . 27
3.1.2. Kinematic selection . . . 28
3.2. Orbit initialization and integration . . . 29
3.2.1. Galpy . . . 30
3.2.2. Orbit initialization . . . 30
3.2.3. Orbit integration . . . 31
3.3. Association size estimation and dynamical traceback age . . . 31

4. Results **37**
4.1. Dynamical traceback age with UVES+ RVs . . . 37
4.2. Dynamical traceback age with combined UVES, *Gaia*, and APOGEE RVs 39
4.3. Dynamical traceback age with the sample from Kerr et al. (2022) . . . 40
4.4. Isochronal ages . . . 42
4.5. Origin of the Carina association . . . 43

5. Discussion **55**
5.1. Comparison of results from this work . . . 55
5.2. Comparison with other studies . . . 56
5.3. Caveats . . . 57
5.4. Perspectives . . . 58

6. Conclusion **59**

Bibliography **61**

A. Appendix **69**
A.1. Master Table . . . 69

List of Tables

2.1. Precision in radial and tangential velocities. 21
2.2. Number of stars at each step of the selection process. 22
2.3. Dispersions in each direction of the present heliocentric Cartesian positions and velocities. 23
2.4. Mean present positions and velocities with errors. 23

4.1. Median of the age distributions 39
4.2. Dynamical age obtained with the robust metrics for the different samples 40
4.3. Summary of resulting ages. 41
4.4. Mean positions and heliocentric velocities of YLAS with their age estimates. 44

5.1. Literature age estimates for Carina. 58

A.1. Master Table 69

List of Figures

1.1. 2D projection on the Galactic plane of young associations in the solar neighborhood. From Gagné et al. (2018a). 2
1.2. Sky projection showing the distribution of YLA members in the celestial sphere. The Galactic plane is indicated by the gray region. From Gagné et al. (2018a). 4
1.3. Illustrative overview for the most common age determination methods. From Barrado (2016). 5

2.1. Histogram comparing the RVs from different catalogs. 20
2.2. Comparison of RV measurements from UVES+, *Gaia* DR3, APOGEE, and Literature sources. 21
2.3. Present heliocentric position distributions for stars with different RV sources. 24
2.4. Present heliocentric velocity distribution using different RV sources. 26

3.1. Histogram of Mahalanobis distance using UVES+ RV sample 34
3.2. Histogram of Mahalanobis distance using RV All sample 34
3.3. 2D projection of the orbits of Carina members integrated back in time. . . 35

4.1. Present heliocentric velocity and position distributions using UVES+ sample. 45
4.2. Present heliocentric velocity and position distributions using RV All sample. 45
4.3. Size estimation of the Carina YLA with the UVES+ RV sample 46
4.4. Size estimation of the Carina YLA with the RV All sample 46
4.5. Dynamical traceback age distribution with the UVES+ RV sample 47
4.6. Dynamical traceback age distribution with the RV All sample 47
4.7. Reconstruction of traceback result for Carina from Kerr et al. (2022) . . . 48
4.8. CMD for Carina with the UVES+ RV sample 49
4.9. CMD for Carina with the RV All sample 49
4.10. CMD for Carina stars from Kerr et al. (2022) sample. 50
4.11. Isochronal age estimates. 51
4.12. Orbits of young local associations 52
4.13. Orbits of YLAS with common origin 53

1. Introduction

The prevailing understanding is that most stars form within groups. However, numerous aspects of the star formation process remain shrouded in uncertainty. Accurate knowledge regarding the properties of stellar ensembles plays a crucial role in comprehending the intricate processes of star formation and evolution (e.g., Ambartsumian, 1947; Blaauw, 1964). Age is a fundamental parameter for characterizing all kinds of astrophysical objects, but it carries significant uncertainties and encounters various observational and theoretical challenges. Age determinations tend to be more precise for stellar associations compared to isolated stars. However, for stellar associations with ages below 150 Myr, the assigned ages can exhibit differences of up to 50% depending on the chosen technique (Soderblom, 2010).

In this introductory chapter, I introduce the concept of young local associations and highlight the Carina association. I continue with the most commonly employed methods for determining their ages and with an overview of the relevant coordinate systems in the context of this thesis.

1.1. Young local associations

Young Local Associations (YLAs) are aggregates of a few dozen young stars that are located within the solar neighborhood, typically within a distance of ~ 100 pc (Fernández et al., 2008). The members of these associations share dynamical properties, suggesting a common origin from the same molecular cloud, and therefore possess similar chemical properties (de Zeeuw et al., 1999; Jayawardhana, 2000). Identifying YLAs presents certain challenges as they typically do not exhibit significant overdensities in the surrounding field. They are only loosely bound and tend to disperse completely within several tens of Myr. The discovery of the first YLAs relied on combining astrometry data from the *Hipparcos* mission with observed X-ray emissions by the Röntgen Satellite (ROSAT) as young stars exhibit high levels of X-ray emission (Zuckerman and Song, 2004). Over the past two decades, numerous YLAs have been identified (Fernández et al., 2008), primarily due to the efforts of *Hipparcos* (Perryman et al., 1997) and other comprehensive surveys such as Tycho (Høg et al., 2000) and the Two Micron All Sky Survey (2MASS; Skrutskie et al., 2006). Figure 1.1 depicts the locations in the Galactic plane of the YLAs, where the cross resembles the location of the Sun.

Due to their proximity and their youth, the YLAs facilitate investigations into various aspects of stellar physics that rely on the early stages of stellar evolution. These include the study of stellar multiplicity, abundance patterns, rotation rates, and stellar activity levels (Torres et al., 2008). YLAs are also excellent candidates for direct detection of low-mass planets, studying circumstellar disks, and investigating mass functions (Schneider et al., 2019). Furthermore, stars in these associations offer optimal opportunities for studying planet formation and low-mass sub-stellar objects (Torres et al., 2008).

Recent improvements in observational techniques have greatly enhanced the precision of measurements. Notably, the *Gaia* mission has played an important role in providing highly accurate proper motion and parallax data. Furthermore, cutting-edge spectrographic instruments have significantly contributed to the acquisition of highly accurate radial velocity measurements. These developments enable us to accurately determine the positions, motions, and distances of stars, thereby facilitating investigations into the ages and origins of YLAs (Galli et al., 2023).

Figure 1.1.: 2D projection on the Galactic plane of young associations in the solar neighborhood. From Gagné et al. (2018a).

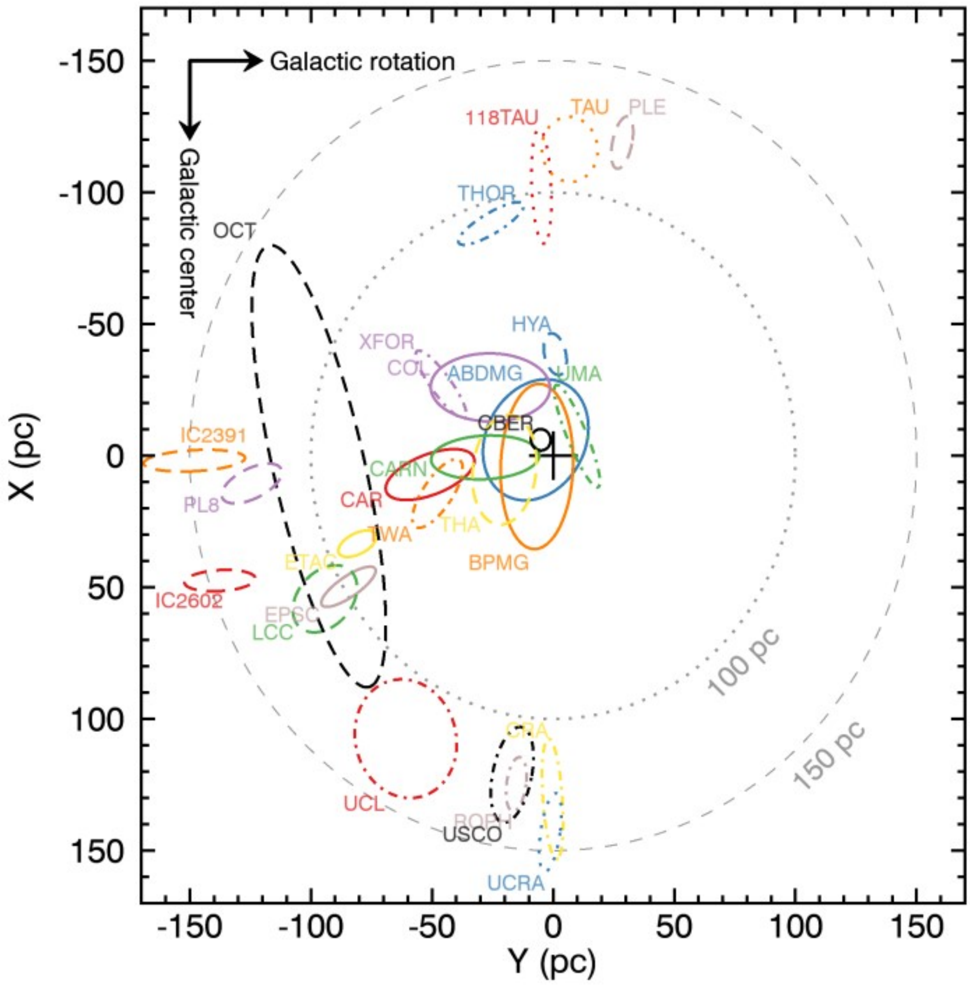

1.1.1. Member identification of YLAs

YLAs pose challenges in member selection due to projection effects caused by their proximity and because of their low density. Their wide coverage across the celestial sphere (see Figure 1.2) makes it difficult to use member selection criteria based solely on sky coordinates and photometry. However, as these associations have formed relatively recently and remain relatively unaffected by other stars in the Galaxy, their members exhibit similar space velocities and low velocity dispersions. This offers a potential method for identifying YLA members, albeit requiring the acquisition of reliable proper motions, parallaxes, and radial velocity measurements for individual stars to determine their complete kinematics. While accurate measurements of proper motion and parallax are now readily available, precise radial velocity measurements are often lacking. This limitation challenges the membership analysis of YLAs (Gagné et al., 2018a).

There are several methods available to identify members of YLAs using only their sky coordinates and proper motion, such as the convergent point tool (Torres et al., 2006), different goodness-of-fit metrics (Kraus et al., 2014), and the “good box” method (Zuckerman and Song, 2004). The convergence point method involves using the organized motion of stars towards a convergent point in the sky to identify genuine members of an association and distinguish them from field stars (Malo et al., 2013). The "good box" method involves selecting young stars for observation based on their kinematic properties, which are expected to fall within certain velocity ranges (Zuckerman and Song, 2004). The goodness of fit metrics assesses the similarity between observed properties of individual stars and the expected properties of association members, determining the likelihood of membership based on the level of agreement (Kraus et al., 2014).

Additionally, more advanced algorithms such as BANYAN, BANYAN II, BANYAN Σ, and LACEwING have been developed, which use Bayesian inference and model associations with unidimensional or tridimensional Gaussian distributions in the 6D phase space (Gagné et al., 2018a).

1.1.2. Carina

Through X-ray observations in the southern hemisphere with ROSAT and the utilization of kinematic information obtained from *Hipparcos*, (Torres et al., 2001) managed to detect the presence of the Great Austral Young Association (GAYA). Subsequent investigations of this association by Torres et al. (2008) revealed that it should be divided into at least three youthful associations: Tucana-Horologium, Columba, and Carina. These associations are believed to be closely connected and share a similar age, but they can be differentiated based on their velocity components.

Torres et al. (2008) used the ROSAT All-sky Survey catalog to propose the existence of 23 members of the Carina YLA located in the solar neighborhood, at a distance of approximately 75 pc from the Sun. Figures 1.1 and 1.2 from Gagné et al. (2018a) display

Figure 1.2.: Sky projection showing the distribution of YLA members in the celestial sphere. The Galactic plane is indicated by the gray region. From Gagné et al. (2018a).

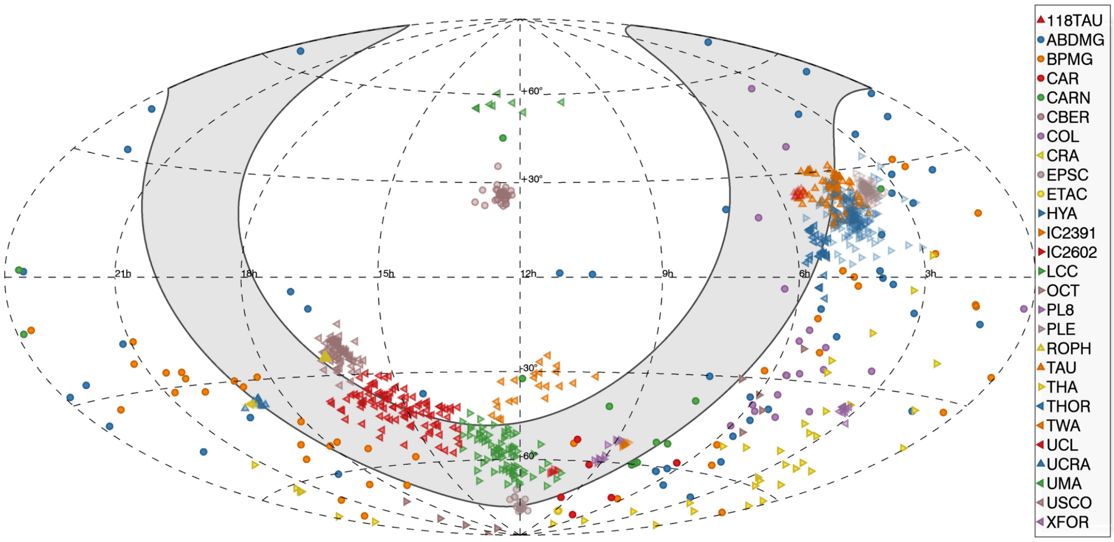

maps showcasing nearby young stellar associations, with Carina's location emphasized in red. The dispersion of the identified Carina members has given rise to ongoing debates regarding their membership status. There is a prevailing belief that numerous misidentifications have occurred, particularly with the nearby Tucana-Horologium and Columba associations (Kerr et al., 2022). Notably, the true membership of Carina remains a subject of contention. Gagné et al. (2018a) listed only seven confirmed members, compared to the 20 and 45 validated members of Columba and Tucana-Horologium, respectively.

The discovery of a protoplanetary disk around WISE J0808-6443 (Schneider et al., 2019) and the identification of substellar companions around some Carina members (such as HD 95086 and HD 44627) emphasize the need for a precise age determination of the association to accurately evaluate their mass and nature (planetary or brown dwarf) (Booth et al., 2021). However, the age of the Carina association remains poorly constrained, with estimates ranging from 13 to 45 Myr according to various studies (refer to Table 5.1 for an overview of the literature age estimates of Carina).

1.2. Age determination methods

The significance of determining the ages of YLAs has already been highlighted. Several methods can be employed for this purpose, with the most frequently utilized ones including lithium evolution, isochronal fitting, gyrochronology, stellar activity, and methods utilizing stellar kinematics like the dynamical traceback method. An illustrative overview of these methods, which I introduce in this section, is depicted in Figure 1.3.

Figure 1.3.: Illustrative overview for the most common age determination methods. From Barrado (2016).

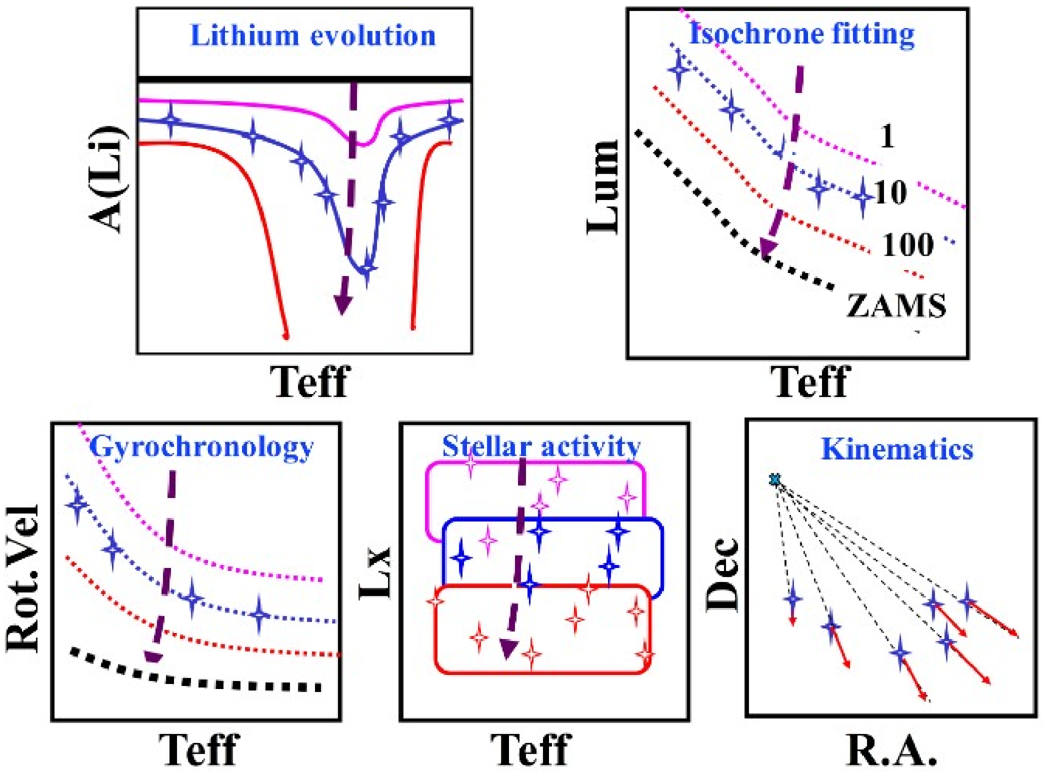

1.2.1. Lithium Evolution

Lithium can be used as an indicator of stellar age. This method relies on the fact that the abundance of lithium in a star's photosphere decreases over time as the star evolves. Stars with higher masses than $\sim 0.06\ M_{\odot}$ can attain central temperatures large enough to initiate lithium burning. When the core temperature of a star reaches $\sim 3 \times 10^6$ K, the process of lithium burning is triggered by the ^{7}Li(p,α)^{4}He reaction, causing the destruction and depletion of lithium. Once lithium burning begins, it rapidly exhausts all available lithium within a relatively short period (< 10 Myr). The onset of lithium burning in stars is influenced by their mass, with higher-mass stars initiating the process more rapidly compared to lower-mass stars. The core temperatures of lower-mass stars require a longer duration to surpass the threshold temperature for lithium burning (Zuckerman and Song, 2004).

By measuring the lithium abundance in a star's spectrum (6708 Å feature) and comparing it to theoretical models of lithium depletion, its age can be estimated (Soderblom, 2010). The upper left panel of Figure 1.3 shows an illustrative plot of Lithium abundance versus the effective temperature. If a star provides a high lithium abundance, it is likely to be young because not much time has passed for the lithium to be significantly depleted. Conversely, a star with a low lithium abundance suggests that it has had enough time to deplete a substantial portion of its original lithium content, indicating an older age (Barrado, 2016).

This method works well for young stars due to the ease of detecting and measuring the primary lithium feature at 6708 Å. In the case of pre-main sequence (PMS) stars, there is a clear trend of decreasing lithium abundance with age. On the contrary, the method is dependent on theoretical models and is highly sensitive to temperature variation. Additionally, other factors can influence the apparent lithium abundance, including PMS magnetic fields, starspots, or early phases of high mass loss (Soderblom, 2010).

A closely related approach, first proposed by Rebolo et al. (1992), uses the Lithium Depletion Boundary (LDB) for stellar age determination. This relies on the phenomenon that for low-mass stars even a small difference in mass can cause the Li 6708 Å absorption feature to appear or disappear as the initiation of lithium burning in low-mass stars is highly dependent on their mass (Zuckerman and Song, 2004).

The LDB approach allows an age estimate that is less dependent on stellar evolution models (Barrado, 2016). However, detecting the LDB requires precise spectral data of extremely faint objects (Soderblom, 2010). It is crucial to acknowledge that the age range applicable to the LDB method is constrained to $\sim 20 - 450$ Myr as a result of both physical limitations and observational constraints (Barrado, 2016).

1.2.2. Isochronal fitting

A very commonly used approach to estimate the ages of stellar aggregates is using their location in the color-magnitude diagram (CMD) or in a Hertzsprung-Russell Diagram (HRD) and comparing it with isochrones, which are derived from stellar models and represent constant age curves (schematically illustrated in the top right panel of Figure 1.3) (Zuckerman and Song, 2004). The computed set of model isochrones can be compared to the observed data using visual evaluation, regression tools, or more sophisticated fitting techniques, such as Bayesian inference (Soderblom, 2010; Ratzenböck et al., 2023). To achieve a strong alignment between the model and the observed data, it is important to accurately capture the evolutionary processes spanning all ranges of stellar mass

(Soderblom, 2010).

The method is extensively employed due to its broad applicability across all age and mass ranges (Galindo-Guil, F. J. et al., 2022). Another advantage of model isochrones, contributing to their widespread adoption, is that they can be easily computed due to the large availability of open-source codes such as PARSEC (Bressan et al., 2012; Marigo et al., 2017) and MIST (Choi et al., 2016; Dotter, 2016). A large caveat of isochronal ages is that they are dependent on evolutionary models. There can be significant differences in the obtained ages depending on the employed model (Binks et al., 2022). When the models' completeness or accuracy is insufficient, the process of isochrone fitting can result in systematic errors in the age estimates (Soderblom, 2010). The selection of the fitting technique is another source of systematic uncertainty since they are associated with different assumptions regarding the underlying data distribution of the measurements (Ratzenböck et al., 2023). Additionally, sources of observational errors influence the determined age estimate. These include the accuracy and completeness of the photometry, contamination from field stars, and the impacts of factors such as metallicity, distance, and extinction (Soderblom, 2010).

1.2.3. Gyrochronology

Gyrochronology is an empirical method used to determine the age of stars by studying the evolution of their spin rate. This technique is based on the observed phenomenon that stars gradually lose angular momentum as they age (indicated in the left bottom panel of Figure 1.3). However, there are aspects of angular momentum loss that are poorly understood, especially regarding PMS and ZAMS stars (Barnes, 2007; Soderblom, 2010).

One of the benefits of the technique is that obtaining rotation periods with high levels of precision and accuracy is feasible and that they are not prone to significant variability. On the contrary, it is only well applicable to solar-type stars older than 500 Myr and younger than the Sun. Additionally, when comparing the distributions of rotational periods with mass among different coeval clusters, significant variations become apparent. Hence, there may be additional factors that should be taken into consideration (Soderblom, 2010).

1.2.4. Stellar activity

Another empirical method for estimating the age of stars relies on the observed decline of stellar activity over time, which is closely linked to their rotation. Stellar activity is a complex and variable process, and several indicators can be used to assess it. These indicators include X-ray emission from the corona, as well as Hα, M II h and k, and Ca II H and K emission from the chromosphere. The middle bottom panel of Fig 1.3 indicates the decrease of coronal activity with age (Zuckerman and Song, 2004; Soderblom, 2010; Barrado, 2016).

This method offers the advantage of utilizing readily observable indicators of stellar activity with a wide range of available datasets. However, it is less effective when applied to very young or old stars. While analyzing a group of stars in an association can provide meaningful results, caution must be exercised when applying this method to individual objects, ideally in conjunction with other age estimation techniques (Soderblom, 2010).

1.2.5. Dynamical traceback method

The concept of dynamical ages builds upon the work of Ambartsumian (1947) and Blaauw (1964) and is based on the understanding that stars form together and gradually disperse from their birthplace over time. The age of the stars can be estimated by identifying the time when the stars were most concentrated. To determine this time, the positions and motions of the stars need to be traced back in time (indicated in the bottom right panel of Figure 1.3). Various methods have been employed in the literature to achieve this, including linear trajectories, epicyclic approximation, and orbital integration using a Galactic potential. Additionally, different criteria have been adopted to define the size of a stellar association, which is necessary to quantify the level of concentration. Commonly used size estimators include the standard deviation of positions in a specific direction or 3D, the maximum distance between members, the median mutual distance, and pairwise encounters (Fernández et al., 2008; Ducourant et al., 2014; Mamajek and Bell, 2014; Riedel et al., 2017; Miret-Roig et al., 2018; Miret-Roig et al., 2020; Kerr et al., 2022).

The utilization of kinematics to estimate stellar ages offers several advantages. Firstly, this approach is independent of evolutionary models, and the resulting ages are not influenced by variability or extinction (Miret-Roig et al., 2020). Moreover, this technique is applicable to stars across all mass ranges and can even be used for stellar associations younger than 20 Myr, which presents a challenge for many other age-determination methods. However, the reliability of dynamical ages diminishes for old stars, as their trajectories may have been disrupted by interactions with massive objects in the Galaxy (Soderblom, 2010). The accuracy of dynamical traceback ages relies on precise measurements of 3D positions and velocities, which in turn require high-quality astrometric and radial velocity data. While precise proper motion and parallax measurements are now widely available with the third data release of *Gaia*, radial velocities can still introduce uncertainties. The primary limitations of this method include the need for precise radial velocity measurements, the development of a systematic approach to select kinematic members, and a statistically robust approach for estimating the size of stellar associations (Miret-Roig et al., 2020; Galli et al., 2023).

Recent investigations conducted by Miret-Roig et al. (2020) and Galli et al. (2023) have successfully estimated the ages of the β Pictoris and Tucana-Horologium associations, demonstrating the possibility of obtaining accurate dynamical age estimates by addressing the limitations associated with this method. These findings motivate further exploration of additional YLAs, aiming to establish a comprehensive and internally consistent age scale for young stellar associations.

1.3. Coordinate systems

In order to conduct a dynamical traceback investigation involving 3D positions and velocities, a combination of astrometric data and radial velocities is required. This section introduces the *Gaia* mission, which serves as the source of astrometric data for this thesis, as well as the relevant coordinate systems used in this context.

1.3.1. The *Gaia* mission

The *Gaia* space-astrometry mission was launched in 2013 by the European Space Agency (ESA) and is operating at the second Lagrange point of the Sun-Earth-Moon system. Initially, its nominal mission was planned to last for five years (Gaia Collaboration et al., 2016), but it has already been extended until the end of 2025[1]. The *Gaia* satellite is the successor to *Hipparcos*, and its main aim is to create a 3D space and velocity map of more than one billion stars in the Milky Way and to deduce their astrophysical characteristics. By doing so, *Gaia* provides detailed information on stellar evolution and physics, star formation, stellar variability, the distance scale, multiple stars, exoplanets, solar system bodies, unresolved galaxies and quasars, and fundamental physics. The ultimate goal of the mission is to examine the structure, origin, and evolution of the Milky Way. *Gaia* data can be accessed from the Gaia archive, which contains multiple intermediary data releases (Gaia Collaboration et al., 2016). The latest is the *Gaia* DR3, which is based on data collected over 34 months of observation and was published in 2022. Its most prominent enhancements are a greatly expanded radial velocity coverage and an exceptionally detailed astrophysical characterization of *Gaia*'s sources. The number of sources covered by *Gaia* DR3 (almost two billion), along with their spatial coordinates, proper motions, parallax measurements, and a collection of wide-spectrum photometry data, captured in the G, GBP, and GRP pass-bands, are identical to those already available in the prior *Gaia* EDR3 (Gaia Collaboration et al., 2022). For this thesis, the most relevant information from the *Gaia* DR3 is the high-precision 5-parameter astrometry.

1.3.2. Equatorial coordinates

Astrometric measurements are commonly expressed using the equatorial coordinate system. This system is based on projecting Earth's equator onto the celestial sphere and serves as a spherical coordinate system with its center in the Earth. In the equatorial frame, the 6D phase space is defined by the following parameters: (ra), declination (dec), distance (d), proper motion (pmra and pmdec), and radial velocity (RV). Right ascension is measured along the celestial equator from the vernal equinox, while declination is measured north or south of the celestial equator. The distance parameter represents the object's radial distance, which is connected to the parallax measurement. Proper motion provides information about an object's transverse velocity perpendicular to the line of sight, while radial velocity describes the component of their motion along the line of sight.

[1] `https://www.cosmos.esa.int/web/gaia/news`

1.3.3. Galactic coordinates

In the Galactic coordinate system, the Galactic plane serves as the equator, while the pole aligns with the Galactic pole. This heliocentric coordinate system utilizes axes pointing towards the Galactic center, the Galactic rotation, and the north Galactic pole. Within this framework, the 6D phase space encompasses several components: Galactic longitude (l), Galactic latitude (b), distance (d), Galactic proper motion (pm$l$ and pm$b$), and RV.

1.3.4. Galactic Cartesian coordinates

We can obtain a Galactic Cartesian 6D representation from the Galactic coordinates via coordinate transformation. This representation consists of the 3D spatial components X, Y, and Z (pc), as well as the 3D velocity components U, V, and W (km s^{-1}). In this representation, X and U point towards the Galactic center, Y and V point in the direction of Galactic rotation, and Z and W point towards the north Galactic pole.

1.3.5. Galactocentric coordinates

The Galactocentric coordinate system is centered to the center of the Milky Way $(l, b) = (0°, 0°)$. In contrast to the equatorial and the Galactic coordinates, the IAU provides no definition for a Galactocentric coordinate system. I utilize the definition employed in the python package `Astropy` (Astropy Collaboration et al., 2013). In spherical and cylindrical coordinates, this coordinate system includes the parameters: R, representing the radial distance from the object to the Galactic center; v_R, denoting the radial velocity along the line connecting the object to the Galactic center; v_T, which characterizes the tangential velocity perpendicular to the line connecting the object to the Galactic center; z, indicating the distance from the object to the Galactic midplane; v_z, representing the vertical velocity perpendicular to the Galactic plane; and ϕ, the azimuthal angle that describes the object's angular position within the galactic plane.

1.3.6. Local Standard of Rest (LSR) frame

The local standard of rest (LSR) is a reference frame to describe the motion of stars in the Milky Way. The LSR is defined as the hypothetical perfectly circular motion of a star located at a particular point in the Milky Way called the solar apex. The solar apex is the direction in which the Sun is moving relative to the stars in its immediate vicinity. The determination of the LSR involves measuring the average 3D motion of nearby stars, which requires proper motion and radial velocity measurements of the stars.

There are various measurements of the velocity of the LSR. This thesis considers the one of Schönrich et al. (2010). The authors used a Bayesian statistical method to analyze the available data on the positions and velocities of stars in the Milky Way, including data from the *Hipparcos* and Tycho-2 catalogs. They found that the LSR has a velocity of $U = 10.00^{+0.36}_{-0.36}$ km s^{-1} towards the Galactic center, $V = 5.25^{+0.62}_{-0.62}$ km s^{-1} in the direction of Galactic rotation, and $W = 7.17^{+0.38}_{-0.38}$ km s^{-1} towards the North Galactic

Pole. These values for U, V, and W provide a reference frame for measuring the motion of other stars in the Milky Way. By subtracting the motion of the LSR from the observed motion of a star, we can establish the star's true motion relative to the Milky Way.

Schönrich et al. (2010) noted that their solution for U, V, and W is consistent with previous determinations, but there is still some uncertainty in the values due to limitations in the available data. However, their analysis provides a robust and up-to-date estimate of the motion of the LSR.

2. Data

In this chapter, I present a comprehensive overview of the member selection process for the sample. This is followed by a detailed outline of the collected astrometric and radial velocity data used to determine the 6D phase space coordinates.

2.1. Compilation member literature

The census of Carina members used for this thesis is based on the Carina candidate members from Kerr et al. (2022). Their member list for Carina, which consists of 110 stars, is a combined literature sample. It contains 23 proposed Carina members from the catalog of Torres et al. (2008), which was later extended by Malo et al. (2013), where among others, 6 Carina member candidates were identified by applying a Bayesian identification tool. To improve the completeness among fainter stars, they further used the collection from Gagné et al. (2018a), Gagné et al. (2018b), and Gagné and Faherty (2018), which applied the BAYNAN Σ algorithm for membership investigation. In addition, they used the outcome from Schneider et al. (2019), which utilized the same algorithm but used new spectroscopic observations. Furthermore, they included a supplementary sample from Booth et al. (2021), which extends the sample by 4 Carina members not identified elsewhere.

2.1.1. Torres et al. (2008)

Torres et al. (2008) generated a candidate list of potential members of nine kinematically well defined loose young associations in the solar neighborhood, one of which is Carina. The paper is part of the SACY (Search for Associations Containing Young Stars) project. SACY focused on systematically examining the counterparts of ROSAT all-sky X-ray sources in the Southern Hemisphere, identifying sources with determined proper motions. The SACY sample incorporates 1626 spectroscopically observed stars in the Southern Hemisphere (i) that have a spectral type later than G0 to utilize the Li λ6707 line as a youth indicator, (ii) that are listed in the TYCHO-2 or *Hipparcos* catalogs guaranteeing the availability of proper motions, and (iii) that are potential optical counterparts of sources from the ROSAT All-Sky Bright Source Catalog. Their approach for identifying members of young associations using information from the SACY sample involves utilizing the convergence method and a membership probability model that both analyze stars in the heliocentric 6D phase space space. Utilizing the convergence method, kinematical distances for individual stars can be derived within a 6D space, particularly when precise trigonometric measurements are not attainable. This iterative process enables the identification of a list of potential candidates. The probability model (k-NN model) was trained using the generated candidate list, where 6D spheres were defined around each star to determine membership probability based on the proportion of stars within these spheres belonging to the training set. A cutoff probability was established for each association to identify probable members. By repeating the convergence method using this updated list, the researchers sought to match the two lists and consider kinematically selected members as potential candidates. These candidates were further evaluated by comparing their Li content with the expected Li depletion for their age. Applying this methodology resulted in identifying 23 potential members of the Carina association, with all but one (HD 107722) being covered by SACY observations. The members include 3 stars previously identified as Tucana-Horologium members, including AB Pic, which hosts a low-mass companion at the brown dwarf/planet boundary. Furthermore, the proposed members incorporate two double-line spectroscopic binary stars, CD-53 2515 and HD 83096.

2.1.2. Malo et al. (2013)

To identify high probability, low-mass members of seven YLAs, Malo et al. (2013) used a method based on Bayesian analysis. The examination considers at least the star's position, proper motion, magnitude, and color, but it is possible to include other measurements, such as radial velocity and distance. As an initial sample for identifying new low-mass Carina members, they used the observational properties of 5 bona fide members proposed by Torres et al. (2008). They created kinematic models describing the respective associations. They generated virtual stars with UVW velocities and dispersions for a particular group and location in the sky. The kinematic model uses the mean and distribution of these UVW velocities to anticipate the mean tangential velocity with its dispersion. This predicted tangential velocity and the assumed distance are used to compute the predicted proper motion, which they compared to the observed proper motion of potential new low-mass members. These low-mass stars originate from a sample of Riaz et al. (2006) consisting of stars exhibiting X-ray and Hα emissions with spectral types ranging from K5V to M5V. So, based on a set of observables (I_c and J magnitudes, amplitude of proper motion in ra and dec), stars potentially belonging to a YLA were selected, and a membership probability and statistical distance were obtained for each star and association. The authors established a threshold of 90% for membership probability to classify a candidate as a high-probability member of a specific group. This investigation yielded a set of 6 new highly probable low-mass Carina members.

2.1.3. Gagné et al. (2018a, b, and c)

To identify members of YLAs within 150 pc of the Sun, including Carina, the authors utilize the new Bayesian algorithm BANYAN Σ (Bayesian Analysis for Nearby Young AssociatioNs). The algorithm can calculate membership probabilities for objects based on sky coordinates and proper motion while incorporating additional measurements such as parallax, radial velocity, and spectrophotometric distance constraints. BANYAN is built upon the work of Malo et al. (2013) for modeling with unidimensional Gaussian distributions in 6D Galactic Cartesian coordinates. Subsequently, BANYAN II introduced the modeling of associations as freely rotating 3D Gaussian ellipsoids in position and velocity space (Gagné et al., 2014). The algorithm got further improved in the form of BANYAN Σ by updating and refining models of YLAs and employing complete 6D multivariate Gaussians. Notably, it outperforms other moving group tools in the literature, particularly in terms of mitigating cross-contamination between young associations. The models for the YLAs in Gagné et al. (2018a) use data from the *Gaia* DR1, in Gagné et al. (2018b) from *Gaia*-Tycho, and in Gagné and Faherty (2018) from *Gaia* DR2. These publications provide a revised catalog of confirmed members for Carina and other nearby young associations. Combining these catalogs, the resulting member list for Carina comprises 88 stars, with 7 originating from Gagné et al. (2018a), 4 from Gagné et al. (2018b), and 77 from Gagné and Faherty (2018).

2.1.4. Schneider et al. (2019)

Schneider et al. (2019) searched in ten nearby YLAs for new low-mass members. Therefore, they created a set of high-resolution optical spectra observed with HIRES, ESPaDOnS, MIKE, and the Echelle Spectrograph. The available measurements encompass radial velocities and age diagnostics such as Hα and Li λ6707 equivalent widths. They merged the radial velocities with astrometry obtained from *Gaia* DR2 to calculate complete $XYZUVW$ kinematics for the entire sample. To assess potential membership in nearby associations, they utilized the measured spectroscopic youth information together with other age indicators (such as X-ray, UV fluxes, and positions on the CMD) and kinematics. To calculate the likelihood of membership, they also used the BANYAN Σ algorithm from Gagné et al. (2018a). If an object had a BANYAN Σ probability of more than 1% for a particular association, they considered it for potential membership. However, only because a star's kinematics match a specific association, it does not necessarily have to be a genuine member, as kinematic interlopers of different ages can occur. Therefore, the authors determined the age of a star using CMDs and Lithium abundances to provide consistency with the age of any matching group. By employing this methodology, they identified one previously unrecognized Carina member, reassigned two stars that were previously attributed to other associations, and confirmed the membership of eight stars that had already been considered as potential candidates in prior investigations.

2.1.5. Booth et al. (2021)

Booth et al. (2021) stated that since not many stars could have been confirmed to be Carina members yet, they aim to study the membership of Carina using *Gaia* DR2 data. Therefore, they applied the BANYAN Σ code from Gagné et al. (2018a) to an initial collection of members from Malo et al. (2013), Moór et al. (2013), Malo et al. (2014), Elliott, P. et al. (2015), Silverberg et al. (2016), Gagné et al. (2018a), Gagné et al. (2018b), Gagné and Faherty (2018), and Schneider et al. (2019). To collect the more recent position and velocity data, they cross-matched the coordinates of all potential members with the *Gaia* database. They took measurements from other sources for stars without available

Gaia DR2 RV measurements. They obtained 6D position and velocity information and provided it to BANYAN Σ for determining the association membership probabilities. When stars turned out to have a membership probability $> 50\%$, they were acknowledged as members. Their candidate list for Carina contains 26 stars, of which Kerr et al. (2022) incorporated all not already included in their list.

2.1.6. Kerr et al. (2022)

Kerr et al. (2022) compiled an initial member selection from the sources mentioned above. To this selection, they applied the HDBSCAN (Hierarchical Density-Based Spatial Clustering of Applications with Noise) clustering algorithm in combination with the EOM (excess of mass) clustering method. The HDBSCAN algorithm employs a parameterized density metric to detect overdensities, which relies on measuring the distance to the kth nearest neighbor. In contrast to other clustering algorithms that often rely on assumptions about density thresholds, shapes, or specific cluster properties, HDBSCAN stands out by utilizing only a minimum cluster size and a parameter that influences the smoothing of the density distribution. HDBSCAN offers two options for cluster selection: "leaf" and "EOM," with EOM clustering generally preferred. The EOM option identifies the most persistent clusters from the clustering tree. Through this clustering process, Kerr et al. (2022) reclustered the initial member selection, resulting in a redefined set of 101 stars for the Carina YLA.

2.2. Astrometry

The proper motion and parallax measurements of Carina members considered in this work are sourced from the *Gaia* DR3 catalog. This catalog provides the most recent and accurate astrometric measurements for the stars under consideration. All 118 Carina candidates have complete 5D data from the *Gaia* DR3 archive. The median astrometric errors for proper motion and parallax are 0.025 mas yr^{-1} and 0.02 mas, respectively. These values are propagated to the calculation of the median uncertainty in tangential velocity, which equals 0.03 km s^{-1} (refer to Table 2.1). The tangential velocity (V_{tan}) is determined using the formula:

$$V_{tan} = \frac{k\mu}{\pi} \tag{2.1}$$

where $\mu = \sqrt{pm_{RA}^2 + pm_{DEC}^2}$ represents the proper motion measured in mas yr^{-1} and π denotes the parallax in mas. The conversion factor $k \approx 4.74$ ensures that the resulting unit is km s^{-1}. To compute the errors associated with V_{tan} and μ, it is possible to propagate the errors and correlations of the astrometric variables.

2.3. Radial velocities

Given the excellent precision in tangential velocities, it is crucial to have RVs of equally high quality. In this section, I present various catalogs that provide RVs for the Carina association. Out of the 118 candidate members identified in Carina, 90 stars (76%) have been subjected to at least one RV measurement. Table 2.1 provides an overview of these sources with the corresponding measurement errors.

2.3.1. UVES

The UVES (Ultraviolet and Visual Echelle Spectrograph) spectrograph (Dekker et al., 2000) is installed on the Very Large Telescope (VLT) at the European Southern Observatory (ESO) in Chile. UVES is located at the Nasmyth B focus of UT2 and was designed to operate in the ultraviolet and visible wavelength ranges, covering a wide spectral range from 300 to 1100 nm. The spectrograph utilizes an echelle grating and offers high-resolution capabilities, reaching resolving powers of up to 110,000.

A dedicated proposal, initiated by my supervisor with ID 109.232D, led to spectroscopic observations being conducted for 24 stars. These observations required 15.1 hours of observing time.

The RVs were derived by applying the methodology described in Miret-Roig et al. (2020) to the observed spectra. For twenty out of the 24 stars, the pipeline was successful in obtaining reliable RV measurements. The remaining stars either exhibited binary behavior, had rapid rotation resulting in broad spectral lines and poor RV determination, or encountered other issues with the spectrum.

Furthermore, the RV sample was extended by including raw spectra from older archives, which allowed us to collect an additional nine RV measurements from data from the Fiber-fed Extended Range Optical Spectrograph (FEROS) and the High Accuracy Radial Velocity Planet Searcher (HARPS) spectrographs. As a result, we have RV information for a total of 29 out of the 88 selected Carina members, which were initially identified as candidates in Gagné et al. (2018a), Gagné et al. (2018b), and Gagné and Faherty (2018) (BANYAN sample in Table 2.2).

Significantly, within the observed stars, four of them stand out as their RV measurements were exclusively obtained from the UVES+ observations, as no RV data is accessible from *Gaia* DR3 or any other sources. In *Gaia* DR3, these stars are identified by the following identifiers: 4651909078695070848, 5258513835596515328, 5252895434280467072, and 5240144982036017536. Consequently, these recent observations mark the first RV measurements for these particular stars.

2.3.2. *Gaia*

The *Gaia* DR3 catalog (Gaia Collaboration et al., 2022) provides an extensive dataset, including RV measurements, for approximately 33.8 million sources with a limiting magnitude of $G_{RVS} \leq 14$ mag. The catalog encompasses a wide range of effective temperatures, spanning from 3100 K to 14500 K, and also incorporates low signal-to-noise spectra that cover all spectral types. The uncertainties associated with the RV measurements display variation, with values less than 1 km s^{-1} for bright stars and a few km s^{-1} for others. It should be noted that the uncertainties for bright stars might be slightly underestimated.

Out of the 118 Carina candidates, *Gaia*DR3 provides RV measurements for 80 of them. However, this set of RV measurements exhibits a relatively large median error of 2.7 km s^{-1} when compared to measurements obtained from other sources (refer to Table 2.1).

2.3.3. APOGEE

The Apache Point Observatory Galactic Evolution Experiment (APOGEE) is a homogeneous spectroscopic survey conducted by the Sloan Digital Sky Surveys (SDSS), which has been scanning the sky since 1998. The SDSS has already accomplished four operational phases, while the fifth phase is underway (Abdurro'uf et al., 2022). APOGEE aims to study the chemical and dynamical properties of stars in the Milky Way. The spectrograph has been collecting data on the Sloan Telescope since 2011. The APOGEE survey uses high-resolution ($R \approx 22,500$) infrared ($1.5 - 1.70$ μm) spectroscopy to obtain the spectra of stars and determine detailed information about their chemical compositions, temperatures, and radial velocities. The RVs deduced from the APOGEE instrument are very precise, having uncertainties of 0.07 km s^{-1} for $S/N > 20$ (Majewski et al., 2017).

I performed a cross-matching analysis between our compiled list of Carina members and the latest APOGEE data release (D17). This analysis resulted in the identification of 10 stars with highly accurate RV measurements. The median error for these measurements is 0.1 km s^{-1}.

2.3.4. Literature sources

To obtain a literature sample of RV measurements, I combined the sample of RV measurements from Kerr et al. (2022) with the SIMBAD archive.

SIMBAD (Set of Identifications, Measurements, and Bibliography for Astronomical Data) (Wenger et al., 2000) is a reference database of astronomical objects maintained by the Centre de Données astronomiques de Strasbourg (CDS), which consists of several million identifications, "basic data", bibliographical references, and selected observational measurements. It provides information on stars, galaxies, and other celestial objects, including their coordinates, magnitudes, spectral types, and other properties. SIMBAD provides

RV measurements from various sources. The Observatoire de Marseille has collaborated to compile stellar RV data.

By merging our Carina member sample with the data from SIMBAD, I obtained a heterogeneous set of RV measurements for 39 Carina members. Among these measurements, five lack information about uncertainties.

The sample of Kerr et al. (2022) consists of 49 measurements collected from various literature sources, excluding *Gaia* DR3. The RV measurements used in Kerr et al. (2022) originated from the following sources: Torres et al. (2006) (T6), Casagrande, L. et al. (2011) (C11), Lopez Martí, B. et al. (2013) (L13), Moór et al. (2013) (Mo13), Malo et al. (2013) (M) Elliott, P. et al. (2014) (E), Malo et al. (2014) (M14), Gagné and Faherty (2018) (13), Soubiran, C. et al. (2018) (S18), and Schneider et al. (2019) (S). Out of the 49 literature RVs, seven do not have accessible errors.

The combination of these two samples resulted in a Literature RV sample consisting of 49 stars, with a median RV error of 0.5 km s^{-1} (see Table 2.1). To determine the most accurate measurements for each star, I prioritized the measurement with the lower error whenever both sources provided measurements. In cases where one of the measurements lacked a reported error, I selected the one with an associated error. If none with an error was available, I omitted the selection altogether.

2.3.5. Comparison of radial velocities between different catalogs

The histogram in Figure 2.1 displays the distribution of RVs for Carina members sourced from multiple catalogs. It is evident that the RVs derived from *Gaia* exhibit the highest dispersion, but they also provide the highest number of measurements. Conversely, the RV measurements from other sources display greater concentration, indicating better precision. Notably, APOGEE offers only a few RV measurements but with remarkable accuracy. However, despite the overall high precision of the RV measurements obtained from UVES+, as evidenced by the median error of 0.4 km s^{-1}, the presence of a few outliers suggests the existence of imprecise measurements. Therefore, I will employ a sampling strategy to address this issue.

Figure 2.2 compares the new RVs measured with the UVES spectrograph and previous RVs from *Gaia* DR3, APOGEE, and literature. The newly obtained RVs are plotted along with their respective errors against the same RV values subtracted by the corresponding *Gaia* RVs of the stars.

The comparison of our sample with *Gaia* DR3 includes observations of 25 out of the 29 stars; as for four stars, we provide the first radial velocity measurement. Stars with very different RV measurements are spectroscopic binary candidates or simply indicate that at least one of the measurements is highly imprecise. In both cases, the radial velocity is inconvenient for a precise traceback analysis. Hence, all stars with a difference in RV

Figure 2.1.: Histogram comparing the RVs from different catalogs.

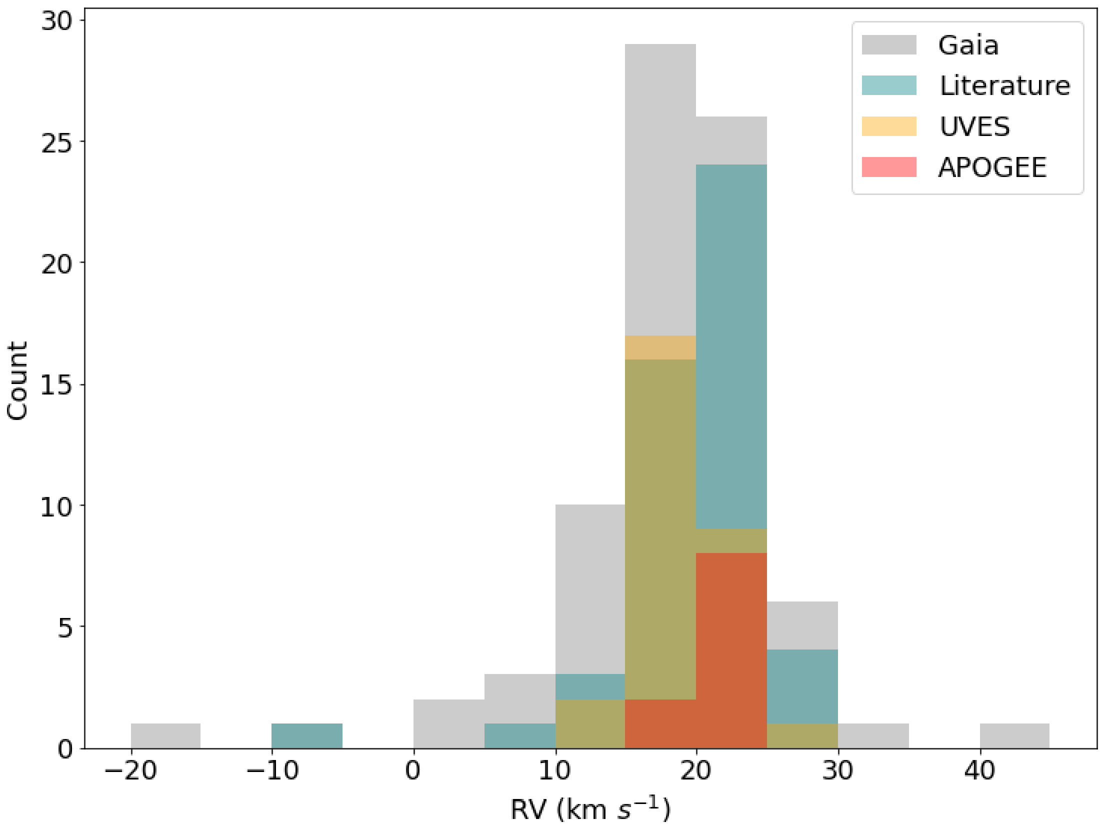

greater than 3 times the combined error are rejected.

Table 2.1 compares the median uncertainties in tangential velocities to the median RVs of different catalogs. It is visible that, except for the very high-precision measurements from APOGEE, the new RVs from UVES+ have the lowest uncertainties.

2.4. 6D phase space parameters

Gaia revealed the intricate nature of associations and star-forming regions in terms of their spatial and kinematic structures. The 6D phase space provides the most suitable representation space to disentangle the spatial and kinematic structure, as it circumvents issues such as projection effects (Miret-Roig et al., 2022).

Table 2.1.: Precision in radial and tangential velocities.

	# Members	Median RV error (km s^{-1})	Median V_{tan} error (km s^{-1})
Members CAR (5D)	118		0.03
UVES+ (6D)	29	0.4	
Gaia DR3 (6D)	80	2.7	
APOGEE DR17 (6D)	10	0.1	
Literature (6D)	49	0.5*	

Notes. The tangential velocity errors are obtained with the *Gaia* DR3 parallaxes and proper motions, taking into account the correlations among the astrometric parameters. (*) Heterogeneous sample. It may contain systematic discrepancies across various studies.

Figure 2.2.: Comparison of RV measurements from UVES+, *Gaia* DR3, APOGEE, and Literature sources.

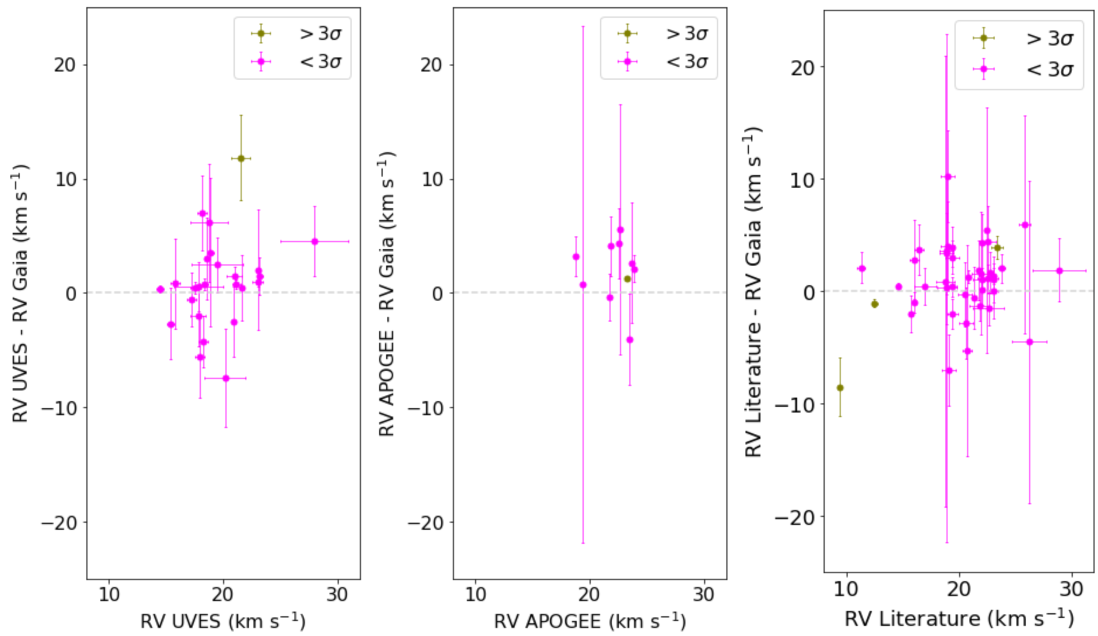

Caption/Notes. Comparison of RV measurements with the corresponding RV measurements from *Gaia* DR3 . The errors on the y-axis represent the combined error, which I took as the sum in quadrature of the error in RV for UVES+ and *Gaia*. Stars indicated in green are potential spectroscopic binary candidates.

2.4.1. Coordinate transformation

To obtain the 3D Cartesian Galactic heliocentric positions and velocities from the equatorial coordinates observed by *Gaia* (ra, dec, parallax, pmra, pmdec, RV), we need a two-step transformation. First, convert the equatorial angles (ra, dec) to Galactic angles

Table 2.2.: Number of stars at each step of the selection process.

	# Members	
Initial candidates		118
compilation from Kerr et al. (2022)	110	
BANYAN	88	
High quality 6D data RV UVES+ sample		20
UVES+ 6D	29	
RUWE ≤ 1.4	26	
precise RV (e_RV< 1 km s^{-1})	24	
SB candidate	1	
High quality 6D data RV All sample		32
UVES+Gaia+APOGEE 6D	84	
RUWE ≤ 1.4	64	
precise RV (e_RV< 1 km s^{-1})	45	
SB candidate	4	
Kinematic selection		
UVES+ RV sample	15	
RV All sample	24	
Confirmed by orbital analysis (bona fide sample)		
UVES+ RV sample	10	
RV All sample	12	

(l, b). Second, by combining the two angles with distance measurement, it is possible to obtain the 3D Cartesian positions. I computed the distances by inverting the parallaxes, which is a good approximation given the low parallax errors (< 0.2%) (Luri et al., 2018). Similarly, the proper motions and radial velocities can be transformed into 3D Cartesian velocities.

I used the python package `Astropy`[1] (Astropy Collaboration et al., 2013) to perform coordinate transformations. I loaded the data file containing the member sample as `Astropy` table, which I further converted to `Gaiadata()`. Then, I applied `get_skycoord().Galactic` to obtain the Galactic coordinates of the stars. By using `.Cartesian`, I achieved the transformation to the heliocentric Cartesian position coordinates XYZ (pc). To obtain the Cartesian velocities UVW (km s^{-1}) centered at the current position of the Sun, I used the attribute `.velocity`. To determine the velocities with respect to the LSR, I utilized the peculiar solar motion of $(U_\odot, V_\odot, W_\odot) = (11.1, 12.24, 7.25)$ km s^{-1} (Schönrich et al., 2010). I performed this conversion routine for all employed RV samples (see Table 2.2).

Figure 2.3 illustrates the current distribution of stars in heliocentric positions, incorporating stars with RV data from UVES+, *Gaia*, APOGEE, and literature sources. The

[1] `https://www.astropy.org/`

magnitude of dispersion in each direction is provided in Table 2.3.

Figure 2.4 shows the Galactic heliocentric 3D Cartesian velocities I obtained utilizing the UVES+, *Gaia*, APOGEE, and literature RV measurements. Notably, the velocities associated with the stars having *Gaia* DR3 IDs 5193473840145068800, 5302978704290910592, and 5290482995153619712 are considered outliers and are excluded from the velocity distributions of *Gaia* and Literature (in the case of the first star). The dispersions on the velocities in the V direction are significantly larger compared to the other two directions (see Table 2.3). This discrepancy is not inherent to the system but arises from the higher uncertainties associated with measurements in this direction, as it is closer to the line of sight. In contrast, the tangential velocities have smaller errors, resulting in a smaller scatter in the other directions. Therefore, the observed scatter in the V direction primarily stems from limitations in the available data rather than representing a physical dispersion.

Table 2.3.: Dispersions in each direction of the present heliocentric Cartesian positions and velocities.

Sample	σ_X	σ_Y (pc)	σ_Z	σ_U	σ_V (km s^{-1})	σ_W
UVES+	9.8	16.8	9.6	0.8	2.3	0.6
Gaia	10.9	25.1	10.2	3.5	6.4	2.1
APOGEE	8.1	11.1	6.1	0.7	0.9	0.5
Literature	10.3	28.9	10.2	4.2	3.2	1.9

Table 2.4 shows the mean values for the Cartesian heliocentric positions and velocities, along with the corresponding errors on the mean calculated using the standard error of the mean (SEM). I computed these mean values based on the UVES+ sample (see Table 2.2).

Table 2.4.: Mean present positions and velocities with errors.

Positions (pc)					
$\langle X\rangle$	$\langle Y\rangle$	$\langle Z\rangle$	$\langle err_X\rangle$	$\langle err_Y\rangle$	$\langle err_Z\rangle$
15.2	-65.0	-15.9	1.8	3.1	1. 8

Velocities (km s^{-1})					
$\langle U\rangle$	$\langle V\rangle$	$\langle W\rangle$	$\langle err_U\rangle$	$\langle err_V\rangle$	$\langle err_W\rangle$
-10.4	-21.7	-5.6	0.1	0.4	0.1

Figure 2.3.: Present heliocentric position distributions for stars with different RV sources.

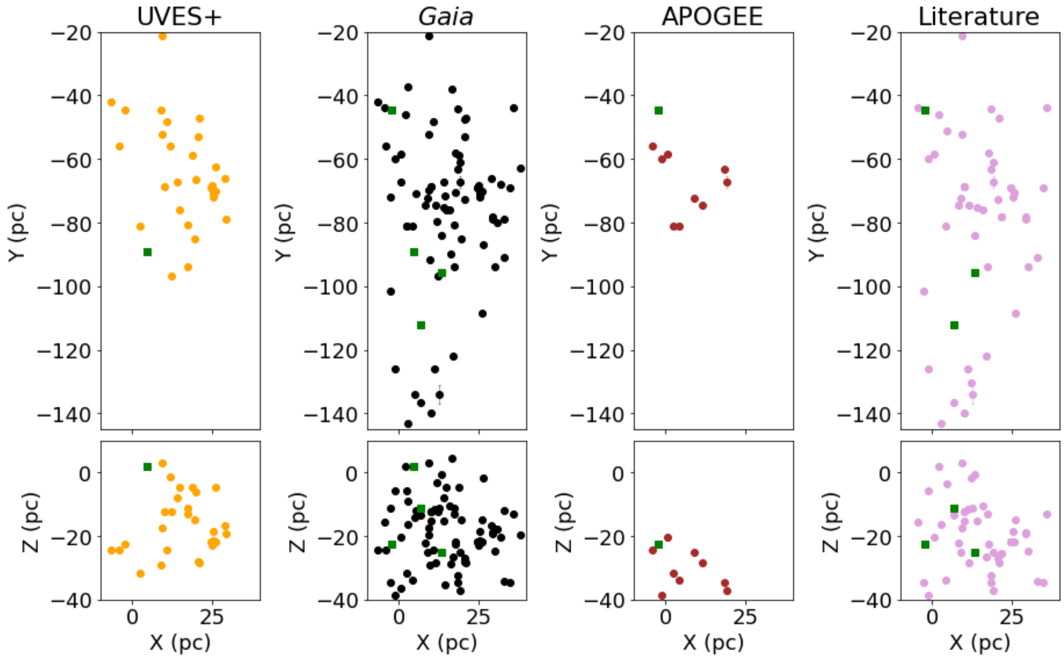

Caption/Notes. Projection in the Galactic plane (top panel) and the vertical plane (lower panel). The spectroscopic binary candidates are indicated in green.

2.5. Master table

I created a comprehensive master table that consolidates the essential information for all 118 Carina members. The table includes the unique *Gaia* ID for each member, along with the astrometry (ra, dec, parallax, and proper motion) and photometry data from Gaia. Additionally, it incorporates the available radial velocity (RV) data from various sources such as UVES+, *Gaia* DR3, APOGEE, and literature sources from Kerr et al. (2022) and SIMBAD.

Furthermore, the table encompasses the 6D phase space information of the Carina candidate members.

Moreover, the table contains a column labeled "RV_final", which provides the RV measurements of the RV All sample (see Table 2.2). This sample combines RV measurements from UVES+, *Gaia* DR3, and APOGEE. If multiple measurements were available for one star, I chose the one with the lowest error. The "r_RV_final" column indicates the source of each "RV_final" value.

Additionally, I included columns indicating which stars pass the respective selection criteria described in Section 3.1. The "RV_quality" column shows which of the RV_final measurements have uncertainties below 1 km s^{-1}. The "RUWE_cut" column marks the stars with a RUWE value smaller than the employed threshold of 1.4, and the "spec_binary" column contains the spectroscopic binary candidates. The "qual_rvfinal" and "qual_uves" columns highlight the stars in the respective samples that pass the quality selection criteria.

Furthermore, the table contains columns with computed Mahalanobis distances for the respective samples (explained in Section 3.1.2), along with "maha_flag" columns that mark, for both samples, all stars with Mahalanobis distances below the p_{74} percentile. The "bona_fide" columns indicate which stars are chosen for the dynamical traceback investigation.

Table 2.2 prepares an overview of the number of stars passing the selection criteria for the respective samples. The complete master table is accessible in the Appendix.

Figure 2.4.: Present heliocentric velocity distribution using different RV sources.

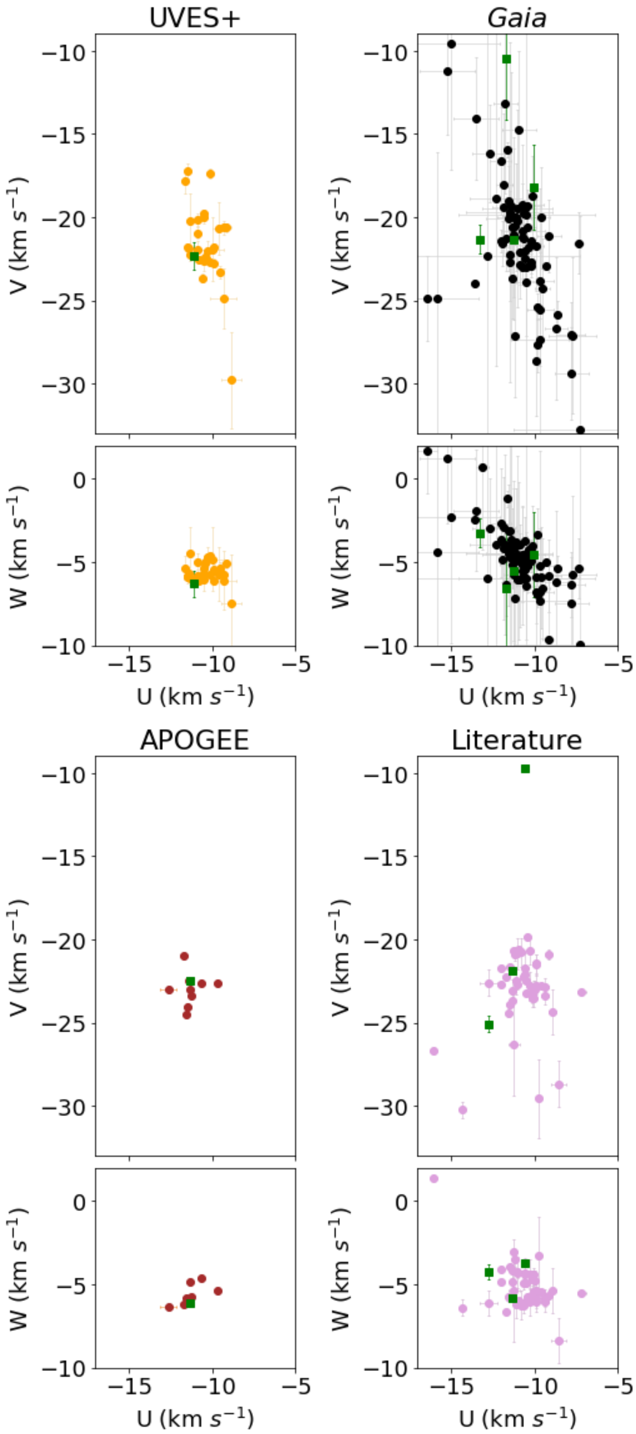

Caption/Notes. Same as Figure 2.3

3. Methods

This chapter describes the methodology used to select clean kinematic samples, integrate stellar orbits back in time, and estimate dynamical traceback ages.

3.1. Sample selection

I created a high-confidence sample of stars with precise 3D velocities. Any misidentified member or star with high observational errors can significantly bias the calculated dynamical age, as it is not moving coherently with the rest of the group and does not share a common origin with the other stars in the association. Thus, a careful selection of stars based on their kinematics and the reliability of their measurements is essential for precise dynamical age determination. This selection process is applied to two different samples: the UVES+ and the RV All sample (the "RV_final" sample from the master table, see Section 2.5).

3.1.1. Quality selection

I created a sample of precise data by excluding members with doubtful *Gaia* astrometry, RV measurements with high uncertainties, or significantly different RV measurements indicating potential binarity. This quality selection is essential to ensure that the sample consists of stars with reliable and accurate measurements for subsequent analysis.

Renormalized Unit Weight Error (RUWE)

The Renormalized Unit Weight Error (RUWE) is a metric that assesses the accuracy of astrometric observations. It indicates the agreement between the single-star model and the astrometric data, indicating excellent alignment when its value is approximately 1. To identify potential anomalies in the astrometric solution or non-single sources, it is recommended to utilize a threshold RUWE value of 1.4 (Fabricius et al., 2021). The procedure for calculating the RUWE value is thoroughly described in the documentation accompanying the *Gaia* data release[1].

My sample includes stars with RUWE values ranging from 0.8 to 17.1, and 22% have RUWE values exceeding 1.4. I excluded these objects, which are three from the UVES+ sample and 25 from the RV All selection.

[1] https://gea.esac.esa.int/archive/documentation/GDR2/Gaia_archive/chap_datamodel/sec_dm_main_tables/ssec_dm_ruwe.html

Notably, not all stars with a higher RUWE value necessarily have poor astrometric solutions. Our selections are strict, which is justified by the need for a clean sample for the dynamical traceback investigation.

Radial velocity quality

As the accuracy of RV measurements poses a significant limitation to the dynamical traceback method, I implemented a radial velocity cut. I excluded all stars with RV errors surpassing 1 km s^{-1}. By employing this threshold, I can ensure that the derived dynamical traceback age remains accurate and aligns closely with the typical dispersion observed in YLAs.

With this restriction, I excluded 5 stars from the UVES+ sample and 38 from the RV All sample for the dynamical traceback analysis. In the case of the RV All selection, this concerns primarily stars with *Gaia* RV measurements.

Spectroscopic binary candidates

Spectroscopic binaries are binary star systems that can not be resolved spectroscopically into individual components. They should be removed from the considered samples for the dynamical traceback analysis, as unresolved companions can introduce RV anomalies. This renders the traceback analysis infeasible without knowledge of the center of mass velocity, which is typically unknown.

As discussed in Section 2.3.5, one star of the UVES+ sample, *Gaia* DR3 52501500-91153808768, exhibits a significant deviation between its *Gaia* DR3 RV measurement and the one derived by UVES+. This discrepancy strongly suggests that it is a spectroscopic binary and, therefore, it is excluded from the dynamical traceback investigation.

Within the RV All sample, I excluded 4 stars due to their identification as spectroscopic binary candidates. Notably, one of these stars coincides with the star excluded from the UVES+ sample. Furthermore, *Gaia* DR3 5481327629267108992 exhibits a significantly divergent RV measurement in the APOGEE catalog compared to *Gaia* DR3. Additionally, two stars, namely *Gaia* DR3 5276844309323980800 and *Gaia* DR3 5305225281435405568, have been identified as spectroscopic binaries based on literature RV measurements. These stars are those highlighted in green in Figure 2.4.

3.1.2. Kinematic selection

I implemented a kinematic selection method to eliminate any kinematic outliers present in the sample. These outliers possess high-quality measurements but do not align with the overall distribution of the association. In this context, kinematic outliers refer to sources whose velocities deviate significantly from the association. They can either be spectroscopic binaries, where the observed RV is not representative of the center of mass or not members of Carina.

Mahalanobis distance

Following a similar approach as Miret-Roig et al. (2020), I employed the Mahalanobis distance to identify and remove kinematic outliers within the 3D velocity distribution (UVW). The Mahalanobis distance is defined as

$$D_M(\mathbf{x}) = \sqrt{(\mathbf{x} - \boldsymbol{\mu})^T \boldsymbol{\Sigma}^{-1} (\mathbf{x} - \boldsymbol{\mu})} \tag{3.1}$$

where `x` corresponds to the observational data, $\boldsymbol{\mu}$ to the central location, and $\boldsymbol{\Sigma}$ to the covariance matrix[2].

I utilized the `MinCovDet().mahalanobis()` function from the `covariance` module in Python's `sklearn` library to compute the Mahalanobis distance. The resulting Mahalanobis distances are visualized in a histogram (see Figures 3.1 and 3.2), where the percentile p_{75} is indicated. All members with a Mahalanobis distance exceeding this cut-off limit are eliminated from further investigations.

The choice of this threshold is based on empirical analysis, striking a balance between excluding kinematic outliers that could impede accurate traceback analysis and retaining kinematic members relevant to the overall study. By eliminating all members with Mahalanobis distances exceeding this limit, the subsequent investigations focus on a refined subset of stars that exhibit coherent motion within the association. A total of 5 stars from the UVES+ sample and 8 from the RV All sample were identified as kinematical outliers and were thus excluded from further investigations.

Traceback orbit selection

Despite the previous selection criteria, some stars passed all the specified cuts but exhibited orbits that significantly deviated from the main group. These stars are distant from the core of the association during the birthtime of Carina. I conducted a careful manual selection process to identify and exclude these stars, ensuring a robust analysis of the dynamical age. I identified and rejected 5 stars from the UVES+ sample and 13 stars from the RV All sample. Table 2.2 prepares an overview of how many stars are rejected by which criterium.

3.2. Orbit initialization and integration

In this section, I describe how I obtained the backward orbits of stars that have passed the quality selection. This conversion allows for a comprehensive examination of the stars'

[2] `https://scikit-learn.org/stable/auto_examples/covariance/plot_mahalanobis_distances.html`

historical trajectories within the Galactic context.

3.2.1. Galpy

I used the python package `Galpy` (Bovy, 2015) for the orbital integration, which is specifically geared towards the study of the movement and patterns of orbits in external gravitational potentials. The framework offers support for numerical orbit integration using a range of Runge-Kutta-type and symplectic integrators. In addition, `Galpy` allows integrating the phase space volume for planar orbits. The orbit integration with `Galpy` uses a Galactic potential to integrate the equations of motions of specific objects. The orbits are initiated using the `Orbit()` tool of `Galpy`, where the present positions and velocities of individual stars need to be entered. There are multiple ways to initialize the orbit, but the easiest approach is to use either Galactic or equatorial coordinates as input. `Galpy` can seamlessly handle the conversion from equatorial to Galactic coordinates. However, it is also possible to utilize Galactocentric coordinates as input. In this case, the data must be transformed from a heliocentric view to Galactocentric coordinates before being used as input. While this approach is slightly more complicated, the resulting orbits are not affected by the choice of the coordinate system.

3.2.2. Orbit initialization

I have developed a Python script that allows users to choose between three options for orbit initialization.

For an input in equatorial coordinates (see Section 1.3.2), the `radec` parameter must be set to `True`. The value of the solar motion is set to $(U_{\odot}, V_{\odot}, W_{\odot}) = (11.1, 12.24, 7.25)$ km s^{-1} (Schönrich et al., 2010), and the distance from the Sun to the Galactic center (ro) and the circular velocity at this position (vo) to 8 kpc and 220 km s^{-1}, respectively, since Carina is close to the Sun (approximately 0.07 kpc away).

The initialization process for Galactic coordinates (see Section 1.3.3) is similar but requires the `lb` parameter to be set to `True` and the input of Galactic coordinates.

Initializing a Galactocentric orbit (see Section 1.3.5) requires converting equatorial coordinates to Galactocentric coordinates. I used the `Galactocentric()` class from `astropy.coordinates` to create a Galactocentric frame with a distance of 8 kpc to the Galactic center. I then applied the `transform_to(galcen_frame)` method from `Astropy` to the equatorial coordinates to obtain Galactocentric coordinates. The cylindrical representation is obtained by assigning `.cylindrical` to the Galactocentric coordinates, which delivers (R, z, ϕ). The velocities (v_R, v_z, v_ϕ) are obtained by applying `.differentials` to the Galactocentric cylindrical coordinates. The tangential velocity is computed by multiplying the angular velocity with the radius ($v_T = v_\phi \cdot R$).

3.2.3. Orbit integration

I used `Orbit().integrate()` to integrate the orbit for a duration of 50 Myr and 500 timesteps, utilizing the `MWPotential2014` model (Bovy, 2015).

Changing the Galactic potential has little influence on the orbits of young stars in the solar neighborhood over a 50 Myr integration time, as this period is only a low fraction of the entire orbit of the Sun around the Galactic center. Moreover, the types of orbits studied here are nearly circular, showing small deviations from the perfectly circular orbit. Therefore, it is unlikely that the association will come much closer to or move much further away from the Galactic center. The effects of uncertainties in the Galactic potential are most significant close to the center or far out and have little impact on regions close to the Sun.

To determine the motion of Carina members with respect to the LSR, I simulate a hypothetical object moving on a perfectly circular orbit around the Galactic center with the following initial conditions: ($R = 8$ kpc, $v_R = 0$ km s^{-1}, $v_T = 220$ km s^{-1}, $z = 0$ kpc, $v_z = 0$ km s^{-1}, $\phi = 0°$). This orbit is integrated with the same potential and over the same period as the Carina orbits and is then subtracted from them to obtain the desired motion. Figure 3.3 illustrates 2D projections of the resulting orbits of Carina members integrated back for 50 Myr for the two employed samples.

3.3. Association size estimation and dynamical traceback age

The dynamical traceback age of a stellar association is the time when its members were most concentrated. Nonetheless, the literature employs various techniques to estimate the size of an association over time, which can lead to significant variations in the calculated dynamical traceback ages.

One common approach is to estimate the size based on the empirical standard deviation in the spatial coordinates, but this method is sensitive to outliers. Miret-Roig et al. (2020) devised an approach to estimate the size of an association using three different functions: the trace, the determinant, and the square roots of the diagonal terms of the covariance matrix in each direction. All of these functions are calculated from the covariance matrix of the association in the configuration space, which can be defined as

$$C = \begin{pmatrix} \sigma_x^2 & \sigma_{xy} & \sigma_{xz} \\ \sigma_{yx} & \sigma_y^2 & \sigma_{yz} \\ \sigma_{zx} & \sigma_{zy} & \sigma_z^2 \end{pmatrix} \tag{3.2}$$

where

$$\sigma_{xy} = \frac{\sum(X - \mu_x)(Y - \mu_y)}{n} \tag{3.3}$$

The association's size determined via the trace of the covariance matrix (S_{TCM}) is defined as

$$S_{TCM} = \left(\frac{Tr(C)}{3}\right)^{1/2} \tag{3.4}$$

The trace is commonly known as the overall variance of a matrix, and it aligns with the summation of its eigenvalues. Since the trace of the covariance matrix of the association in the configuration space has units pc^2, the square root is needed, and the division by three is for averaging over the three spatial directions. Therefore, it is possible to construe the S_{TCM} estimator as the arithmetic mean of the variances among the individual components.

Secondly, the size obtained by the determinant of the covariance matrix (S_{DCM}) is defined as

$$S_{DCM} = det(C)^{1/6} \tag{3.5}$$

The determinant of the covariance matrix provides information about the variability of a dataset. It is computed as the geometric mean of the eigenvalues of the covariance matrix. A larger determinant indicates a greater spread of the data along the principal axes of variation. Moreover, the determinant is directly related to the volume of the association described by the data. Specifically, the volume of the association is proportional to the square root of the determinant.

The third size estimator (S_X, S_Y, S_Z) is derived using the squared roots of the diagonal terms of the covariance matrix in the spatial directions. When the values are unweighted, the square roots of the diagonal terms of the covariance matrix correspond to the standard deviations.

I followed the strategy from Miret-Roig et al. (2020) using two approaches to compute the covariance matrix: empirical covariance estimation and robust covariance estimation. While the empirical one coincides with the maximum likelihood covariance estimator, the robust covariance estimation gives less weight to outliers and is thus more robust against them. I use the `Sklearn` python package to compute these. I obtained the empirical covariance estimation by applying the `empirical_covariance()` class of the `covariance` package to the positions of the integrated stellar orbits at each timestep. For the robust estimation, I fitted the `MinCovDet()` class from the same package to the data and derived the resulting covariance matrix using the `.covariance` attribute[3].

Initially, I applied the covariance matrices only to the stellar XYZ positions in the present and compared the resulting estimates. As expected, the values of the robust covariance matrix were smaller than those of the empirical estimate. Subsequently, I employed both algorithms on the entire dataset for all timesteps.

[3] `https://scikit-learn.org/stable/modules/covariance.html`

Furthermore, I calculated the mentioned size estimators for each covariance estimation and plotted the resulting size estimates (S_{TCM}, S_{DCM}, S_X, S_Y, S_Z) against the integration time to determine the time when the association's size is at its smallest, representing the determined traceback age (see Section 4).

Figure 3.1.: Histogram of Mahalanobis distance using UVES+ RV sample

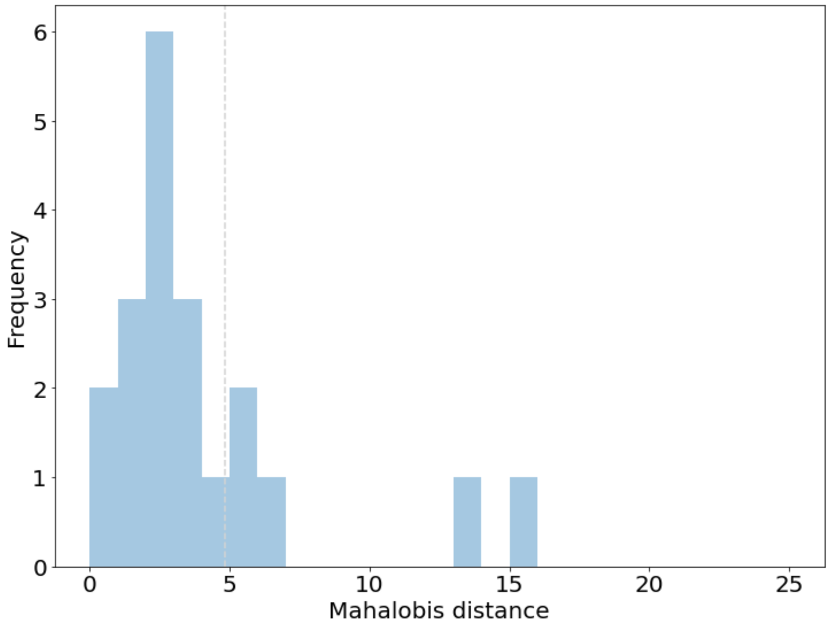

Caption/Notes. The vertical dashed lines indicate the percentile p_{75} used as a threshold for the cut.

Figure 3.2.: Histogram of Mahalanobis distance using RV All sample

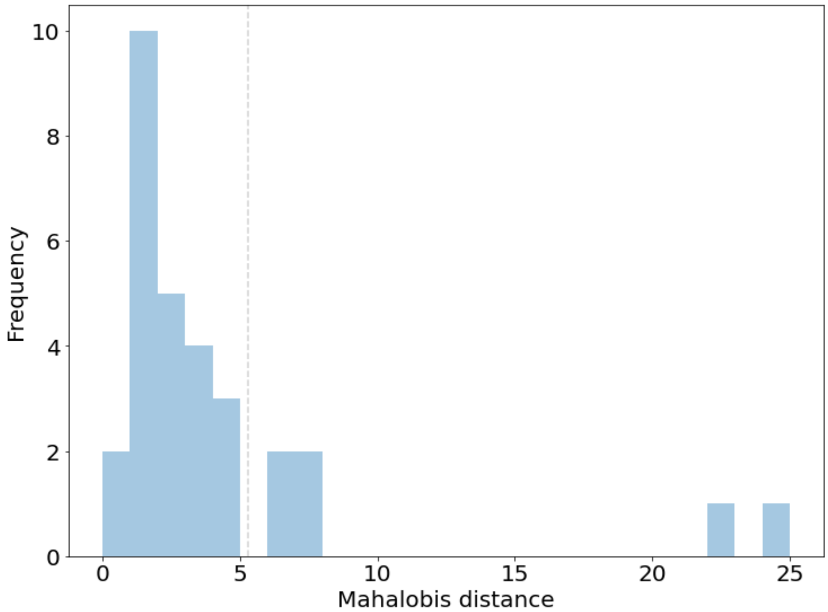

Caption/Notes. Same as Figure 3.1.

Figure 3.3.: 2D projection of the orbits of Carina members integrated back in time.

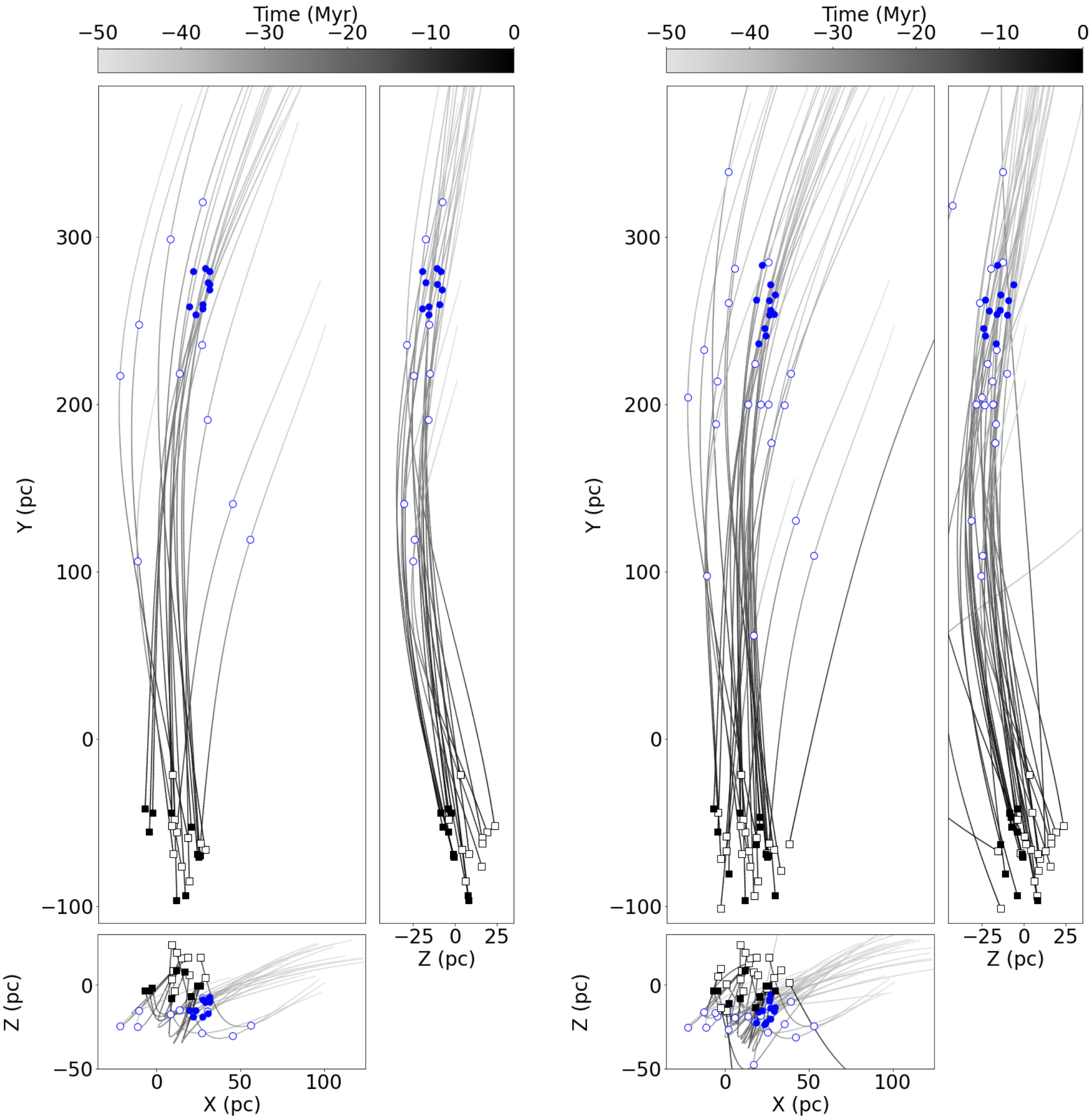

Caption/Notes. Left: using the sample of UVES+ RVs. Right: using the RV All sample. For each of these two Figures, I show the Galactic plane view (top left) and the two vertical planes (bottom left and top right). The orbits are integrated back in time 50 Myr using the `MWPotential2014` Galactic potential. The orbits are color-coded with the backward time; the black squares represent the positions in the present ($t = 0$ Myr), and the blue dots the positions at the birth time ($t = -32.7$ Myr for the UVES+ sample and $t = -31$ Myr for the combined RV sample).

4. Results

This chapter presents the dynamical ages of the Carina YLA for different member selection methods. I considered three cases: (1) using only the members of the UVES+ RV sample, (2) including additional RV measurements from *Gaia* and APOGEE, and (3) using the same sample and methodology as Kerr et al. (2022) to replicate their results. Table 4.3 provides an overview of the resulting ages. Furthermore, I investigated the origin of the Carina association in relation to nearby YLAs.

4.1. Dynamical traceback age with UVES+ RVs

I applied the traceback analysis to the UVES+ sample (see Section 2.3.1). This sample offers the advantage of homogeneity and high precision of radial velocities (median error = 0.4 km s^{-1}). I excluded stars that did not meet the quality and kinematic selection criteria (described in Section 3.1) from the sample for the traceback investigation. In addition, I rejected stars with significantly different orbits that do not converge to the main part of the association around birth time. Figure 4.1 illustrates the present heliocentric velocity and position distribution for this sample. I observe that stars rejected by the kinematic and orbital selections (green and red stars) are especially dispersed along the velocity coordinate V, closely aligned with the line of sight direction. Some of these stars are also closer to the Galactic plane ($Z \sim 0$ pc) than the rest of Carina's bona fide members (orange stars).

In Figure 4.3, I present the estimates of the association's size using two different covariance matrix-based methods: empirical covariance matrix-based size estimates (top panels) and robust covariance matrix-based size estimates (bottom panels). I obtained the size estimates using various metrics described in Section 3.3. To smooth out the lines, I plot the median of 1000 bootstrap samples, while the shaded areas represent the 1σ uncertainties. The vertical lines indicate the respective minima.

Remarkably, the minimum sizes estimated by the empirical covariance estimate closely resemble those obtained with the robust covariance estimate, except for those estimated with S_{DCM}. This consistency suggests that there are no sources with large dispersions in the sample. Typically, significant differences between these estimates can arise due to the robust covariance estimate's superior handling of outliers. To ensure a more reliable estimation of the stars' multivariate position and dispersion while reducing sensitivity to outliers, I have chosen to adopt the approach described in Miret-Roig et al. (2020) and utilize the robust covariance matrix. This choice enhances our capability to obtain a more accurate and robust estimate of the stars' age.

Additionally, dynamical ages depend on the applied size estimator. Comparing the sizes deduced from the main diagonal elements of the covariance matrix (S_X, S_Y, S_Z) as shown in the bottom left panel of Figure 4.3, the obtained minima differ depending on the respective direction. The size estimator S_X indicates an approximate dynamical age of 27 Myr, while the S_Z estimator yields a resulting age of around 34 Myr. The S_Y size estimator provides an age estimate of approximately 37 Myr, aligning more closely with the S_Z result. To overcome the challenge of measuring distinct values for association size in each direction, I employ the S_{TCM} estimator, which combines the contributions from all three directions, providing an averaged value. According to the S_{TCM} estimator, the minimum inferred size of the association is approximately 33 Myr (see bottom right panel), aligning more closely with the findings obtained from S_Y and S_Z. The bottom middle panel emphasizes the robust size determined with the S_{DCM} size estimator, which provides a measure of the overall volume occupied by the association. However, the S_{DCM}-based association size, determined by the robust covariance matrix determinant, exhibits a plateau that spans approximately 10 Myr. This plateau roughly coincides with the lowest points observed in the curves obtained from the S_X and S_Z estimators. As a result, pinpointing the precise location of the minimum size of the association becomes highly uncertain when using this method, in contrast to the more reliable outcomes achieved with alternative approaches. Table 4.1 contains a summary of all resulting median ages using different size estimators.

As described in Section 3.3, the S_{TCM} size represents the arithmetic mean, and the S_{DCM} size is the geometric mean of the eigenvalues of the covariance matrix. In general, the arithmetic mean is always larger or equal to the geometric mean, and they are equal only if all values are identical. Since an isotropic covariance matrix does not apply to my considerations, the size estimates with S_{TCM} are larger than those with S_{DCM}. Carina has a median minimum S_{DCM} size of approximately 3 pc and a median minimum S_{TCM} size of approximately 6 pc, which aligns more closely with what has been observed in starforming regions such as Ophiuchus (Cánovas et al., 2019), Taurus (Galli et al., 2019), and Corona Australis (Galli et al., 2020). Therefore, I use the S_{TCM} size estimator, which provides a measure of the total dispersion of the data along all dimensions and leads to a more robust estimate of Carina's size.

From the age estimates of the 1000 bootstrap samples, I derived a distribution of ages. Figure 4.5 presents the age distribution with a bandwidth of 1 Myr, which is smaller and of the same order as the age uncertainties. The age distribution computed from the S_{DCM} size estimator shows a wider spread than from the S_{TCM}, highlighting the larger uncertainties in the age estimation when computed from the S_{DCM} size estimator. Table 4.2 shows the mode and the 68%, 95%, and 99.7% highest density intervals of the age distribution. Considering the S_{TCM} size estimator and the 68% highest density interval for the uncertainty, I determined a dynamical age of Carina as $32.7^{+3.1}_{-1.9}$ Myr (see Table

4.3). For comparison, using the S_{DCM} size estimator, I obtained a highly uncertain age of $26.9^{+1.2}_{-26.9}$ Myr. The two values do not agree within the uncertainties. However, as mentioned, considering the Figures 4.3 and 4.5, it can be seen that no clear minimum could be obtained when employing the S_{DCM} estimator, and its age distribution is much wider, so this estimate is not reliable.

Table 4.1.: Median of the age distributions (Myr).

Sample	Covariance	S_{TCM}	S_{DCM}	S_X	S_Y	S_Z
UVES+	Robust	32.7	26.9	27.1	37.4	33.7
	Empirical	32.4	35.4	26.3	35.0	34.3
RV All	Robust	31.1	36.1	27.8	23.8	44.4
	Empirical	30.0	35.9	27.0	27.7	36.7

4.2. Dynamical traceback age with combined UVES, *Gaia*, and APOGEE RVs

I expanded the traceback analysis to include the second sample, which combines radial velocities from multiple sources: *Gaia*, APOGEE, and our measurements for the selected Carina members. Similar to the first sample, all stars in this set had to meet the quality and kinematic criteria outlined in Section 3.1. After applying these criteria, I identified 32 stars that satisfied the requirements and traced their trajectories backward in time. I compared the resulting orbits and excluded stars with significantly different orbits to the core group, resulting in a final sample of 12 stars for estimating the age of Carina. Figure 4.2 illustrates the distribution of present velocities and positions for both the rejected and selected members. It is evident from the figure that the rejected stars exhibit the largest discrepancies in their V velocities compared to the chosen stars, although differences are also noticeable in their W velocities.

To estimate the evolution of Carina's size, I plotted the median estimated sizes obtained from this sample in Figure 4.4, following the same strategy as in Figure 4.3. Once again, the median minima of the estimated sizes, using both empirical and robust covariance matrices, occurred at similar times, indicating a good selection of stars. I adopted the approach used with the UVES+ sample and focused on the estimates derived from the robust covariance matrix.

By Comparing the minima from the robust sizes obtained from the S_X, S_Y, and S_Z size estimators in the bottom left panel of Figure 4.4, I observe differences for the respective directions. The S_X size estimator suggests a dynamical age of approximately 28 Myr, while S_Y indicates an age of about 24 Myr and S_Z of around 44 Myr. Consequently, unlike the results from the UVES+ sample, in this case, the age estimates derived from S_X and S_Y align more closely. Comparing the resulting ages obtained from this sample with those using the UVES+ sample, it is apparent that the estimate from S_Y implies a younger age for this sample compared to the UVES+ sample, while the estimates from S_X and S_Z remain roughly the same. Although the age result obtained with S_{DCM} is more distinct than with the previous sample, suggesting an older age of about 36 Myr, I maintain consistency by once again employing the S_{TCM} size estimator for the final result. The age derived from S_{TCM} yields a similar age to that of the UVES+ sample, approximately 31 Myr. The median ages computed by different size estimators with this sample are reported in Table 4.1.

The age distribution obtained from this larger combined sample is depicted in Figure 4.6, and Table 4.2 presents the mode, as well as the 68%, 95%, and 99.7% highest density intervals of the age distribution. Considering the S_{TCM} size estimator and the 68% highest density interval, I estimate the dynamical age of Carina to be 31^{+5}_{-9} Myr, which agrees with the age computed using the UVES+ sample within the uncertainties. For comparison, the obtained age with the S_{DCM} size estimator is 36^{+1}_{-12} Myr, providing a slightly better uncertainty. However, it is consistent with the estimate from the S_{TCM} size estimator within the uncertainties.

Table 4.2.: Dynamical age (Myr) obtained with the robust metrics for the different samples.

Sample	Size estimator	$p_{0.15}$	$p_{2.5}$	p_{16}	mode	p_{84}	$p_{97.5}$	$p_{99.85}$
UVES+	S_{DCM}	-48.9	-38.4	-28.1	-26.9	0	0	0
	S_{TCM}	-50	-39.2	-35.8	-32.7	-30.8	-20.3	0
RV All	S_{DCM}	-50	-37.3	-37.1	-36.1	-23.8	0	0
	S_{TCM}	-40.4	-38.2	-36.1	-31.1	-22.6	-12.9	0

Notes. The mode and the highest density interval for probabilities of 68%, 95%, and 99.7% are illustrated.

4.3. Dynamical traceback age with the sample from Kerr et al. (2022)

Using the membership, RV data, and cuts as described by the authors in Kerr et al. (2022), I reconstructed the resulting dynamical age for Carina. I utilized Tables 1 and 2 from their publication, which contained the spectroscopic and astrometric data of all considered associations. The authors applied an HDBSCAN clustering algorithm to their initial member samples and used the reclustered member samples indicated in Table 2 ($REG = 2$) for their dynamical age computations.

To acquire a comprehensive dataset, I cross-matched these tables and compiled all the Carina members with RV measurements. Their reclustered Carina sample contains recorded RV measurements for 76 stars. It's worth noting that after reclustering, several stars initially classified as Carina members were identified as Platais 8 members, while some stars originally categorized as Columba or Tucana-Horologium members were included. Table 2, provided by the authors, only included stars consistent with youth ($G > 7.9$ mag).

Following their approach to stellar selection, I applied additional general cuts. Stars were excluded from the traceback analysis if they did not pass the astrometric quality flag, had resolved binaries, had $RUWE > 1.2$, had an RV error > 0.5 km s^{-1}, or were represented by *Gaia* RVs. Furthermore, as the RVs were drawn from a heterogeneous sample, the authors performed two additional cuts to exclude velocity outliers for Carina. They removed stars that were outside the 3σ extent of an ellipsoid, with the extents along the U, V, and W axes determined by a 3σ sigma-clipped standard deviation and median of stars along each respective axis. Additionally, their second cut excluded all Carina members with $V > -22$ km s^{-1}. With these selection criteria, I reduced the sample to only six stars.

I integrated the orbits of this selection back in time for 60 Myr using the `MWpotential14` model. Subsequently, I calculated the median distance to all other Carina members for each age step and star. I obtained a sample of stellar traceback ages by determining the time when the median distance was the smallest for each star. I excluded all stars with individual traceback ages less than 10 Myr, resulting in the rejection of one star (*Gaia* DR3 5299141546145254528).

With the final sample, I recalculated the individual traceback ages and estimated the age for Carina by taking the median of those plotted over time (refer to Figure 4.7). This investigation yielded an age estimation for Carina of 34^{+6}_{-6} Myr, where the uncertainty represents one standard deviation. Kerr et al. (2022) derived a dynamical age of $32.9^{+8.2}_{-8.2}$ Myr for Carina, which is consistent with my estimate within the error range. Furthermore, the estimated size aligns with their finding of a minimum median mutual distance of approximately 20 pc.

Table 4.3 summarizes all the estimated ages computed in this work, where the one using the strategy of Kerr et al. (2022) delivers the oldest and the one obtained with the combined RV All sample the youngest age. The median is the estimation using the homogeneous UVES+ sample, which I also use as the resulting traceback age of this work.

Table 4.3.: Summary of resulting ages.

Sample	Nr. of stars	Age (Myr)
UVES+	10	$32.7^{+3.1}_{-1.9}$
RV All	12	31^{+5}_{-9}
Kerr et. al	5	34^{+6}_{-6}

4.4. Isochronal ages

Figures 4.8, 4.9, and 4.10 depict color-magnitude diagrams (CMDs) illustrating Carina members. The first CMD (Figure 4.8) includes the 20 high-quality 6D Carina members of the UVES+ sample (refer to Table 2.2). The second one (Figure 4.9) presents a CMD for the high-quality 6D stars of the RV All sample, consisting of 32 stars. On the other hand, the last plot shows a CMD of all the reclustered Carina members from Kerr et al. (2022) for which RV measurements are available, and that pass their selection criteria, which applies to 6 stars.

To construct these CMDs, I plotted the absolute magnitudes in the G-band against the differences between the G-band Blue Photometer and the G-band Red Photometer obtained from the *Gaia* DR3 data. To convert the apparent magnitudes from *Gaia* DR3 to absolute magnitudes, I used the following formula from Hughes (2006):

$$M_G = (G_{\text{mag}}) - 5 \cdot \log_{10}(d) + 5 \tag{4.1}$$

To calculate the distances (d), I employed the inverse of the individual parallaxes. This approach is a good approximation due to the low parallax errors obtained from *Gaia* DR3. Notably, I did not account for the influence of extinction in this calculation. However, considering that the stars under study are in close proximity and not embedded within a cloud, neglecting extinction is a reasonable approximation (Luri et al., 2018).

Additionally, I overlaid three distinct isochrones on the CMDs, which correspond to ages similar to those derived from the observed data. These isochrones were selected from two different libraries of stellar evolution models: PARSEC (Bressan et al., 2012; Marigo et al., 2017) and BHAC15 (Baraffe, Isabelle et al., 2015). Specifically, I included a 30 Myr old isochrone from the PARSEC models, a 40 Myr old isochrone from the PARSEC models, and a 30 Myr isochrone from the BHAC15 models.

The CMDs provide evidence that the stars I excluded based on kinematic properties (green and red points) exhibit a similar age distribution to Carina. This observation suggests that these stars are not old field stars but likely members of other young associations located in the same vicinity.

S. Ratzenböck fitted isochrones to the data samples employed in this work, as depicted in Figure 4.11. A Bayesian routine utilizing the PARSEC models was used for both samples, allowing us to estimate the age uncertainties (Ratzenböck et al., 2023). The age estimates obtained are $35.2^{+38.7}_{-25.8}$ Myr for the UVES+ sample and $29^{+35.3}_{-26.8}$ Myr for the RV all sample. The uncertainties are expected to be larger when dealing with less data, as seen in the case of the UVES+ sample. Despite the varying amounts of data, both datasets yield similar results, compatible within the uncertainties. However, the RV All sample, which includes more data, suggests a slightly lower age.

4.5. Origin of the Carina association

To investigate the formation region of Carina and 16 other associations in the solar neighborhood, I selected all the young (<50 Myr) stellar associations in the solar neighborhood (<130 pc) from Gagné et al. (2018a) (see Table 4.4). I conducted an analysis using their mean present positions and velocities. I aimed to trace their orbits back to the time they formed by integrating their orbits backward in time for 50 Myr, utilizing the `MWPotential14` model.

I obtained the 6D phase space data and ages of most of the YLAs mentioned in Table 4.4 from Tables 1 and 9 of Gagné et al. (2018a). I used data from this study, while for the ages of β Pictoris and Tucana-Horologium, I rely on the work of Miret-Roig et al. (2020) and Galli et al. (2023), respectively. I also included two older associations, namely AB Doradus (ABDMG) and χ^1 For (also known as Alessi 13) associations in my analysis, as their ages are not well determined yet, and there is a possibility that they might be younger than initially thought, which could provide valuable information for understanding the evolution of these associations.

Figure 4.12 displays the resulting paths of the YLAs in heliocentric Cartesian coordinates, presented in both a two-dimensional plane and a vertical projection. The grayscale variation within each orbit represents different points in time, while the colored markers indicate the positions of the specific associations at the time of their origin. It is important to note that since my investigation covers a period of only 50 Myr, the origins of the older associations, AB Doradus and χ^1 Fornacis, are placed at 50 Myr. From the figure, two prominent nodes of associations can be inferred to have potentially shared a common origin. The first node includes the associations β Pictoris, Upper Centaurus Lupus (UCL), Lower Centaurus Crux (LCC), ϵ Chamaeleontis (EPSC), η Chamaeleontis (ETAC), Upper Scorpius (USCO), and TW Hya (TWA). These associations are connected to Scorpius-Centaurus, which has been extensively studied in Fernández et al. (2008). The second formation node comprises Carina, Tucana-Horologium, Columba, and χ^1 Fornacis. These YLAs exhibit similar paths and seem to share a common origin, which was also suggested by Miret-Roig et al. (2018) and Galli et al. (2021). Figure 4.13 shows only the paths of these associations to provide a clearer representation. To quantify the spatial dispersion of these associations at the time of their origins, I computed their 3D mutual median distance. The dispersion is 142.5 pc when including χ^1 Fornacis, which has the largest separation among these associations, and 81.4 pc when considering only Carina, Tucana-Horologium, and Columba.

The χ^1 Fornacis association has been estimated to be approximately 500 Myr old based on isochronal fitting and the main-sequence turnoff, as reported by Pöhnl and Paunzen (2010) and Kharchenko et al. (2013). However, despite this age, the trajectory of χ^1 Fornacis shows remarkable similarity to those of Carina, Tucana-Horologium, and Columba. If the age of χ^1 Fornacis were younger than initially thought, as also suggested by Mamajek (2016), the association would have a close formation region to Carina, Columba, and Tucana-Horologium. Mamajek (2016) and Galli et al. (2021) stated that χ^1 Fornacis could be as young as 30 Myr old due to the saturated X-ray emission observed in its members.

To resolve this discrepancy and gain a clearer understanding of the formation scenario for these YLAs, further investigations into the age of the χ^1 Fornacis association are required. Conducting new high-resolution spectroscopic measurements would enable the determination of its dynamical age. This additional information would contribute significantly to refining our understanding of the evolutionary processes of these YLAs.

Table 4.4.: Mean positions and heliocentric velocities of YLAS with their age estimates.

Ass.	$\langle X \rangle$	$\langle Y \rangle$ (pc)	$\langle Z \rangle$	$\langle U \rangle$	$\langle V \rangle$ (km s^{-1})	$\langle W \rangle$	Age (Myr)	Ref.
CAR	14.88	-75.29	-18.32	-11.22	-21.35	-4.81	$32.7^{+3.1}_{-1.9}$	0
118Tau	-102.3	-4.8	-9.9	-12.8	-19.1	-9.2	~ 10	1
ABDMG	-6.0	-7.2	-8.8	-7.2	-27.6	-14.2	149^{+51}_{-19}	2
betaPic	4.1	-6.7	-15.7	-10.9	-16.0	-9.0	$18.5^{+2.0}_{-2.4}$	3
COL	-25.9	-25.9	-21.4	-11.90	-21.28	-5.66	42^{+6}_{-4}	2
EPSC	49.9	-84.8	-25.6	-9.9	-19.3	-9.7	$3.7^{+4.6}_{-1.4}$	4
ETAC	33.65	-81.36	-34.81	-10.0	-22.3	-11.7	11^{+3}_{-3}	2
OCT	4.0	-96.9	-59.7	-13.7	-3.3	-10.1	35^{+5}_{-5}	5
THA	5.4	-20.1	-36.1	-9.79	-20.94	-0.99	$38.5^{+1.6}_{-8}$	6
THOR	-88.4	-25.7	-23.9	-12.8	-18.8	-9.0	22^{+4}_{-3}	2
TWA	14.4	-47.7	22.7	-11.6	-17.9	-5.6	10^{+3}_{-3}	2
XFOR	-27.1	-46.3	-84.2	-12.54	-22.24	-6.26	~ 500	7
ROPH	124.79	-15.23	37.60	-5.9	-13.5	-7.9	< 2	8
TAU	-116.3	6.7	-35.9	-14.3	-9.3	-8.8	$1 - 2$	9
LCC	54.3	-94.2	5.8	-7.8	-21.5	-6.2	15^{+3}_{-3}	10
UCL	107.5	-60.9	26.5	-4.7	-19.7	-5.2	16^{+2}_{-2}	10
USCO	121.2	-17.0	48.9	-4.9	-14.2	-6.5	10^{+3}_{-3}	10

References. (0) This work; (1) Mamajek (2016); (2) Bell et al. (2015); (3) Miret-Roig et al. (2020); (4) Murphy et al. (2013); (5) Murphy and Lawson (2015); (6) Galli et al. (2023); (7) Pöhnl and Paunzen (2010); (8) Wilking et al. (2008); (9) Kenyon and Hartmann (1995); (10) Pecaut and Mamajek (2013).

Figure 4.1.: Present heliocentric velocity and position distributions using UVES+ sample.

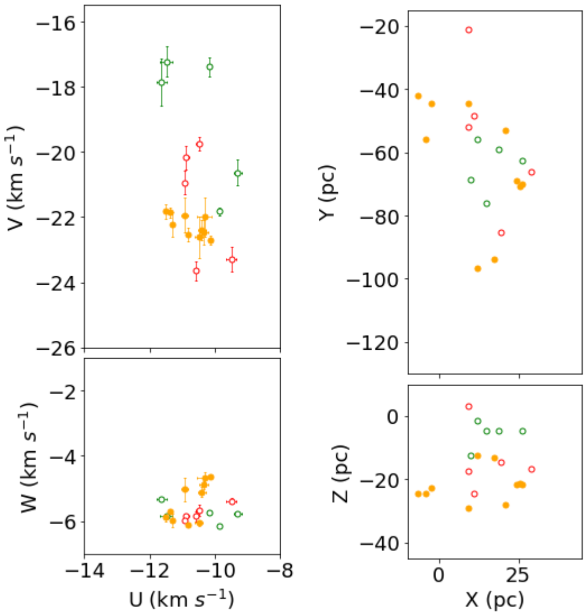

Caption/Notes. The included stars are from the high-quality 6D data sample. Chosen stars for traceback investigation (orange), stars excluded by large Mahalanobis distance (green), and stars excluded because of significantly differing orbits (red).

Figure 4.2.: Present heliocentric velocity and position distributions using RV All sample.

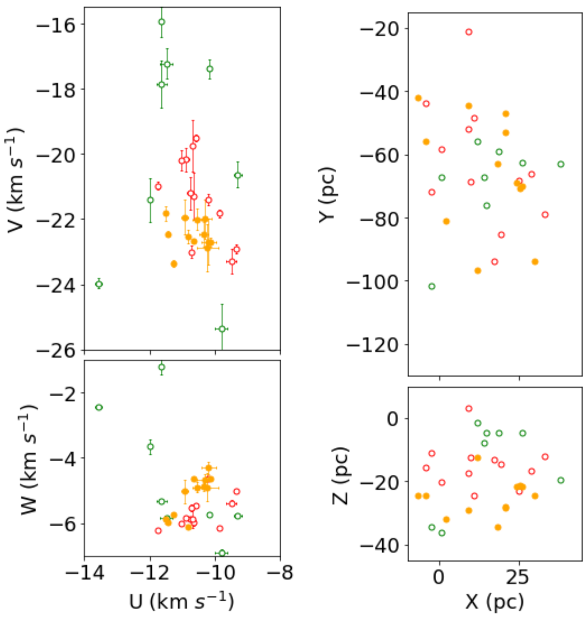

Caption/Notes. Same as Figure 4.1.

Figure 4.3.: Size estimation of the Carina YLA with the UVES+ RV sample

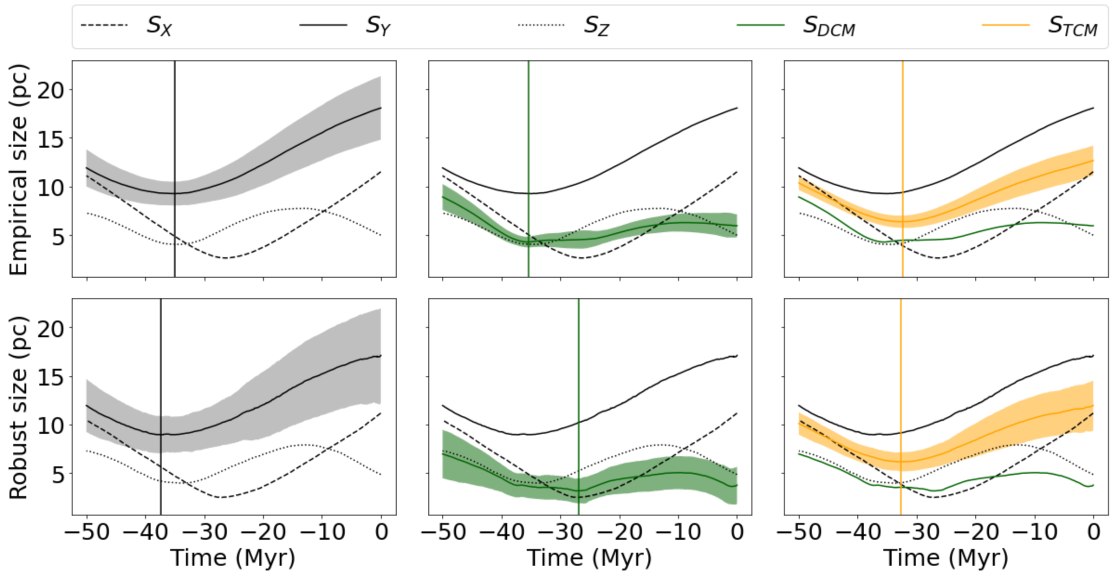

Caption/Notes. The association size as a function of traceback time employing various estimators. The top panels depict the computations with the empirical covariance estimate, and the bottom panels show the ones with robust covariance estimates. The median of 1000 bootstrap repetitions is plotted as lines, while the shaded areas represent the 1σ uncertainties.

Figure 4.4.: Size estimation of the Carina YLA with the RV All sample

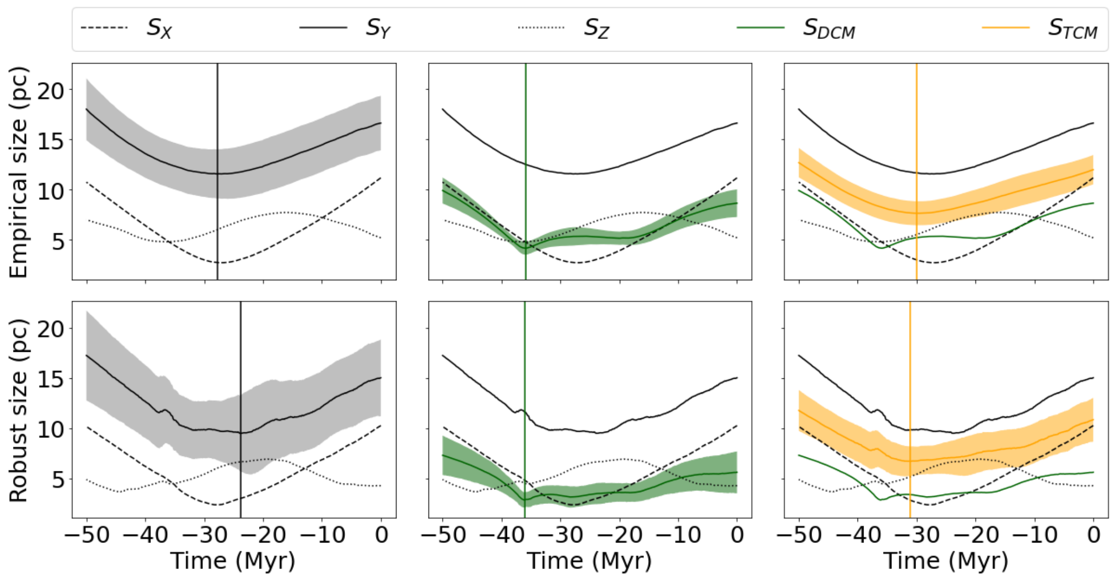

Caption/Notes. Same as Figure 4.3.

Figure 4.5.: Dynamical traceback age distribution with the UVES+ RV sample

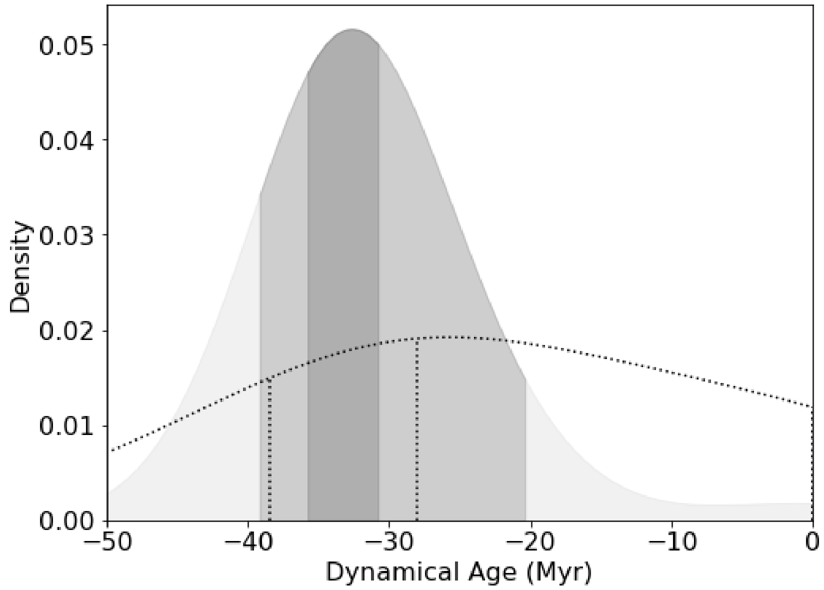

Caption/Notes. The distribution of dynamical ages derived from 1000 bootstrap repetitions utilizing the S_{TCM} size estimator. The color-coded regions highlight the 68%, 95%, and 99.7% highest-density intervals. The distribution acquired with the S_{DCM} size estimator is represented by the dashed lines.

Figure 4.6.: Dynamical traceback age distribution with the RV All sample

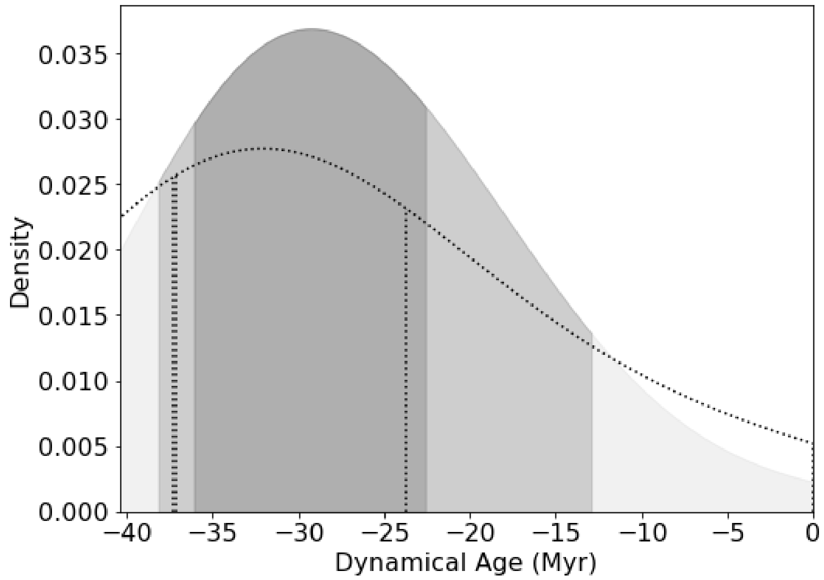

Caption/Notes. Same as Figure 4.5.

Figure 4.7.: Reconstruction of traceback result for Carina from Kerr et al. (2022)

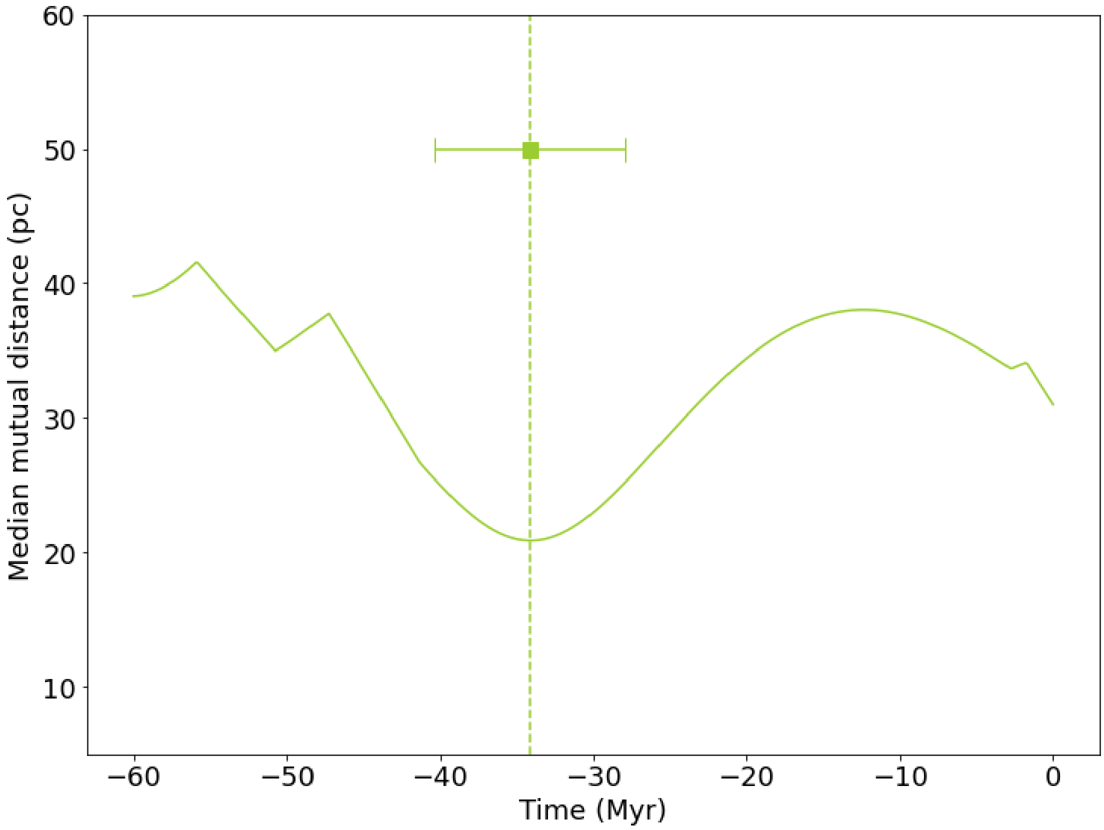

Figure 4.8.: CMD for Carina with the UVES+ RV sample

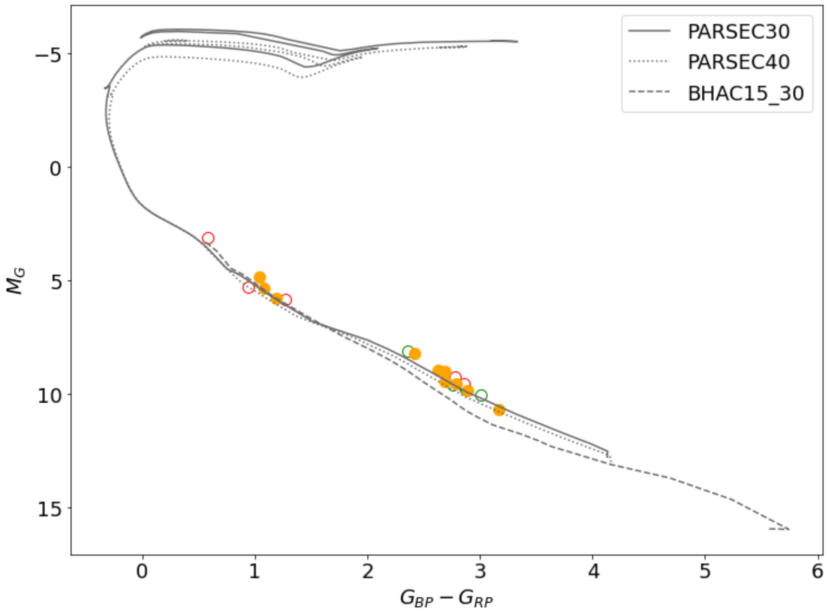

Caption/Notes. The colors indicate again the stars that are chosen for the final computations (orange), the rejected ones due to large Mahalanobis distance (green), and because of significantly differing orbits (red).

Figure 4.9.: CMD for Carina with the RV All sample

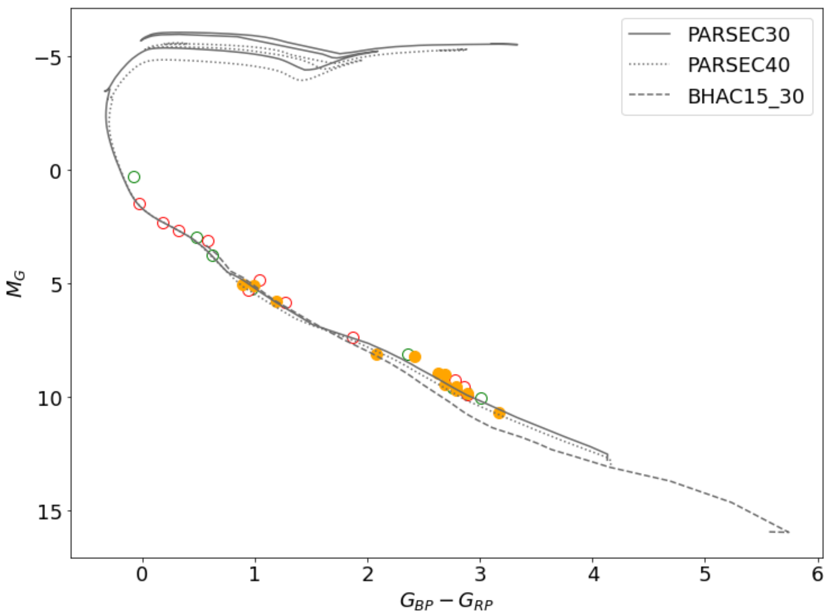

Caption/Notes. Same as Figure 4.8.

Figure 4.10.: CMD for Carina stars from Kerr et al. (2022) sample.

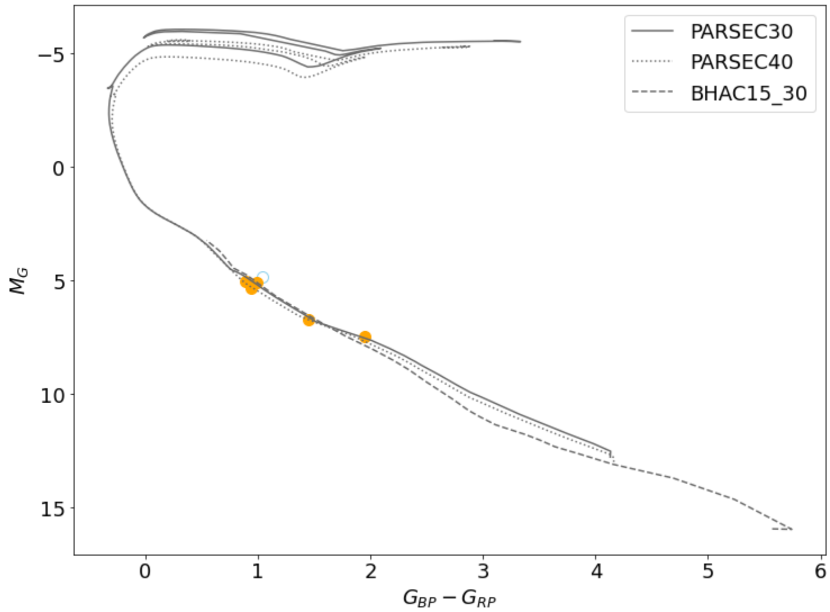

Caption/Notes. CMD for reclustered Carina members passing the cuts applied by Kerr et al. (2022). The orange stars are the chosen candidates for the dynamical age computation, while the blue one marks the star excluded due to an individual age estimate of < 10 Myr.

Figure 4.11.: Isochronal age estimates.

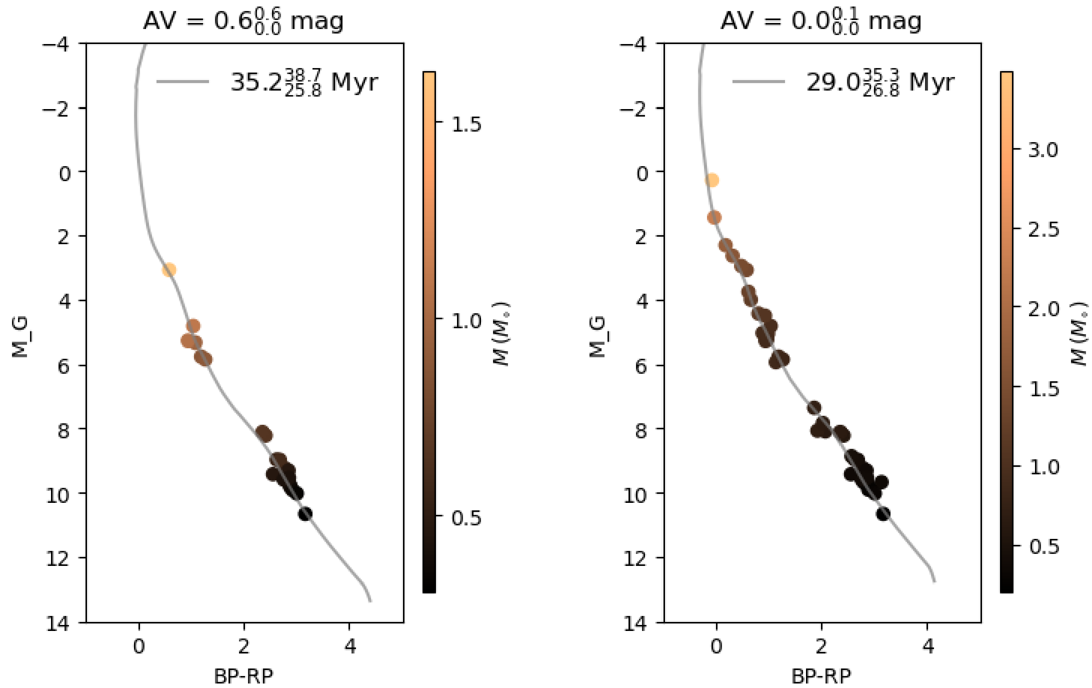

Caption/Notes. Left: Isochrone fitting to UVES+ sample. Right: Isochrone fitting to the RV All sample. Extinction is considered. Stellar mass is color-coded.

Figure 4.12.: Orbits of young local associations

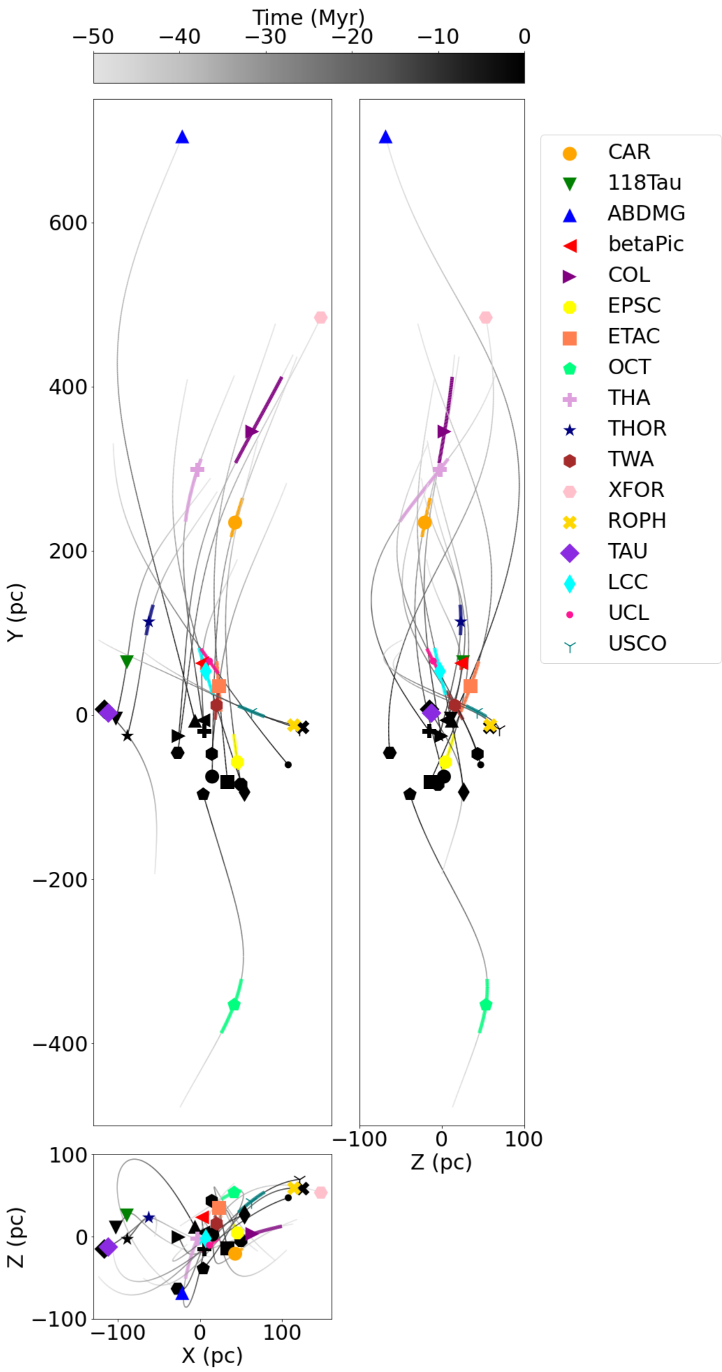

Caption/Notes. Orbits of YLAs color-coded as a function of time. The present (black markers) and birth time (colored markers) positions are indicated.

Figure 4.13.: Orbits of YLAS with common origin

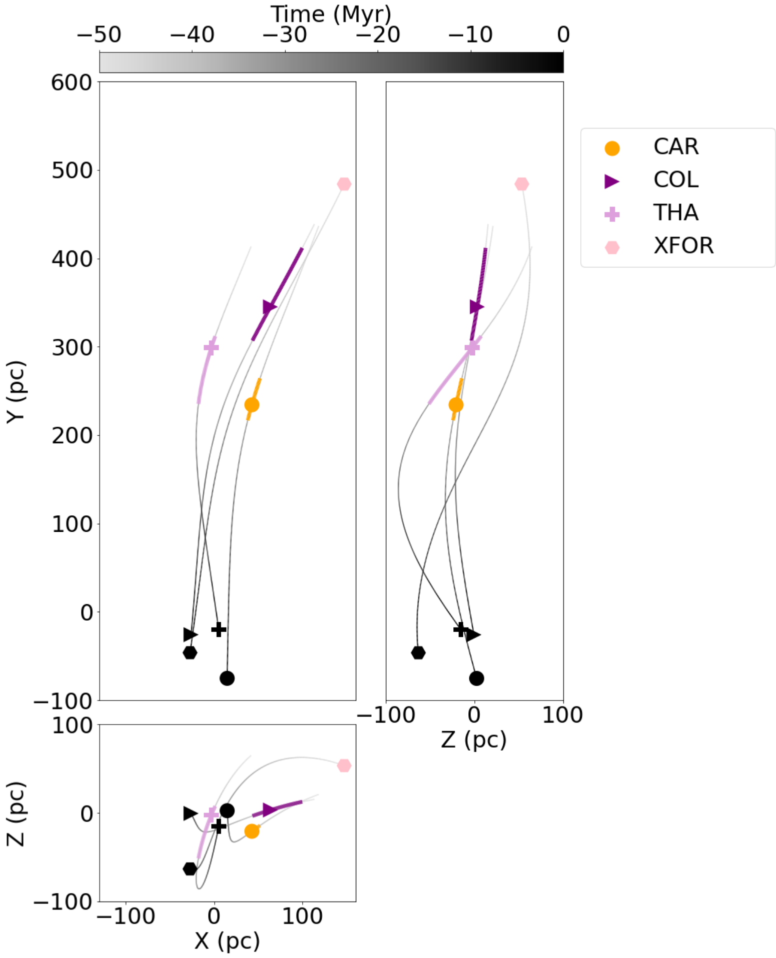

Caption/Notes. The orbits of the mean positions of the associations that share, according to this investigation, a common origin.

5. Discussion

In this chapter, I engage in a comprehensive analysis of the results presented in the previous chapter. First, I compare the outcome from Section 4 with relevant studies in the existing literature. I then provide possible explanations for observed differences or inconclusive results. In addition, I outline future prospects for the study of YLAs.

5.1. Comparison of results from this work

I employed diverse strategies to determine the dynamical traceback age of Carina, and the outcomes varied depending on the samples and size estimators utilized. The final age estimate for Carina obtained from my work is $32.7^{+3.1}_{-1.9}$ Myr. This determination is based on a sample of 10 bona fide members with new ground-based RV measurements and computed with the S_{TCM} size estimator.

I further applied the strategy to an alternative sample, consisting of 12 stars that have available RV measurements from UVES, *Gaia* DR3, and APOGEE. The analysis yielded an age estimate of 31^{+5}_{-9} Myr. However, it is important to note that I do not consider this result to be the outcome of my thesis. Despite the larger sample, I rely on the advantages offered by the UVES+ sample in two ways: 1) the homogeneity of the RV sample and 2) the precision of the RV measurements.

For comparison, I reconstructed the dynamical age investigation of Kerr et al. (2022). Applying their strategy to their data resulted in an age estimate of 34^{+6}_{-6} Myr obtained from tracing back 5 stars. This result is consistent with that obtained by applying the strategy of this work within the uncertainties. However, it is significantly less precise. Possible explanations include the smaller sample employed, the heterogeneous RV data, and the choice of the size estimator. Of the 5 stars used to replicate their study, three with *Gaia* DR3 IDs 5216440061069982592, 5343936233991963392, and 5297100607744079872 were not included in my dynamical age investigations because precise RV measurements are not available from the sources used (error > 1.6 km s^{-1}). However, I used stars with IDs 4621305817457618176 and 5219351911459314048 for the study with the RV All sample. The authors employed the median mutual distance between stars at each time step to determine the dynamical age from the minima of the respective curves. Applying the strategy used in this work to this selection of 5 stars resulted in a dynamical age of 22.9^{+8}_{-4} Myr, which is younger but still agrees within the uncertainties. This demonstrates that the choice of size estimator can have a significant impact on the resulting dynamical age.

A remarkable level of consistency is observed in the comparison between the isochronal age estimates provided by S. Ratzenböck ($35.2^{+38.7}_{-25.8}$ Myr for the UVES+ sample and $29^{+35.3}_{-26.8}$ Myr for the RV All sample; see Figure 4.11) and the dynamical age estimates obtained. This outcome is particularly significant because the methodology employed in this study is independent of evolutionary models and fundamentally distinct in its construction.

Overall, comparing the results indicates consistency among different strategies and samples, with minor variations arising from the sample size, available data, and employed strategy. These findings provide a robust age estimate for Carina that allows us to investigate its origin.

5.2. Comparison with other studies

In Table 5.1, I have compiled previous age estimates from the literature to compare with the result of this study. Bell et al. (2015) provided the first reliable age estimate for Carina by semi-empirical isochrone fitting to 12 members. The age of 45^{+11}_{-7} obtained by them is the oldest age estimate in the literature and older than the estimate obtained in this study.

Miret-Roig et al. (2018) conducted the first dynamical traceback study to narrow down the age of Carina. They analyzed nine YLAs using astrometry data from *Gaia* DR1 and ground-based radial velocities from the literature. Due to high observational errors, they obtained only a lower limit on the age of the association, which was 28 Myr, consistent with the results of this work. In addition, Booth et al. (2021) calculated a kinematic age based on the mutual distances between the stars considered and found that it must be younger than about 20 Myr. This result is at odds with the results of my work. However, the authors acknowledged that the uncertainties are substantial, so they cannot draw definitive conclusions. Their investigation did not reveal a distinct minimum in the estimated size but a plateau in the first 20 Myr, followed by an increase in the size of the association (see their Figure 5). Kerr et al. (2022) performed a dynamical traceback investigation in what they refer to as the extensive Austral complex. This complex encompasses multiple young stellar associations in the solar neighborhood, including the Carina association. They estimated the age of the Carina association to be $32.9^{+8.2}_{-8.2}$ Myr. Although the authors used a different sample, a different source of radial velocities, different selection criteria, and a different size estimator, their result is consistent with the results of this thesis. They mention that because of the high age of the considered associations (compared to Cepheus Far North) and the presence of marginally virialized clusters, not all of their dynamic age estimates shown in Figure 8 of their paper are reliable. However, they did not indicate whether the estimate for Carina is reliable, but it is the estimate with the highest uncertainty in their studies. Nonetheless, they found a clear minimum where the association's size is more than twice the minimum size derived from the analysis of this work (see Figure 4.3).

Recently, there have been suggestions in the literature that Carina is younger, inferred from other age-determination methods. Schneider et al. (2019) estimated an age for Carina of about 22 Myr by comparing λ6707 lithium abundances of Carina members with those of β Pictoris and the Tucana-Horologium and found that the abundances are more similar to the those of β Pictoris. Booth et al. (2021) determined the age of Carina to be $13.3^{+1.1}_{-0.6}$ based on isochrone fitting obtained by employing a Bayesian inference code that leverages the models of PARSEC. The most recent study by Kerr et al. (2022) yielded an age of $14.5^{+0.7}_{-0.7}$ Myr for Carina by fitting an isochrone from the BHAC15 models. However, these models are not preferred by the authors. It is evident that the isochronal age estimates exhibit significant differences depending on the employed model.

Conversely, there are also age estimates in the literature, including Ujjwal et al. (2020) and Kerr et al. (2022), which are based on isochronal fitting and are consistent with the estimate derived from this study within the uncertainties. Ujjwal et al. (2020) estimated Carina's age to be in the range of 3-34.5 Myr with a mean age of 16.64 Myr using *Gaia* DR2 CMD with a overplotted grid of MIST isochrones. The isochronal age estimate from Kerr et al. (2022) employing the PARSEC, which is favored by the authors, is $37^{+2.6}_{-2.6}$ Myr.

Notably, the minimum size of the Carina association inferred from the S_{TCM} estimator is about 6 pc, aligning with the minimum sizes determined in Galli et al. (2023) and Miret-Roig et al. (2020) (about 4 pc for Tucana-Horologium and 7 pc for β Pictoris).

Interestingly, a recent paper Miret-Roig et al. (2023) has shown that traceback ages are generally underestimated, suggesting that also the Carina association might be older than suggested by this study. Comparing the isochronal ages obtained by S. Ratzenböck for this thesis to the dynamical ages of this work, I can observe this discrepancy only in the UVES+ sample, but the difference is not significant. Further investigations are required to clarify this.

5.3. Caveats

The dynamical traceback method is sensitive to the inclusion of non-members or stars with inaccurate measurements, which can significantly affect the obtained results. In the case of the Carina association, its membership is not well-established. Overlaps with the Columba and Tucana-Horologium associations may lead to misidentifications. The reclustering by Kerr et al. (2022) of their initial sample selection has shown that some previously cataloged Carina members are, in fact, members of the old Platais 8 open cluster, and vice versa for Tucana-Horologium and Columba. Therefore, a comprehensive investigation of the membership status of Carina and its neighboring associations is needed to shed light on their origins and ages.

Furthermore, this work has demonstrated that the choice of size estimator plays a crucial role in determining the resulting dynamical age. To obtain a robust estimate of the size, it is important that the estimator considers dispersions in all directions and possesses good outlier handling capabilities.

5.4. Perspectives

To determine more accurate dynamical ages for nearby associations, we need high-confidence members and high-precision RV measurements. To achieve a more accurate understanding of cluster membership in this region, it is recommended to employ new clustering methods such as SigMa (Ratzenböck et al., 2022). These methods can provide additional clarity regarding the precise membership of the clusters. Moreover, the upcoming 4MOST (4-meter Multi-Object Spectroscopic Telescope) spectroscopic survey facility and the WEAVE (WHT Enhanced Area Velocity Explorer) spectrograph, along with complementary devoted proposals like the RV measurements obtained for this study, will deliver new reliable RV measurements in the future. Furthermore, it is worth mentioning that the upcoming releases of the *Gaia* mission will enhance the precision of RV measurements. These improved measurements would allow a more accurate traceback investigation.

Table 5.1.: Literature age estimates for Carina.

Reference	Age (Myr)	Method
Torres et al. (2008)	~ 40	Li λ6707 EW and $V - I_c$ CMD
Bell et al. (2015)	45^{+11}_{-7}	Isochronal age
Miret-Roig et al. (2018)	> 28	Dynamical traceback age
Schneider et al. (2019)	~ 22	Li evolution
Ujjwal et al. (2020)	16.64 (3-34.5)	Isochronal age
Booth et al. (2021)	$13.3^{+1.1}_{-0.6}$	Isochronal age
Booth et al. (2021)	~ 20 Myr	Dynamical traceback age
Kerr et al. (2022)	$32.9^{+8.2}_{-8.2}$	Dynamical traceback age
Kerr et al. (2022)	$37^{+2.6}_{-2.6}$	Isochronal age (PARSEC)
Kerr et al. (2022)	$14.5^{+0.7}_{-0.7}$	Isochronal age (BHAC15)
Kerr et al. (2022)	$27.7^{+2.1}_{-2.1}$	Isochronal age (DSEP-Magnetic)
This work	$\mathbf{32.7^{+3.1}_{-1.9}}$	**Dynamical traceback age**

6. Conclusion

In this thesis, I derived a dynamical traceback age of the Carina young local association of $32.7^{+3.1}_{-1.9}$ Myr. This result is consistent with several age estimates reported in the literature using isochrone fitting and dynamical ages. By establishing a reliable age estimate, I was able to investigate the origin of Carina in relation to 16 nearby young stellar associations. The analysis revealed that Carina shares a similar path and origin with the Columba, Tucana-Horologium, and χ^1 Fornacis young stellar associations, which supports previous suggestions in the literature.

Accurate measurements of astrometry and radial velocities are crucial components for obtaining precise dynamical ages. To achieve this, I utilized the precise astrometric data from the *Gaia* DR3 catalog and new ground-based radial velocity measurements. The radial velocity measurements of 29 stars were obtained by combining high-resolution spectra from public archives with new observations using the UVES spectrograph. These measurements not only align well with published results from other projects but also offer improved precision and provide initial radial velocity data for four stars. This approach allowed me to create a consistent and accurate dataset to investigate the kinematic properties of the Carina association.

To ensure reliable results, I carefully selected members with high-quality data and identified the most probable kinematic members of the Carina association based on the stars' 3D space motion and the convergence of their stellar orbits in the past. Subsequently, I conducted an extensive analysis to explore the dynamical age of the association, employing various samples of stars and metrics to determine the minimum size of the association. Remarkably, the dynamical ages derived from the different data sets investigated in this analysis exhibited agreement within a margin of 2 Myr when employing the same size estimation method. Moreover, in my analysis, estimating the association's size based on the trace of the covariance matrix provided the most robust estimate of the dynamical age of Carina.

The findings of this thesis highlight the necessity of a clean sample of cluster members, highly accurate data, and a reliable size estimator when employing the traceback method to derive stellar age estimates. Similar conclusions have been drawn by Miret-Roig et al. (2020) for the β Pic moving group ($18.5^{+2.0}_{-2.2}$ Myr) and by Galli et al. (2023) for the Tuc-Hor association ($38.5^{+1.6}_{-8.0}$ Myr). These results underscore the feasibility of deriving reliable dynamical ages for young local associations aged 30-40 Myr based on the dynamical traceback method. They represent a significant step towards constructing a self-consistent age scale, independent of stellar models, for young stellar associations in the solar neighborhood.

Bibliography

Abdurro'uf et al. (Apr. 2022). 'The Seventeenth Data Release of the Sloan Digital Sky Surveys: Complete Release of MaNGA, MaStar, and APOGEE-2 Data'. In: *Astrophys. J. Suppl. Ser.* 259(2), 35, p. 35. DOI: 10.3847/1538-4365/ac4414. arXiv: 2112.02026 [astro-ph.GA].

Ambartsumian, V. A. (Aug. 1947). 'The Evolution of Stars and Astrophysics'. In: *Communications of the Byurakan Astrophysical Observatory* 69(1), pp. 127–139. DOI: 10.52526/25792776-22.69.1-127.

Astropy Collaboration et al. (Oct. 2013). 'Astropy: A community Python package for astronomy'. In: *Astron. Astrophys.* 558, A33, A33. DOI: 10.1051/0004-6361/201322068. arXiv: 1307.6212 [astro-ph.IM].

Baraffe, Isabelle et al. (2015). 'New evolutionary models for pre-main sequence and main sequence low-mass stars down to the hydrogen-burning limit'. In: *A&A* 577, A42. DOI: 10.1051/0004-6361/201425481. URL: https://doi.org/10.1051/0004-6361/201425481.

Barnes, Sydney A. (Nov. 2007). 'Ages for Illustrative Field Stars Using Gyrochronology: Viability, Limitations, and Errors'. In: *Astrophys. J.* 669(2), pp. 1167–1189. DOI: 10.1086/519295.

Barrado, D. (2016). 'Clusters: Age Scales for Stellar Physics'. In: *EAS Publications Series* 80-81. Ed. by E. Moraux, Y. Lebreton and C. Charbonnel, pp. 115–175. DOI: 10.1051/eas/1680005. URL: https://doi.org/10.1051\%2Feas\%2F1680005.

Bell, Cameron P. M., Eric E. Mamajek and Tim Naylor (Sept. 2015). 'A self-consistent, absolute isochronal age scale for young moving groups in the solar neighbourhood'. In: *Monthly Notices of the Royal Astronomical Society* 454(1), pp. 593–614. ISSN: 0035-8711. DOI: 10.1093/mnras/stv1981. eprint: https://academic.oup.com/mnras/article-pdf/454/1/593/13769516/stv1981.pdf. URL: https://doi.org/10.1093/mnras/stv1981.

Binks, A. S. et al. (July 2022). 'The Gaia-ESO survey: constraining evolutionary models and ages for young low mass stars with measurements of lithium depletion and rotation'. In: *Mon. Not. R. Astron. Soc.* 513(4), pp. 5727–5751. DOI: 10.1093/mnras/stac1245. arXiv: 2204.05820 [astro-ph.SR].

Blaauw, Adriaan (Jan. 1964). 'The O Associations in the Solar Neighborhood'. In: *Annu. Rev. Astron. Astrophys.* 2, p. 213. DOI: 10.1146/annurev.aa.02.090164.001241.

Booth, Mark, Carlos del Burgo and Valeri V. Hambaryan (Jan. 2021). 'The age of the carina young association and potential membership of HD 95086'. In: *Mon. Not. R. Astron. Soc.* 500(4), pp. 5552–5560. DOI: 10.1093/mnras/staa3631. arXiv: 2011.07083 [astro-ph.SR].

Bovy, Jo (Feb. 2015). 'galpy: A python LIBRARY FOR GALACTIC DYNAMICS , journal = The Astrophysical Journal Supplement Series'. In: 216(2), p. 29. DOI: 10.1088/0067-0049/216/2/29. URL: https://doi.org/10.1088\%2F0067-0049\%2F216\%2F2\%2F29.

Bressan, Alessandro et al. (Nov. 2012). 'PARSEC: stellar tracks and isochrones with the PAdova and TRieste Stellar Evolution Code'. In: *Mon. Not. R. Astron. Soc.* 427(1), pp. 127–145. DOI: 10.1111/j.1365-2966.2012.21948.x. arXiv: 1208.4498 [astro-ph.SR].

Cánovas, H. et al. (June 2019). 'Census of ρ Ophiuchi candidate members from Gaia Data Release 2'. In: *Astron. Astrophys.* 626, A80, A80. DOI: 10.1051/0004-6361/201935321. arXiv: 1902.07600 [astro-ph.EP].

Casagrande, L. et al. (2011). 'New constraints on the chemical evolution of the solar neighbourhood and Galactic disc(s) - Improved astrophysical parameters for the Geneva-Copenhagen Survey'. In: *A&A* 530, A138. DOI: 10.1051/0004-6361/201016276. URL: https://doi.org/10.1051/0004-6361/201016276.

Choi, Jieun et al. (June 2016). 'Mesa Isochrones and Stellar Tracks (MIST). I. Solar-scaled Models'. In: *Astrophys. J.* 823(2), 102, p. 102. DOI: 10.3847/0004-637X/823/2/102.

de Zeeuw, P. T. et al. (Jan. 1999). 'A HIPPARCOS Census of the Nearby OB Associations'. In: *Astron. J.* 117(1), pp. 354–399. DOI: 10.1086/300682. arXiv: astro-ph/9809227 [astro-ph].

Dekker, Hans et al. (Aug. 2000). 'Design, construction, and performance of UVES, the echelle spectrograph for the UT2 Kueyen Telescope at the ESO Paranal Observatory'. In: *Optical and IR Telescope Instrumentation and Detectors*. Ed. by Masanori Iye and Alan F. Moorwood. Vol. 4008. Society of Photo-Optical Instrumentation Engineers (SPIE) Conference Series, pp. 534–545. DOI: 10.1117/12.395512.

Dotter, Aaron (Jan. 2016). 'MESA Isochrones and Stellar Tracks (MIST) 0: Methods for the Construction of Stellar Isochrones'. In: *Astrophys. J. Suppl. Ser.* 222(1), 8, p. 8. DOI: 10.3847/0067-0049/222/1/8.

Ducourant, C. et al. (Mar. 2014). 'The TW Hydrae association: trigonometric parallaxes and kinematic analysis'. In: *Astron. Astrophys.* 563, A121, A121. DOI: 10.1051/0004-6361/201322075. arXiv: 1401.1935 [astro-ph.SR].

Elliott, P. et al. (2014). 'Search for associations containing young stars (SACY) - V. Is multiplicity universal? Tight multiple systems'. In: *A&A* 568, A26. DOI: 10.1051/0004-6361/201423856. URL: https://doi.org/10.1051/0004-6361/201423856.

Elliott, P. et al. (2015). 'Search for associations containing young stars (SACY) - VI. Is multiplicity universal? Stellar multiplicity in the range 3-1000 au from adaptive-optics observations'. In: *A&A* 580, A88. DOI: 10.1051/0004-6361/201525794. URL: https://doi.org/10.1051/0004-6361/201525794.

Fabricius, C. et al. (May 2021). 'Gaia Early Data Release 3. Catalogue validation'. In: *Astron. Astrophys.* 649, A5, A5. DOI: 10.1051/0004-6361/202039834. arXiv: 2012.06242 [astro-ph.GA].

Fernández, D., F. Figueras and J. Torra (Mar. 2008). 'On the kinematic evolution of young local associations and the Scorpius-Centaurus complex'. In: *Astron. Astrophys.* 480(3), pp. 735–751. DOI: 10.1051/0004-6361:20077720. arXiv: 0801.0605 [astro-ph].

Gagné, Jonathan and Jacqueline K. Faherty (Aug. 2018). 'BANYAN. XIII. A First Look at Nearby Young Associations with Gaia Data Release 2'. In: *Astrophys. J.* 862(2), 138, p. 138. DOI: 10.3847/1538-4357/aaca2e. arXiv: 1805.11715 [astro-ph.SR].

Gagné, Jonathan et al. (Mar. 2018a). 'BANYAN. XI. The BANYAN Σ Multivariate Bayesian Algorithm to Identify Members of Young Associations with 150 pc'. In: *Astrophys. J.* 856(1), 23, p. 23. DOI: 10.3847/1538-4357/aaae09. arXiv: 1801.09051 [astro-ph.SR].

Gagné, Jonathan et al. (June 2018b). 'BANYAN. XII. New Members of Nearby Young Associations from GAIA-Tycho Data'. In: *Astrophys. J.* 860(1), 43, p. 43. DOI: 10.3847/1538-4357/aac2b8. arXiv: 1804.03093 [astro-ph.SR].

Gagné, Jonathan et al. (Feb. 2014). 'BANYAN. II. VERY LOW MASS AND SUBSTELLAR CANDIDATE MEMBERS TO NEARBY, YOUNG KINEMATIC GROUPS WITH PREVIOUSLY KNOWN SIGNS OF YOUTH'. In: *The Astrophysical Journal* 783(2), p. 121. DOI: 10.1088/0004-637X/783/2/121. URL: https://dx.doi.org/10.1088/0004-637X/783/2/121.

Gaia Collaboration et al. (Nov. 2016). 'The Gaia mission'. In: *Astron. Astrophys.* 595, A1, A1. DOI: 10.1051/0004-6361/201629272. arXiv: 1609.04153 [astro-ph.IM].

Gaia Collaboration et al. (July 2022). 'Gaia Data Release 3: Summary of the content and survey properties'. In: *arXiv e-prints*, arXiv:2208.00211, arXiv:2208.00211. DOI: 10.48550/arXiv.2208.00211. arXiv: 2208.00211 [astro-ph.GA].

Galindo-Guil, F. J. et al. (2022). 'Lithium depletion boundary, stellar associations, and Gaia'. In: *A&A* 664, A70. DOI: 10.1051/0004-6361/202141114. URL: https://doi.org/10.1051/0004-6361/202141114.

Galli, P. A. B. et al. (Oct. 2019). 'Structure and kinematics of the Taurus star-forming region from Gaia-DR2 and VLBI astrometry'. In: *Astron. Astrophys.* 630, A137, A137. DOI: 10.1051/0004-6361/201935928. arXiv: 1909.01118 [astro-ph.SR].

Galli, P. A. B. et al. (Feb. 2020). 'Corona-Australis DANCe. I. Revisiting the census of stars with Gaia-DR2 data'. In: *Astron. Astrophys.* 634, A98, A98. DOI: 10.1051/0004-6361/201936708. arXiv: 2001.05190 [astro-ph.SR].

Galli, P. A. B. et al. (Oct. 2021). 'χ^1 Fornacis cluster DANCe. Census of stars, structure, and kinematics of the cluster with Gaia-EDR3'. In: *Astron. Astrophys.* 654, A122, A122. DOI: 10.1051/0004-6361/202141366. arXiv: 2108.11208 [astro-ph.SR].

Galli, Phillip A. B. et al. (Apr. 2023). 'Dynamical age of the Tucana-Horologium young stellar association'. In: *Mon. Not. R. Astron. Soc.* 520(4), pp. 6245–6255. DOI: 10.1093/mnras/stad520. arXiv: 2302.12036 [astro-ph.SR].

Høg, E. et al. (Mar. 2000). 'The Tycho-2 catalogue of the 2.5 million brightest stars'. In: *Astron. Astrophys.* 355, pp. L27–L30.

Hughes, David (Dec. 2006). 'The Introduction of Absolute Magnitude (1902 - 1922)'. In: *Journal of Astronomical History and Heritage* 9. DOI: 10.3724/SP.J.1440-2807.2006.02.06.

Jayawardhana, Ray (Apr. 2000). 'New Stars on the Block'. In: *Science* 288, p. 64. DOI: 10.1126/science.288.5463.64. arXiv: astro-ph/0005223 [astro-ph].

Kenyon, Scott J. and Lee Hartmann (Nov. 1995). 'Pre-Main-Sequence Evolution in the Taurus-Auriga Molecular Cloud'. In: *Astrophys. J. Suppl. Ser.* 101, p. 117. DOI: 10.1086/192235.

Kerr, Ronan et al. (Oct. 2022). 'SPYGLASS III: The Fornax-Horologium Association and its Traceback History within the Austral Complex'. In: *arXiv e-prints*, arXiv:2211.00123, arXiv:2211.00123. arXiv: 2211.00123 [astro-ph.GA].

Kharchenko, N. V. et al. (Oct. 2013). 'Global survey of star clusters in the Milky Way. II. The catalogue of basic parameters'. In: *Astron. Astrophys.* 558, A53, A53. DOI: 10.1051/0004-6361/201322302. arXiv: 1308.5822 [astro-ph.GA].

Kraus, Adam L. et al. (May 2014). 'A STELLAR CENSUS OF THE TUCANA–HOROLOGIUM MOVING GROUP'. In: *The Astronomical Journal* 147(6), p. 146. DOI: 10.1088/0004-6256/147/6/146. URL: https://dx.doi.org/10.1088/0004-6256/147/6/146.

Lopez Martí, B. et al. (2013). 'Proper motions of young stars in Chamaeleon - I. A Virtual Observatory study of spectroscopically confirmed members'. In: *A&A* 551, A46. DOI: 10.1051/0004-6361/201220128. URL: https://doi.org/10.1051/0004-6361/201220128.

Luri, X. et al. (Aug. 2018). 'Gaia Data Release 2. Using Gaia parallaxes'. In: *Astron. Astrophys.* 616, A9, A9. DOI: 10.1051/0004-6361/201832964. arXiv: 1804.09376 [astro-ph.IM].

Majewski, Steven R. et al. (Sept. 2017). 'The Apache Point Observatory Galactic Evolution Experiment (APOGEE)'. In: *Astron. J.* 154(3), 94, p. 94. DOI: 10.3847/1538-3881/aa784d. arXiv: 1509.05420 [astro-ph.IM].

Malo, Lison et al. (Dec. 2013). 'BAYESIAN ANALYSIS TO IDENTIFY NEW STAR CANDIDATES IN NEARBY YOUNG STELLAR KINEMATIC GROUPS*'. In: *The Astrophysical Journal* 762(2), p. 88. DOI: 10.1088/0004-637X/762/2/88. URL: https://dx.doi.org/10.1088/0004-637X/762/2/88.

Malo, Lison et al. (June 2014). 'BANYAN. III. Radial Velocity, Rotation, and X-Ray Emission of Low-mass Star Candidates in Nearby Young Kinematic Groups'. In: *Astrophys. J.* 788(1), 81, p. 81. DOI: 10.1088/0004-637X/788/1/81. arXiv: 1402.6053 [astro-ph.SR].

Mamajek, Eric (Mar. 2016). 'A New Candidate Young Stellar Group at d=121 pc Associated with 118 Tauri'. In: DOI: 10.6084/m9.figshare.3122689.v1. URL: https://figshare.com/articles/figure/A_New_Candidate_Young_Stellar_Group_at_d_121_pc_Associated_with_118_Tauri/3122689.

Mamajek, Eric E. (Jan. 2016). 'A Pre-Gaia Census of Nearby Stellar Groups'. In: *Young Stars & Planets Near the Sun.* Ed. by J. H. Kastner, B. Stelzer and S. A. Metchev. Vol. 314, pp. 21–26. DOI: 10.1017/S1743921315006250. arXiv: 1507.06697 [astro-ph.SR].

Mamajek, Eric E. and Cameron P. M. Bell (Dec. 2014). 'On the age of the β Pictoris moving group'. In: *Mon. Not. R. Astron. Soc.* 445(3), pp. 2169–2180. DOI: 10.1093/mnras/stu1894. arXiv: 1409.2737 [astro-ph.SR].

Marigo, Paola et al. (Jan. 2017). 'A New Generation of PARSEC-COLIBRI Stellar Isochrones Including the TP-AGB Phase'. In: *Astrophys. J.* 835(1), 77, p. 77. DOI: 10.3847/1538-4357/835/1/77.

Miret-Roig, N. et al. (Oct. 2018). 'Dynamical ages of the young local associations with Gaia (Corrigendum)'. In: *Astron. Astrophys.* 618, C7, p. C7. DOI: 10.1051/0004-6361/201731976e.

Miret-Roig, N. et al. (Oct. 2020). 'Dynamical traceback age of the β Pictoris moving group'. In: *Astron. Astrophys.* 642, A179, A179. DOI: 10.1051/0004-6361/202038765. arXiv: 2007.10997 [astro-ph.GA].

Miret-Roig, N. et al. (Nov. 2022). 'The star formation history of Upper Scorpius and Ophiuchus. A 7D picture: positions, kinematics, and dynamical traceback ages'. In: *Astron. Astrophys.* 667, A163, A163. DOI: 10.1051/0004-6361/202244709. arXiv: 2209.12938 [astro-ph.GA].

Miret-Roig, N. et al. (2023). 'Reconciling stellar ages: A new observable for probing star formation and dispersion'. In: *Submitted*.

Moór, A. et al. (Oct. 2013). 'A Resolved Debris Disk around the Candidate Planet-hosting Star HD 95086'. In: *Astrophys. J. Lett.* 775(2), L51, p. L51. DOI: 10.1088/2041-8205/775/2/L51. arXiv: 1309.1675 [astro-ph.SR].

Murphy, S. J. and W. A. Lawson (Jan. 2015). 'VizieR Online Data Catalog: Low-mass members of the Octans association (Murphy+, 2015)'. In: *VizieR Online Data Catalog*, J/MNRAS/447/1267, J/MNRAS/447/1267.

Murphy, S. J., W. A. Lawson and M. S. Bessell (Sept. 2013). 'VizieR Online Data Catalog: Membership of the {epsilon} Cha association (Murphy+, 2013)'. In: *VizieR Online Data Catalog*, J/MNRAS/435/1325, J/MNRAS/435/1325.

Pecaut, Mark J. and Eric E. Mamajek (Sept. 2013). 'Intrinsic Colors, Temperatures, and Bolometric Corrections of Pre-main-sequence Stars'. In: *Astrophys. J. Suppl. Ser.* 208(1), 9, p. 9. DOI: 10.1088/0067-0049/208/1/9. arXiv: 1307.2657 [astro-ph.SR].

Perryman, M. A. C. et al. (July 1997). 'The HIPPARCOS Catalogue'. In: *Astron. Astrophys.* 323, pp. L49–L52.

Pöhnl, H. and E. Paunzen (May 2010). 'A statistical method to determine open cluster metallicities'. In: *Astron. Astrophys.* 514, A81, A81. DOI: 10.1051/0004-6361/200810855. arXiv: 1002.4503 [astro-ph.GA].

Ratzenböck, Sebastian et al. (Nov. 2022). 'Significance Mode Analysis (SigMA) for hierarchical structures. An application to the Sco-Cen OB association'. In: *arXiv e-prints*, arXiv:2211.14225, arXiv:2211.14225. DOI: 10.48550/arXiv.2211.14225. arXiv: 2211.14225 [astro-ph.GA].

Ratzenböck, Sebastian et al. (Feb. 2023). 'The star formation history of the Sco-Cen association. Coherent star formation patterns in space and time'. In: *arXiv e-prints*, arXiv:2302.07853, arXiv:2302.07853. DOI: 10.48550/arXiv.2302.07853. arXiv: 2302.07853 [astro-ph.SR].

Rebolo, Rafael, Eduardo L. Martin and Antonio Magazzu (Apr. 1992). 'Spectroscopy of a Brown Dwarf Candidate in the alpha Persei Open Cluster'. In: *Astrophys. J. Lett.* 389, p. L83. DOI: 10.1086/186354.

Riaz, Basmah, John E. Gizis and James Harvin (Aug. 2006). 'Identification of New M Dwarfs in the Solar Neighborhood'. In: *Astron. J.* 132(2), pp. 866–872. DOI: 10.1086/505632. arXiv: astro-ph/0606617 [astro-ph].

Riedel, Adric R. et al. (Mar. 2017). 'LACEwING: A New Moving Group Analysis Code'. In: *Astron. J.* 153(3), 95, p. 95. DOI: 10.3847/1538-3881/153/3/95. arXiv: 1702.02219 [astro-ph.SR].

Schneider, Adam C. et al. (June 2019). 'ACRONYM. III. Radial Velocities for 336 Candidate Young Low-mass Stars in the Solar Neighborhood, Including 77 Newly Confirmed Young Moving Group Members'. In: *Astron. J.* 157(6), 234, p. 234. DOI: 10.3847/1538-3881/ab1a26. arXiv: 1904.07193 [astro-ph.SR].

Schönrich, Ralph, James Binney and Walter Dehnen (Apr. 2010). 'Local kinematics and the local standard of rest'. In: *Monthly Notices of the Royal Astronomical Society* 403(4), pp. 1829–1833. DOI: 10.1111/j.1365-2966.2010.16253.x. URL: https://doi.org/10.1111\%2Fj.1365-2966.2010.16253.x.

Silverberg, Steven M. et al. (Oct. 2016). 'A NEW M DWARF DEBRIS DISK CANDIDATE IN A YOUNG MOVING GROUP DISCOVERED WITH DISK DETECTIVE'. In: *The Astrophysical Journal Letters* 830(2), p. L28. DOI: 10.3847/2041-8205/830/2/L28. URL: https://dx.doi.org/10.3847/2041-8205/830/2/L28.

Skrutskie, M. F. et al. (Feb. 2006). 'The Two Micron All Sky Survey (2MASS)'. In: *Astron. J.* 131(2), pp. 1163–1183. DOI: 10.1086/498708.

Soderblom, David R. (Aug. 2010). 'The Ages of Stars'. In: *Annual Review of Astronomy and Astrophysics* 48(1), pp. 581–629. DOI: 10.1146/annurev-astro-081309-130806. URL: https://doi.org/10.1146\%2Fannurev-astro-081309-130806.

Soubiran, C. et al. (2018). 'Gaia Data Release 2 - The catalogue of radial velocity standard stars'. In: *A&A* 616, A7. DOI: 10.1051/0004-6361/201832795. URL: https://doi.org/10.1051/0004-6361/201832795.

Torres, C. A. O. et al. (Jan. 2001). 'The Great Austral Nearby Young Association'. In: *Young Stars Near Earth: Progress and Prospects*. Ed. by Ray Jayawardhana and Thomas Greene. Vol. 244. Astronomical Society of the Pacific Conference Series, p. 43. DOI: 10.48550/arXiv.astro-ph/0105291. arXiv: astro-ph/0105291 [astro-ph].

Torres, C. A. O. et al. (Dec. 2006). 'Search for associations containing young stars (SACY). I. Sample and searching method'. In: *Astron. Astrophys.* 460(3), pp. 695–708. DOI: 10.1051/0004-6361:20065602. arXiv: astro-ph/0609258 [astro-ph].

Torres, C. A. O. et al. (2008). 'Young Nearby Loose Associations'. In: *Handbook of Star Forming Regions, Volume II*. Ed. by B. Reipurth. Vol. 5, p. 757. DOI: 10.48550/arXiv.0808.3362.

Ujjwal, K. et al. (Apr. 2020). 'Analysis of Membership Probability in Nearby Young Moving Groups with Gaia DR2'. In: *Astron. J.* 159(4), 166, p. 166. DOI: 10.3847/1538-3881/ab76d6. arXiv: 2002.04801 [astro-ph.SR].

Wenger, M. et al. (Apr. 2000). 'The SIMBAD astronomical database. The CDS reference database for astronomical objects'. In: *Astron. Astrophys. Suppl.* 143, pp. 9–22. DOI: 10.1051/aas:2000332. arXiv: astro-ph/0002110 [astro-ph].

Wilking, B. A., M. Gagne and L. E. Allen (Nov. 2008). 'VizieR Online Data Catalog: JKH photometry in LDN 1688 (Wilking+, 2008)'. In: *VizieR Online Data Catalog* 5, II/289, pp. 351–380.

Zuckerman, B. and Inseok Song (Sept. 2004). 'Young Stars Near the Sun'. In: *Annu. Rev. Astron. Astrophys.* 42(1), pp. 685–721. DOI: 10.1146/annurev.astro.42.053102.134111.

A. Appendix

A.1. Master Table

In this Appendix, I present the complete master table that I have compiled, which includes all the information utilized in this thesis for the 118 Carina members considered. To enhance readability and manage the large number of columns, I divided the table into multiple sections, each containing a subset of the columns. I provided a detailed description of the columns in Section 2.5.

Table A.1.: Columns 1-5

ID	*Gaia* DR3 ID	member_our	member_kerr	ra (deg)	dec (deg)
0	4634072762364274048	True	False	36.05	-76.56
1	4626843786944938880	True	True	48.99	-77.39
2	4615260912983205376	True	True	63.37	-84.14
3	4627516443247238912	True	False	66.84	-77.32
4	4651868358068062976	True	True	81.01	-71.16
5	4651909078695070848	True	True	81.04	-70.63
6	4759444786175885824	True	True	83.61	-60.1
7	4792149175429007360	True	True	88.12	-53.05
8	4621305817457618176	True	True	88.37	-81.95
9	5207595074138996608	True	True	92.22	-81.55
10	5481327629267108992	True	True	92.72	-61.5
11	5495052596695570816	True	True	94.8	-58.05
12	5261554496328279552	True	True	96.59	-75.28
13	5266729004207512320	True	True	100.08	-70.87
14	5496804462316135168	True	True	100.32	-56.27
15	5265670762922792960	True	True	100.94	-71.98
16	5266642318884581632	True	True	101.6	-70.63
17	5286310069347838080	True	True	104.58	-63.19
18	5208216951043609216	True	True	105.13	-79.7
19	5286978645433636480	True	True	105.17	-62.06
20	5287208409004384384	True	True	107.24	-60.98
21	5281448892220945536	True	True	108.82	-65.93
22	5293390756728204160	True	True	111.12	-59.37
23	5274939091892309120	True	True	114.01	-67.09
24	5287415735666649728	True	False	116.05	-64.97
25	5514007451307863808	True	True	119.92	-50.6
26	5277462269217606400	True	True	121.02	-63.28
27	5213934514587912320	True	True	121.65	-74.74
28	5320108854927493888	True	True	122.24	-54.35
29	5513493846240655360	True	True	122.59	-50.26
30	5271426397057175936	True	True	122.8	-66.94
31	5513520440678664192	True	True	122.95	-50.06
32	5276491847127422208	True	True	123.92	-63.99
33	5276446767151154048	True	True	124.86	-64.24
34	5320716335102626048	True	True	125.25	-52.23
35	5316349173696052736	True	False	126.03	-55.37
36	5223338912419663360	True	True	129.95	-69.91
37	5302977089383194368	True	True	130.45	-57.76
38	5221537843653900288	True	True	130.5	-71.22
39	5221537843653900544	True	True	130.5	-71.22
40	5302978704290910592	True	True	130.57	-57.72
41	5300961615845927936	True	True	131.08	-61.98
42	5297800829152578816	True	True	132.2	-63.13
43	5298428169260191104	True	True	134.53	-61.22
44	5298428169260191232	True	True	134.53	-61.22
45	5224035654899133440	True	False	135.03	-67.85
46	5323690033028759936	True	True	135.34	-52.35
47	5221973868734158976	True	True	136.1	-71.62

Continued on next page

ID	*Gaia* DR3 ID	member_our	member_kerr	ra (deg)	dec (deg)
48	5303566187102489344	True	True	137.16	-58.53
49	5216186726719969792	True	True	139.36	-74.73
50	5310606291358320512	True	True	139.51	-54.88
51	5299015441609388672	True	False	139.73	-61.02
52	5299141546145254528	True	True	140.9	-61.19
53	5217812354662194048	True	True	140.95	-73.68
54	5217812354662195328	True	True	140.95	-73.68
55	5250150091153808768	True	True	142.1	-64.25
56	5313934959706088320	True	True	142.57	-49.46
57	5217846817480160640	True	True	142.91	-73.75
58	5217868876431672960	True	True	142.98	-73.46
59	5217554622264363008	True	True	143.52	-74.09
60	5306966181987971456	True	False	143.6	-56.89
61	5250926999202194688	True	True	143.84	-62.37
62	5251098523021221376	True	True	144.84	-61.33
63	5244271552233795200	True	True	145.15	-67.75
64	5307852908070273792	True	True	145.56	-56.03
65	5405529741513021440	True	True	147.12	-52.03
66	5218453026345066368	True	True	147.25	-71.63
67	5257836605156299776	True	True	147.5	-58.47
68	5308164516542077440	True	True	148.45	-54.9
69	5258252942105518080	True	True	150.99	-59.4
70	5230321567172871040	True	True	151.34	-71.62
71	5230321361014440704	True	True	151.36	-71.62
72	5258513835596515328	True	True	151.41	-57.51
73	5356713413789909632	True	True	153.31	-52.52
74	5355142868813361792	True	True	153.49	-55.95
75	5230688284360121472	True	True	155.16	-71.09
76	5252895434280467072	True	True	155.19	-63.19
77	5253033285548628864	True	True	155.31	-62.43
78	5252222670597991040	True	True	157.59	-62.88
79	5229115299838780416	True	True	159.49	-73.49
80	5254474058096434432	True	True	159.68	-59.91
81	5239284339287940864	True	True	160.27	-65.69
82	5204523004293421696	True	True	160.39	-76.04
83	5240144982036017536	True	True	168.42	-64.82
84	5236935022238989568	True	False	169.07	-66.44
85	5217846851839896704	True	True	142.85	-73.75
86	5217846851839896832	True	True	142.85	-73.75
87	5486699125824396928	False	True	110.35	-57.34
88	5276844309323980800	False	True	126.02	-63.57
89	5300857711997333120	False	True	130.5	-62.31
90	5318296000780849536	False	True	131.47	-53.46
91	5216440061069982592	False	True	132.52	-75.91
92	5317505864239805696	False	True	132.98	-53.93
93	5317269950278675072	False	True	134.44	-54.14
94	5325281335588219008	False	True	134.47	-49.7
95	5305225281435405568	False	True	134.87	-54.78
96	5305106431102283648	False	True	135.01	-55.64
97	5310127660192135552	False	True	137.37	-55.64
98	5310142950274535424	False	True	138.32	-55.48
99	5312245422658960768	False	True	143.11	-52.63
100	5249913283844160256	False	True	145.79	-63.22
101	5343936233991963392	False	True	176.47	-55.35
102	5788750466217278592	False	True	185.87	-77.68
103	5410009942142844032	False	True	143.31	-48.81
104	5288017095509716480	False	True	118.53	-63.34
105	5221009695816673536	False	True	124.75	-72.67
106	5193473840145068800	False	True	130.59	-83.76
107	5286760525517037568	False	True	105.41	-62.6
108	5219983787046519168	False	True	124.93	-74.02
109	5297100607744079872	False	True	135.85	-63.81
110	5250988846733325312	False	True	142.99	-62.16
111	5796192888624311936	False	True	217.2	-74.51
112	5290482995153619712	True	True	123.69	-60.12
113	4625883599760005760	False	True	62.11	-78.75
114	5231963962676292224	False	True	164.26	-68.67
115	5219351911459314048	False	True	142.63	-70.7
116	5261761930366706816	False	True	95.92	-75.08
117	5491506843495850240	False	True	106.74	-53.9

Table A.1.: Columns 6-10

ID	e_ra (deg)	e_dec (deg)	plx (mas)	e_plx (mas)	e_plx_over
0	0.65	0.57	16.68	0.62	26.72
1	0.05	0.05	34.26	0.06	606.96
2	0.05	0.05	14.21	0.05	270.16
3	0.19	0.22	19.2	0.21	90.78
4	0.06	0.05	18.41	0.06	329.09
5	0.02	0.02	18.51	0.02	968.86
6	0.16	0.18	14.06	0.17	80.96
7	0.02	0.02	20.37	0.02	1221.86
8	0.01	0.01	17	0.01	1395.99
9	0.02	0.02	16.96	0.02	890.94
10	0.02	0.01	13.1	0.02	823.07
11	0.01	0.01	19.95	0.01	1605.7
12	0.01	0.01	13.45	0.01	1043.06
13	0.14	0.16	15.25	0.16	96.47
14	0.01	0.01	16.34	0.01	1294.05
15	0.01	0.01	18.05	0.01	1250.35
16	0.02	0.02	12.3	0.02	690.84
17	0.17	0.16	11.8	0.17	69.46
18	0.01	0.01	15.76	0.01	1179.41
19	0.04	0.04	11.97	0.04	336.59
20	0.02	0.01	11.49	0.01	814.05
21	0.03	0.02	11.25	0.02	478.86
22	0.02	0.01	16.19	0.02	1053.88
23	0.13	0.12	12.38	0.13	93.63
24	0.03	0.03	12.95	0.03	472.94
25	0.03	0.03	13.83	0.03	413.71
26	0.01	0.01	12.81	0.01	965.88
27	0.01	0.01	14.58	0.01	978.32
28	0.04	0.04	14.93	0.04	360.76
29	0.03	0.03	13.68	0.03	431.29
30	0.02	0.02	10.45	0.02	562.63
31	0.03	0.03	13.36	0.03	395.4
32	0.04	0.03	13.68	0.04	385.61
33	0.1	0.08	10.52	0.09	116.91
34	0.02	0.02	13.75	0.02	770.71
35	0.14	0.15	14.04	0.15	91.67
36	0.02	0.02	13.17	0.02	580.56
37	0.03	0.04	17.47	0.04	482.21
38	0.03	0.03	11.77	0.03	434.82
39	0.02	0.02	11.77	0.02	604.34
40	0.03	0.03	13.85	0.03	498.88
41	0.04	0.03	10.78	0.03	313.3
42	0.04	0.03	14.15	0.04	370.1
43	0.01	0.01	14.2	0.01	1017.27
44	0.01	0.01	14.22	0.01	1012.2
45	0.37	0.34	13.69	0.38	35.95
46	0.01	0.01	12.28	0.02	780.4
47	0.03	0.03	12.33	0.03	450.53
48	0.01	0.01	10.17	0.01	910.5
49	0.03	0.03	13.09	0.03	431.01
50	0.24	0.28	19.4	0.29	66.62
51	1.06	1.13	14.68	1.37	10.72
52	0.01	0.01	10.37	0.01	892.53
53	0.01	0.01	13.09	0.01	1202.34
54	0.02	0.02	13.08	0.02	547.4
55	0.01	0.02	11.28	0.02	667.24
56	0.01	0.01	11.21	0.02	691.88
57	0.02	0.03	12.8	0.03	472.67
58	0.01	0.01	12.79	0.01	959.13
59	0.02	0.02	12.85	0.02	751
60	0.42	0.54	11.41	0.57	19.93
61	0.02	0.02	12.02	0.02	591.49
62	0.08	0.07	14.48	0.08	185.86
63	0.05	0.05	13.1	0.05	266.46
64	0.02	0.02	12.42	0.02	686.09
65	0.07	0.07	11.17	0.08	139.16
66	0.06	0.06	12.75	0.06	201.23
67	0.01	0.02	12.88	0.02	824.86
68	0.05	0.05	11.77	0.06	204.11
69	0.02	0.02	10.2	0.02	586.53
70	0.03	0.03	11.58	0.04	327.64
71	0.06	0.05	11.67	0.06	205.09
72	0.01	0.01	17.49	0.02	1145.95
73	0.01	0.01	18.84	0.01	1692.45
74	0.05	0.05	15.58	0.06	272.17
75	0.02	0.02	11.41	0.03	440.41
76	0.25	0.25	14.36	0.27	53.06

Continued on next page

ID	e_ra (deg)	e_dec (deg)	plx (mas)	e_plx (mas)	e_plx_over
77	0.02	0.02	12.1	0.03	482.39
78	0.01	0.01	16.12	0.01	1229.46
79	0.01	0.01	13.51	0.02	879.84
80	0.02	0.02	10.99	0.02	539.37
81	0.17	0.17	12.79	0.19	65.94
82	0.02	0.02	12.87	0.02	653.55
83	0.01	0.01	14.69	0.01	1152.63
84	0.41	0.36	12.38	0.49	25.4
85	0.02	0.02	12.81	0.02	615.58
86	0.02	0.03	12.83	0.03	509.1
87	0.01	0.01	9.32	0.01	858.46
88	0.03	0.02	10.02	0.03	398.55
89	0.01	0.01	7.93	0.01	729.44
90	0.02	0.02	6.95	0.02	350.29
91	0.01	0.01	9.75	0.02	599.63
92	0.02	0.02	7.41	0.02	312.19
93	0.01	0.01	7.28	0.01	661.96
94	0.01	0.01	7.93	0.01	806.59
95	0.01	0.01	8.85	0.01	782.12
96	0.01	0.01	7.1	0.01	592.66
97	0.03	0.03	7.88	0.04	217.97
98	0.14	0.13	7.4	0.15	47.93
99	0.01	0.01	7.63	0.01	745.31
100	0.03	0.03	8.89	0.03	307.98
101	0.01	0.01	23.99	0.01	2003.71
102	0.01	0.01	13.11	0.02	790.23
103	0.01	0.01	21.61	0.01	1898.92
104	0.07	0.05	10.35	0.05	194.26
105	0.01	0.01	12.44	0.01	1020.52
106	0.04	0.04	11.81	0.05	255.74
107	0.01	0.01	11.36	0.01	863.55
108	0.09	0.08	15.41	0.09	173.19
109	0.01	0.01	12.82	0.01	1054.43
110	0.02	0.02	12.75	0.02	718.27
111	0.01	0.01	17.11	0.01	1144.1
112	0.03	0.03	26.03	0.03	858.35
113	0.01	0.01	17.33	0.02	1068.18
114	0.02	0.02	11.57	0.02	618.45
115	0.01	0.01	9.85	0.01	817.56
116	0.26	0.56	12.62	0.32	39.34
117	0.01	0.01	21.36	0.01	1934.87

Table A.1.: Columns 11-15

ID	pm (mas yr^{-1})	pmra (mas yr^{-1})	e_pmra (mas yr^{-1})	pmdec (mas yr^{-1})	e_pmdec (mas yr^{-1})
0	66.1	65.56	0.84	8.45	0.72
1	129.65	113.66	0.05	62.38	0.07
2	60.2	44.48	0.06	40.57	0.06
3	69.37	51.84	0.26	46.09	0.29
4	61.89	35.72	0.07	50.54	0.07
5	63.59	35.01	0.02	53.08	0.03
6	41.36	26.25	0.21	31.96	0.23
7	44.1	24.62	0.02	36.59	0.02
8	68.26	25.34	0.01	63.39	0.02
9	66.81	18.07	0.02	64.32	0.02
10	37.25	14.81	0.03	34.18	0.02
11	47.45	14.31	0.01	45.23	0.02
12	48.92	11.99	0.02	47.43	0.02
13	53.97	8.15	0.17	53.35	0.2
14	35.98	4.89	0.02	35.65	0.02
15	61	7.43	0.02	60.54	0.02
16	40.26	3.81	0.03	40.08	0.02
17	32.51	2	0.31	32.45	0.22
18	60.2	2.08	0.02	60.16	0.02
19	32.61	1.39	0.05	32.58	0.04
20	29.81	-1.54	0.02	29.77	0.02
21	33.37	-1.99	0.04	33.31	0.03
22	41.06	-11.79	0.02	39.33	0.02
23	39.72	-8.64	0.15	38.77	0.14
24	34.16	-8.82	0.03	33	0.03
25	26.39	-17.27	0.04	19.96	0.04
26	36.7	-17.25	0.02	32.39	0.02
27	52.05	-16.21	0.02	49.46	0.02
28	32.32	-21.34	0.05	24.28	0.05

Continued on next page

ID	pm (mas yr^{-1})	pmra (mas yr^{-1})	e_pmra (mas yr^{-1})	pmdec (mas yr^{-1})	e_pmdec (mas yr^{-1})
29	27.14	-19.58	0.04	18.79	0.04
30	32.14	-14.69	0.03	28.59	0.02
31	26.38	-18.34	0.04	18.95	0.04
32	38.78	-21.35	0.05	32.38	0.04
33	32.12	-14.99	0.14	28.41	0.11
34	29.65	-22.14	0.02	19.73	0.02
35	32.79	-23.05	0.17	23.32	0.18
36	44.51	-24.05	0.03	37.45	0.03
37	44.35	-33.98	0.05	28.5	0.04
38	39.88	-21.18	0.04	33.79	0.03
39	39.68	-20.8	0.03	33.79	0.02
40	35.15	-26.27	0.03	23.36	0.04
41	31.25	-19.73	0.06	24.24	0.04
42	42.24	-29.68	0.06	30.05	0.05
43	39.46	-30.55	0.02	24.98	0.02
44	39.4	-30.1	0.02	25.42	0.02
45	44.2	-30.65	0.49	31.84	0.44
46	30.68	-27.85	0.02	12.88	0.02
47	42.78	-25.98	0.04	34	0.03
48	29.94	-24.89	0.01	16.64	0.01
49	46.76	-29.78	0.04	36.05	0.04
50	57.73	-49.64	0.34	29.46	0.31
51	37.96	-31.79	1.33	20.75	1.13
52	32.3	-27.29	0.01	17.26	0.01
53	47.38	-31.04	0.01	35.79	0.01
54	47.38	-32.48	0.03	34.49	0.03
55	36.64	-30.55	0.02	20.23	0.02
56	33.05	-32.05	0.02	8.09	0.02
57	47.32	-32.24	0.03	34.63	0.03
58	46.34	-32.33	0.02	33.2	0.02
59	47.5	-33.41	0.02	33.77	0.02
60	37.08	-34.76	0.56	12.9	0.61
61	35.94	-31.3	0.03	17.66	0.02
62	47.07	-42.41	0.11	20.41	0.09
63	43.27	-36.07	0.06	23.89	0.06
64	35.77	-33.91	0.02	11.38	0.02
65	35.24	-34.51	0.09	7.11	0.08
66	45.61	-36.12	0.08	27.85	0.08
67	38.39	-36.19	0.02	12.82	0.02
68	34.02	-32.67	0.07	9.51	0.06
69	33.59	-31.52	0.02	11.62	0.02
70	41.37	-35.52	0.04	21.21	0.04
71	41.97	-35.57	0.07	22.27	0.06
72	58.67	-55.8	0.02	18.14	0.02
73	63.66	-62.94	0.01	9.56	0.01
74	52.03	-50.82	0.06	11.19	0.06
75	42.14	-36.98	0.03	20.19	0.03
76	45.89	-43.23	0.31	15.4	0.29
77	40.21	-38.47	0.03	11.71	0.03
78	53.6	-51.91	0.02	13.34	0.01
79	51.59	-46.32	0.02	22.7	0.02
80	37.53	-36.92	0.02	6.76	0.02
81	44.79	-43.28	0.26	11.55	0.23
82	50.35	-44.59	0.02	23.4	0.02
83	55.67	-55.43	0.01	5.22	0.01
84	50.13	-49.88	0.53	4.95	0.41
85	47.05	-34.55	0.03	31.93	0.02
86	46.7	-31.11	0.03	34.83	0.03
87	23.53	-1.71	0.01	23.46	0.01
88	34.16	-15.04	0.04	30.67	0.03
89	23.42	-13.01	0.01	19.48	0.01
90	16.34	-12.08	0.02	11	0.02
91	36.55	-16.7	0.02	32.51	0.01
92	19.09	-13.97	0.03	13.01	0.03
93	19.46	-14.67	0.01	12.8	0.01
94	20.71	-17.69	0.01	10.76	0.01
95	21.39	-17.44	0.01	12.39	0.01
96	19.66	-14.62	0.01	13.14	0.01
97	20.78	-16.68	0.04	12.39	0.04
98	15.58	-14.08	0.19	6.68	0.18
99	22.05	-19.89	0.01	9.52	0.01
100	41.69	-25.42	0.04	33.05	0.03
101	99.08	-98.94	0.01	-5.27	0.01
102	66.62	-65.8	0.02	10.45	0.02
103	54.7	-50.94	0.01	19.94	0.01
104	29.86	-11.09	0.1	27.73	0.07
105	58.19	-22.19	0.01	53.8	0.01
106	100.41	-48.39	0.05	87.98	0.05

Continued on next page

ID	pm (mas yr^{-1})	pmra (mas yr^{-1})	e_pmra (mas yr^{-1})	pmdec (mas yr^{-1})	e_pmdec (mas yr^{-1})
107	31.61	1.73	0.02	31.56	0.02
108	54.05	-23.53	0.11	48.66	0.1
109	39.96	-30.34	0.02	26	0.01
110	39.68	-34.58	0.02	19.47	0.02
111	74.38	-63.72	0.01	-38.36	0.01
112	68.01	-31.77	0.04	60.14	0.03
113	69.8	54.28	0.02	43.87	0.02
114	43.09	-41.13	0.02	12.86	0.02
115	34.56	-24.06	0.02	24.8	0.01
116	49.97	7.5	0.3	49.41	0.73
117	39.61	-7.41	0.01	38.91	0.01

Table A.1.: Columns 16-20

ID	ra_dec_cor	ra_plx_cor	ra_pmra_cor	ra_pmdec_cor	dec_plx_cor
0	0.08	0.15	-0.29	-0.33	-0.09
1	0.06	0.33	-0.12	-0.36	0.11
2	0.05	0.21	-0.03	-0.18	-0.22
3	0.03	0.13	2E-4	-0.11	0.2
4	-0.03	0.09	-0.02	-0.07	0.31
5	0.08	0.07	-0.13	-0.1	0.15
6	0.04	0.21	-0.04	-0.14	0.1
7	0.01	0.13	-0.28	-0.07	-0.03
8	0.05	-0.13	-0.33	-0.07	0.06
9	0.01	0.24	0.18	-0.17	0.1
10	-0.1	0.2	0.13	-0.11	0.02
11	-0.03	0.15	-0.08	-0.17	0.27
12	-0.07	0.11	-0.13	0.05	0.15
13	0.03	0.15	0.11	-0.12	0.06
14	0.28	0.16	0.07	-0.05	0.07
15	-0.06	-0.19	-0.01	-0.14	0.29
16	-0.02	-0.01	-0.09	0.12	0.18
17	0.05	0.07	3E-3	-0.09	0.18
18	0.06	0.06	0.06	0.12	0.35
19	0.05	0.13	-0.11	0.04	0.18
20	-0.06	-0.04	-0.17	0.13	0.15
21	0.08	0.16	0.06	-0.05	0.07
22	-0.09	0.18	0.13	-0.12	0.21
23	-0.08	-0.3	0.05	-0.05	0.17
24	0.01	0.21	-0.06	-0.02	0.08
25	0.06	0.03	-0.1	0.05	0.13
26	0.12	0.11	0.12	0.03	0.03
27	-0.01	-0.03	0.14	0.15	0.32
28	0.12	0.1	-0.1	0.05	0.25
29	0.05	0.1	-0.07	0.06	0.18
30	0.01	0.09	0.14	0.08	0.07
31	0.01	0.12	-0.07	0.12	0.1
32	0.08	-0.15	0.24	0.1	0.17
33	-0.04	0.05	0.25	-0.1	0.19
34	0.08	0.19	-0.12	-0.03	0.12
35	0.01	0.16	-0.11	0.1	0.02
36	0.03	0.06	0.02	0.07	0.23
37	-0.03	-0.06	3E-3	0.1	-4E-3
38	-0.01	-0.14	-0.09	0.11	0.09
39	0.04	-0.12	-0.08	0.1	0.13
40	-0.08	0.03	-0.07	0.11	0.09
41	0.03	0.02	0.18	0.03	0.18
42	0.08	0.05	0.17	0.18	0.12
43	0.16	-0.13	-0.24	-0.03	0.09
44	0.14	-0.14	-0.21	-0.01	0.04
45	-0.09	0.06	-0.02	0.13	0.25
46	0.09	-0.08	-0.07	0.11	0.18
47	0.12	0.06	0.07	0.04	0.25
48	0.11	0.11	0.13	0.1	0.23
49	-0.11	-0.04	0.04	0.17	0.19
50	0.08	0.08	-0.06	0.01	0.25
51	0.23	0.42	0.14	0.09	0.44
52	0.18	-0.04	-0.05	0.02	0.09
53	-0.05	0.07	-0.01	0.14	0.03
54	-0.05	0.06	0.04	0.15	0.05
55	0.01	-0.06	-0.05	0.1	0.37
56	0.04	-0.08	-0.14	0.15	0.1
57	0.06	-0.01	-0.1	0.12	0.34
58	-0.03	-0.05	0.01	0.24	0.23
59	0.05	0.05	0.15	0.26	-0.04

Continued on next page

ID	ra_dec_cor	ra_plx_cor	ra_pmra_cor	ra_pmdec_cor	dec_plx_cor
60	0.08	0.24	0.15	-0.14	0.22
61	0.23	-0.07	-0.13	0.08	0.11
62	0.21	0.28	0.27	0.2	0.15
63	0.14	0.02	-2E-3	0.1	0.14
64	0.15	-0.1	-0.18	0.11	0.03
65	0.17	0.03	-0.04	0.02	0.15
66	-0.08	0.03	-0.19	0.16	0.16
67	0.03	-0.02	-0.14	0.11	0.14
68	0.15	0.04	0.11	0.05	0.18
69	0.09	0.03	-0.02	0.2	0.21
70	-0.05	0.03	0.14	0.17	0.06
71	-0.07	0.05	0.11	0.19	0.06
72	-0.04	0.12	-0.07	0.26	0.12
73	0.13	-0.2	-0.28	-0.01	0.15
74	-2E-3	-0.19	-0.17	0.04	0.14
75	-2E-3	0.02	-0.07	0.07	0.17
76	-0.02	-0.07	-0.2	0.16	0.03
77	0.05	-0.18	-0.1	0.06	0.12
78	0.09	-0.07	0.12	0.26	0.1
79	-0.05	-0.02	-0.01	0.12	0.12
80	0.06	-0.01	-0.03	0.14	0.09
81	0.07	-0.05	-0.04	0.13	0.09
82	-0.02	-0.02	-0.28	0.16	0.31
83	0.12	-0.08	-0.26	0.04	0.19
84	0.04	-0.26	0.12	0.14	0.35
85	0.14	0.03	-0.32	0.05	0.38
86	0.4	0.13	-0.23	-0.17	0.32
87	0.11	0.15	0.06	0.1	0.28
88	0.12	-0.04	0.28	0.06	0.1
89	0.11	0.21	0.03	0.04	0.07
90	0.06	0.05	-0.17	0.02	0.2
91	0.13	0.35	0.42	-3E-3	0.25
92	0.05	0.08	0.01	0.01	0.29
93	0.01	-0.08	-0.14	0.15	0.19
94	0.05	-0.03	-0.06	0.14	0.14
95	0.04	0.13	0.04	0.17	0.13
96	0.1	-0.04	-0.04	0.07	0.22
97	0.03	-0.11	0.07	-0.03	0.14
98	0.01	0.02	0.02	-0.04	0.12
99	0.05	0.05	-0.04	0.07	0.11
100	-4E-4	-0.18	-0.08	0.19	0.19
101	0.31	-0.17	-0.16	0.17	E-3
102	0.14	0.05	-0.13	0.04	0.03
103	E-3	-0.18	-0.09	0.1	0.18
104	0.38	-0.13	-0.23	-0.27	0.05
105	-0.01	-0.08	0.24	0.03	0.31
106	-0.06	-0.02	-0.12	0.1	0.21
107	-0.09	0.22	0.2	-0.13	0.06
108	0.07	0.15	-0.01	0.01	0.19
109	0.08	0.11	-0.01	0.02	0.15
110	0.11	-0.01	0.12	0.16	0.23
111	0.21	-0.27	-0.42	-0.26	-0.12
112	0.02	0.01	-0.2	-0.04	0.33
113	0.06	0.03	-0.08	-0.23	0.05
114	-0.02	0.02	-0.03	0.17	0.2
115	0.01	0.09	0.28	0.1	0.25
116	-0.04	-0.03	-0.16	0.01	0.07
117	0.17	0.32	0.08	0.1	0.31

Table A.1.: Columns 21-25

ID	dec_pmra_cor	dec_pmdec_cor	plx_pmra_cor	plx_pmdec_cor	pmra_pmdec_cor
0	-0.28	0.13	-0.08	-0.33	0.15
1	-0.24	-0.13	-0.09	-0.58	0.1
2	-0.17	-0.13	-0.01	-0.15	0.16
3	-0.1	-0.12	-0.01	-0.14	0.03
4	0.01	-0.35	0.15	-0.27	-0.12
5	-0.09	-0.49	0.15	-0.15	0.11
6	-0.09	-0.32	0.18	-0.08	-0.07
7	-0.05	-0.41	0.03	-0.07	-2E-3
8	-0.07	-0.58	0.36	-0.06	0.07
9	-0.11	-0.09	0.19	-0.16	-0.12
10	-0.06	-0.16	0.09	-0.19	-0.21
11	-0.07	-0.24	0.16	-0.17	-0.14
12	0.07	-0.13	0.11	-0.04	-0.08
13	-0.05	-0.23	0.39	0.03	-0.03
14	-0.02	0.04	0.09	-0.04	0.1

Continued on next page

ID	dec_pmra_cor	dec_pmdec_cor	plx_pmra_cor	plx_pmdec_cor	pmra_pmdec_cor
15	0.01	-0.21	0.32	0.12	-0.02
16	0.14	-0.33	0.08	-0.16	-0.02
17	-0.06	-0.18	0.17	-0.12	0.02
18	0.16	-0.01	0.13	-0.1	0.08
19	0.05	-0.23	0.04	-0.03	0.05
20	0.15	-0.3	0.09	-0.05	-0.09
21	-0.03	-0.14	0.16	-0.01	0.01
22	-0.02	-0.12	0.28	-0.09	-0.25
23	0.03	-0.31	0.37	-0.06	-0.14
24	-0.01	-0.34	0.13	0.05	-0.03
25	0.05	-0.23	-0.08	0.12	-0.04
26	0.05	-0.2	0.09	0.04	0.08
27	0.23	-0.15	0.28	-0.03	-0.02
28	0.08	-0.21	0.12	0.07	0.02
29	0.1	-0.19	0.25	0.06	0.03
30	0.1	-0.13	0.16	-0.11	0.03
31	0.12	-0.21	0.12	0.25	-0.07
32	0.08	-0.17	0.18	-0.09	0.17
33	-0.08	-0.03	0.08	0.02	-0.08
34	0.01	-0.28	0.08	-0.09	-0.01
35	0.12	-0.24	0.03	-0.08	-0.02
36	0.15	-0.18	0.33	-0.11	-0.03
37	0.08	-0.3	0.11	-0.02	0.04
38	0.09	-0.11	0.08	-0.23	0.1
39	0.08	-0.1	0.05	-0.24	0.13
40	0.11	-0.23	0.13	0.05	-0.02
41	0.05	-0.09	0.09	-0.02	0.01
42	0.22	-0.03	0.24	-0.2	0.13
43	0.02	-0.2	0.24	0.18	0.14
44	0.03	-0.18	0.25	0.2	0.13
45	0.16	-0.23	0.27	0.01	-0.02
46	0.14	-0.13	0.19	-0.09	0.09
47	0.07	-0.29	0.06	0.02	0.07
48	0.19	-0.09	0.28	0.02	2E-3
49	0.22	-0.14	0.06	0.12	-0.23
50	0.06	-0.19	0.15	-0.09	0.03
51	0.13	-0.11	-0.25	-0.05	-0.06
52	0.08	-0.33	0.24	0.12	0.08
53	0.14	-0.15	0.18	0.01	-0.02
54	0.15	-0.16	0.16	-0.01	0.01
55	0.17	-0.03	0.19	0.05	-0.01
56	0.15	-0.18	0.18	-0.06	0.02
57	0.19	-0.15	0.22	-0.08	-0.08
58	0.3	-0.2	0.24	0.06	-0.05
59	0.24	-0.1	0.22	0.12	0.1
60	0.03	0.42	0.4	-0.18	-0.03
61	0.09	-0.16	0.28	-0.07	0.17
62	0.2	-0.08	0.15	0.13	0.23
63	0.15	-0.26	0.18	0.01	0.1
64	0.13	-0.26	0.12	0.04	0.05
65	0.03	-0.1	0.04	-0.14	0.14
66	0.2	-0.09	0.14	-0.05	0.02
67	0.13	-0.26	0.13	0.01	0.1
68	0.12	-0.12	0.25	0.13	0.09
69	0.25	-0.19	0.25	0.08	0.11
70	0.18	0.04	0.3	0.01	0.04
71	0.2	0.04	0.29	0.03	0.02
72	0.28	-0.22	0.31	0.11	0.02
73	0.02	-0.2	0.1	0.01	0.24
74	0.07	-0.09	0.14	0.02	0.16
75	0.1	-0.13	0.14	-0.04	0.03
76	0.18	-0.13	0.07	0.09	-0.01
77	0.06	-0.04	0.18	-0.09	-0.06
78	0.27	-0.04	0.07	-0.02	0.21
79	0.16	0.09	0.23	-0.01	0.06
80	0.17	-0.08	0.23	0.14	0.16
81	0.15	-0.14	0.21	-0.03	0.2
82	0.2	-0.09	0.16	0.09	-0.03
83	0.07	-0.04	0.07	0.09	0.15
84	0.25	0.1	0.23	2E-3	0.16
85	0.11	-0.21	0.2	-0.05	-0.02
86	-0.07	-0.36	0.19	-0.1	0.25
87	0.18	-0.14	0.29	-0.1	-0.05
88	0.05	-0.19	0.21	0.08	0.21
89	0.06	-0.22	0.22	0.04	0.11
90	0.05	-0.11	0.06	-0.13	0.16
91	0.18	-0.24	0.56	-0.07	-0.06
92	0.1	-0.15	0.28	-0.11	-0.04
93	0.19	-0.24	0.15	0.06	0.01
94	0.15	-0.23	0.09	-0.13	0.04

Continued on next page

ID	dec_pmra_cor	dec_pmdec_cor	plx_pmra_cor	plx_pmdec_cor	pmra_pmdec_cor
95	0.2	-0.23	0.19	-0.1	0.02
96	0.03	-0.12	-0.15	0.02	0.11
97	0.04	-0.12	0.24	0.15	-0.03
98	-0.06	-0.1	-0.08	-0.23	0.08
99	0.08	-0.26	0.21	0.1	0.11
100	0.22	-0.18	0.23	-0.09	-0.03
101	0.2	0.12	0.3	0.1	0.45
102	0.04	0.03	0.16	0.05	0.18
103	0.12	-0.2	0.1	-0.03	0.11
104	-0.27	-0.5	0.17	-0.01	0.41
105	0.04	0.12	0.02	0.06	-0.01
106	0.17	-0.24	0.33	-0.09	-0.11
107	-0.08	0.02	0.18	-0.21	-0.19
108	0.07	-0.17	0.22	-0.17	0.01
109	0.09	-0.34	0.21	0.05	-0.03
110	0.18	-0.1	0.17	-0.04	0.2
111	-0.25	-0.04	0.24	0.3	0.15
112	0.02	-0.29	0.15	-0.23	-0.04
113	-0.24	-0.21	0.31	-0.4	0.01
114	0.22	-0.03	0.23	-0.09	0.14
115	0.18	-0.03	0.33	-E-3	-0.02
116	-0.01	-0.73	0.27	0.13	0.07
117	0.15	-0.11	0.11	-0.04	0.1

Table A.1.: Columns 26-30

ID	RUWE	RV_Gaia (km s^{-1})	e_RV_Gaia (km s^{-1})	RV_UVES (km s^{-1})	e_RV_UVES (km s^{-1})
0	1.51				
1	1	14.16	0.13	14.5	0.28
2	1.1				
3	1.05				
4	1.26				
5	1.2			18.98	0.65
6	8.69	21.79	1.22		
7	1.36	21.73	1.59	23.2	0.25
8	0.94	17.03	0.9	19.51	2.22
9	1.29	3.13	4.77		
10	0.98	14.47	0.53		
11	0.92	22.02	0.19	23.04	0.43
12	1.24	15.5	1.76		
13	1.1				
14	1.24	21.04	5.26	23.04	0.17
15	1.02	20.45	0.22	21.17	0.34
16	1.18	13.71	3.67		
17	0.99				
18	1.12	17.08	0.38	17.55	0.38
19	1.15				
20	1.08	27.56	3.95	20.16	1.75
21	1.12				
22	1.15	22.05	2.03		
23	8.21	17.04	10.94		
24	2.59	17.73	2.61		
25	1.09				
26	1.24	20.44	5.41		
27	1.34	16.59	1.27		
28	1.11				
29	1.04				
30	1.11	22.58	3.42		
31	1.15				
32	1.24	12.11	5.68		
33	2.63				
34	0.84	22.32	0.74		
35	1.06				
36	1.07	16.85	10.98		
37	0.99				
38	1.07				
39	1.13				
40	1.02	-18.35	5.02		
41	1.06				
42	1.07				
43	1.15	23.43	3.09	20.93	0.13
44	1.07	20.77	2.82		
45	1.12				
46	1.03	28.7	3.3		
47	1.02				

Continued on next page

ID	RUWE	RV_Gaia (km s^{-1})	e_RV_Gaia (km s^{-1})	RV_UVES (km s^{-1})	e_RV_UVES (km s^{-1})
48	1.17	21.14	2.86	21.61	0.21
49	1.07	17.22	0.2	17.82	2.14
50	5.32				
51	1.1				
52	0.98	19.54	0.51	20.98	0.65
53	1.23	15.57	3.6	18.58	0.15
54	1.2	26.15	3.09		
55	1.27	23.51	3.52	17.95	0.39
56	1.07	9.72	3.65	21.57	0.81
57	1.97	8.76	4.06		
58	1.36	19.84	2.5	17.81	0.66
59	1.28	11.14	3.26	18.13	0.42
60	1.21				
61	1.21	12.62	4.88	18.77	1.64
62	0.79	23.45	0.78	28	2.96
63	1.11				
64	1.13	25.27	4.33		
65	1.01				
66	2.57	15.34	6.48	18.91	0.27
67	1.16	18.14	3.11	15.45	0.3
68	4.86	24.14	0.78		
69	1.28				
70	2.22	15.02	3.92	15.85	0.41
71	5.08	16.39	1.37		
72	1.11			15.16	0.72
73	0.9	17.59	0.32	18.34	0.36
74	1.11				
75	1.29	3.87	8.29		
76	7.04			17.46	0.27
77	2.11				
78	1.14	17.78	2.29	17.23	0.41
79	1.31	22.52	2.2	18.29	0.42
80	1.12	23.79	4.91		
81	1.63				
82	1.41	14.95	3.27		
83	1.06			11.81	0.49
84	1.02				
85	1.11				
86	1.59				
87	0.91	21.73	0.71		
88	1.94	19.48	0.91		
89	0.89	21.49	1.23		
90	1.59	23.11	1		
91	1.16	17.77	1.63		
92	1.78	19.15	8.07		
93	0.81	21.94	2.78		
94	0.77	21.91	1.35		
95	0.81	17.92	2.57		
96	0.84	23.11	2.43		
97	3	21.09	0.51		
98	11.08	21.14	1.84		
99	0.85				
100	1.89	19.93	2.64		
101	0.96	13.2	3.46		
102	0.92	13.58	0.19		
103	1	27.02	1.59		
104	1.24	17.18	4.52		
105	1.19	19.92	9.69		
106	3.47	-5.53	4.46		
107	1.41	18.16	3.04		
108	8.7	30.77	14.31		
109	1.15	25.99	9.38		
110	1.31	17.94	20.06		
111	1.04	9.26	1.34		
112	1.1	43.33	4.89		
113	1.02	12.69	2.24		
114	0.91	18.04	0.16		
115	0.94	19	0.76		
116	17.07	18.64	22.62		
117	0.99	21.48	0.85		

Table A.1.: Columns 31-35

ID	RV_our	RV_ Lit (km s^{-1})	e_RV_ Lit (km s^{-1})	r_RV_ Lit	RV_APOGEE (km s^{-1})
0	False				
1	True	14.6	0.2	13	
2	False				
3	False				
4	False				
5	True				
6	False	23.8	0.3	C11	23.93
7	True				
8	True	16	0.2	C11	
9	False				
10	False				
11	True				23.29
12	False	19.44	0.02	Simbad	18.74
13	False				
14	True				23.69
15	True				
16	False				
17	False				
18	True				
19	False				
20	True				23.53
21	False				
22	False	23.05	0.05	Simbad	21.72
23	False	22.47	0.14	Simbad	22.63
24	False	22.02	0.01	Simbad	21.84
25	False				
26	False	22	0.85	S	
27	False	17	1	13	
28	False				
29	False				
30	False				
31	False				
32	False				
33	False				
34	False				
35	False				
36	False				
37	False				
38	False	20.7	0.6	13	
39	False	20.7	0.6	13	
40	False				
41	False				
42	False				
43	True	20.6	0.6	13	
44	False	20.5	0.6	13	
45	False				
46	False				
47	False				
48	True				
49	True				
50	False	25.43	3.12	S	
51	False				
52	True	20.82	0.15	E	
53	True	18.9	0.6	13	
54	False	19.1	0.6	13	
55	True				
56	True				
57	False	19	0.6	13	
58	True				
59	True				
60	False				
61	True				
62	True				
63	False				
64	False				
65	False				
66	True	18.9	0.6	13	
67	True				
68	False	22.65	1.4	Simbad	
69	False				
70	True	19	0.6	13	
71	False	19.4	0.6	13	
72	True				
73	True				
74	False				
75	False				
76	True				
77	False				

Continued on next page

ID	RV_our	RV_ Lit (km s^{-1})	e_RV_ Lit (km s^{-1})	r_RV_ Lit	RV_APOGEE (km s^{-1})
78	True				
79	True				
80	False				
81	False				
82	False				
83	True				
84	False				
85	False				
86	False				
87	False	23.07	0.12	Simbad	
88	False	23.4	0.5	T6	
89	False	19.43	0.44	Simbad	
90	False	21.82	0.89	E	
91	False	15.73	0.04	Simbad	
92	False				
93	False	21.36	0.11	Simbad	
94	False	22.03	0.17	E	
95	False	9.38	0.01	Simbad	
96	False	23.1	0.4	Simbad	
97	False	22.11	0.86	E	
98	False	22.8	0.1	T6	
99	False	21.6	0.3	T6	
100	False	21.8	0.1	T6	
101	False	16.01	0.41	E	
102	False	12.5	0.27	E	
103	False	28.9	2.35	Simbad	
104	False				
105	False	25.84	0.54	S	
106	False	-8	2	L13	
107	False	22.57	0.72	S	22.52
108	False	26.24	1.54	S	
109	False	20.7	0.4	M14	
110	False	18.8	0.8	M14	
111	False	11.32	0.36	S	
112	False				
113	False	16.4	0.4	M14	
114	False				
115	False	19.4	0.4	Mo13	
116	False	18.93	0.88	S	19.42
117	False	22.57	0.9	S	

Table A.1.: Columns 36-40

ID	e_RV_APOGEE (km s^{-1})	RV_final (km s^{-1})	e_RV_final (km s^{-1})	r_RV_final	RUWE_cut
0					False
1		14.16	0.13	RV_Gaia	True
2					True
3					True
4					True
5		18.98	0.65	RV_UVES	True
6	0.06	23.93	0.06	RV_APOGEE	False
7		23.2	0.25	RV_UVES	True
8		17.03	0.9	RV_Gaia	True
9		3.13	4.77	RV_Gaia	True
10		14.47	0.53	RV_Gaia	True
11	0.03	23.29	0.03	RV_APOGEE	True
12	0.05	18.74	0.05	RV_APOGEE	True
13					True
14	0.08	23.69	0.08	RV_APOGEE	True
15		20.45	0.22	RV_Gaia	True
16		13.71	3.67	RV_Gaia	True
17					True
18		17.08	0.38	RV_Gaia	True
19					True
20	0.11	23.53	0.11	RV_APOGEE	True
21					True
22	0.12	21.72	0.12	RV_APOGEE	True
23	0.2	22.63	0.2	RV_APOGEE	False
24	0.03	21.84	0.03	RV_APOGEE	False
25					True
26		20.44	5.41	RV_Gaia	True
27		16.59	1.27	RV_Gaia	True
28					True
29					True

Continued on next page

ID	e_RV_APOGEE (km s^{-1})	RV_final (km s^{-1})	e_RV_final (km s^{-1})	r_RV_final	RUWE_cut
30		22.58	3.42	RV_Gaia	True
31					True
32		12.11	5.68	RV_Gaia	True
33					False
34		22.32	0.74	RV_Gaia	True
35					True
36		16.85	10.98	RV_Gaia	True
37					True
38					True
39					True
40		-18.35	5.02	RV_Gaia	True
41					True
42					True
43		20.93	0.13	RV_UVES	True
44		20.77	2.82	RV_Gaia	True
45					True
46		28.7	3.3	RV_Gaia	True
47					True
48		21.61	0.21	RV_UVES	True
49		17.22	0.2	RV_Gaia	True
50					False
51					True
52		19.54	0.51	RV_Gaia	True
53		18.58	0.15	RV_UVES	True
54		26.15	3.09	RV_Gaia	True
55		17.95	0.39	RV_UVES	True
56		21.57	0.81	RV_UVES	True
57		8.76	4.06	RV_Gaia	False
58		17.81	0.66	RV_UVES	True
59		18.13	0.42	RV_UVES	True
60					True
61		18.77	1.64	RV_UVES	True
62		23.45	0.78	RV_Gaia	True
63					True
64		25.27	4.33	RV_Gaia	True
65					True
66		18.91	0.27	RV_UVES	False
67		15.45	0.3	RV_UVES	True
68		24.14	0.78	RV_Gaia	False
69					True
70		15.85	0.41	RV_UVES	False
71		16.39	1.37	RV_Gaia	False
72		15.16	0.72	RV_UVES	True
73		17.59	0.32	RV_Gaia	True
74					True
75		3.87	8.29	RV_Gaia	True
76		17.46	0.27	RV_UVES	False
77					False
78		17.23	0.41	RV_UVES	True
79		18.29	0.42	RV_UVES	True
80		23.79	4.91	RV_Gaia	True
81					False
82		14.95	3.27	RV_Gaia	False
83		11.81	0.49	RV_UVES	True
84					True
85					True
86					False
87		21.73	0.71	RV_Gaia	True
88		19.48	0.91	RV_Gaia	False
89		21.49	1.23	RV_Gaia	True
90		23.11	1	RV_Gaia	False
91		17.77	1.63	RV_Gaia	True
92		19.15	8.07	RV_Gaia	False
93		21.94	2.78	RV_Gaia	True
94		21.91	1.35	RV_Gaia	True
95		17.92	2.57	RV_Gaia	True
96		23.11	2.43	RV_Gaia	True
97		21.09	0.51	RV_Gaia	False
98		21.14	1.84	RV_Gaia	False
99					True
100		19.93	2.64	RV_Gaia	False
101		13.2	3.46	RV_Gaia	True
102		13.58	0.19	RV_Gaia	True
103		27.02	1.59	RV_Gaia	True
104		17.18	4.52	RV_Gaia	True
105		19.92	9.69	RV_Gaia	True
106		-5.53	4.46	RV_Gaia	False
107	0.04	22.52	0.04	RV_APOGEE	False

Continued on next page

ID	e_RV_APOGEE (km s^{-1})	RV_final (km s^{-1})	e_RV_final (km s^{-1})	r_RV_final	RUWE_cut
108		30.77	14.31	RV_Gaia	False
109		25.99	9.38	RV_Gaia	True
110		17.94	20.06	RV_Gaia	True
111		9.26	1.34	RV_Gaia	True
112		43.33	4.89	RV_Gaia	True
113		12.69	2.24	RV_Gaia	True
114		18.04	0.16	RV_Gaia	True
115		19	0.76	RV_Gaia	True
116	0.07	19.42	0.07	RV_APOGEE	False
117		21.48	0.85	RV_Gaia	True

Table A.1.: Columns 41-45

ID	spec_binary	RV_qual	qual_rvfinal	qual_uves	X (pc)
0	False	False	False	False	20.423
1	False	True	True	True	9.351
2	False	False	False	False	28.09
3	False	False	False	False	15.157
4	False	False	False	False	9.587
5	False	True	True	True	9.051
6	False	True	False	False	-1.154
7	False	True	True	True	-6.831
8	False	True	True	False	20.973
9	False	False	False	False	20.678
10	True	True	True	False	0.774
11	False	True	False	True	-2.383
12	False	True	True	False	18.51
13	False	False	False	False	11.697
14	False	True	True	True	-4.236
15	False	True	True	True	10.966
16	False	False	False	False	14.342
17	False	False	False	False	4.819
18	False	True	True	True	20.792
19	False	False	False	False	3.274
20	False	True	True	False	2.291
21	False	False	False	False	9.941
22	False	True	True	False	0.7
23	False	True	False	False	11.617
24	False	True	False	False	8.997
25	False	False	False	False	-6.455
26	False	False	False	False	8.453
27	False	False	False	False	19.114
28	False	False	False	False	-1.365
29	False	False	False	False	-5.815
30	False	False	False	False	16.203
31	False	False	False	False	-6.022
32	False	False	False	False	9.54
33	False	False	False	False	13.105
34	False	True	True	False	-2.548
35	False	False	False	False	1.068
36	False	False	False	False	17.948
37	False	False	False	False	4.216
38	False	False	False	False	21.728
39	False	False	False	False	21.729
40	False	False	False	False	5.324
41	False	False	False	False	12.498
42	False	False	False	False	11.006
43	False	True	True	True	10.061
44	False	False	False	False	10.051
45	False	False	False	False	16.801
46	False	False	False	False	2.598
47	False	False	False	False	22.768
48	False	True	True	True	12.153
49	False	True	True	False	25.054
50	False	False	False	False	4.816
51	False	False	False	False	11.585
52	False	True	True	True	17.263
53	False	True	True	True	24.579
54	False	False	False	False	24.601
55	True	True	True	True	19.639
56	False	True	False	False	4.552
57	False	False	False	False	25.722
58	False	True	True	True	25.528
59	False	True	True	True	26.07
60	False	False	False	False	12.814

Continued on next page

ID	spec_binary	RV_qual	qual_rvfinal	qual_uves	X (pc)
61	False	False	False	False	17.487
62	False	True	True	False	14.137
63	False	False	False	False	21.057
64	False	False	False	False	12.114
65	False	False	False	False	10.577
66	False	True	False	False	25.471
67	False	True	True	True	14.851
68	False	True	False	False	13.589
69	False	False	False	False	22.078
70	False	True	False	False	29.545
71	False	False	False	False	29.334
72	False	True	True	True	11.976
73	False	True	True	True	9.291
74	False	False	False	False	13.484
75	False	False	False	False	31.098
76	False	True	False	False	20.116
77	False	False	False	False	23.398
78	False	True	True	True	18.734
79	False	True	True	True	28.988
80	False	False	False	False	26.618
81	False	False	False	False	26.645
82	False	False	False	False	31.954
83	False	True	True	True	26.279
84	False	False	False	False	32.229
85	False	False	False	False	25.69
86	False	False	False	False	25.649
87	False	True	True	False	-2.601
88	False	True	False	False	13.296
89	False	False	False	False	17.185
90	False	False	False	False	2.975
91	False	False	False	False	32.981
92	False	False	False	False	4.987
93	False	False	False	False	6.777
94	False	False	False	False	-1.176
95	True	False	False	False	6.845
96	False	False	False	False	10.262
97	False	True	False	False	11.211
98	False	False	False	False	12.534
99	False	False	False	False	12.167
100	False	False	False	False	26.003
101	False	False	False	False	16.61
102	False	True	True	False	38.4
103	False	False	False	False	2.285
104	False	False	False	False	9.643
105	True	False	False	False	20.68
106	False	False	False	False	34.954
107	False	True	False	False	4.296
108	False	False	False	False	17.953
109	False	False	False	False	14.279
110	False	False	False	False	15.897
111	False	False	False	False	36.179
112	False	False	False	False	2.792
113	False	False	False	False	18.397
114	False	True	True	False	33.176
115	False	True	True	False	30.018
116	False	True	False	False	19.432
117	False	True	True	False	-4.337

Table A.1.: Columns 46-50

ID	e_X (pc)	Y (pc)	e_Y (pc)	Z (pc)	e_Z (pc)
0	0.764	-41.624	1.558	-37.98	1.421
1	0.015	-21.348	0.035	-17.567	0.029
2	0.104	-53.569	0.198	-35.994	0.133
3	0.167	-40.413	0.445	-29.156	0.321
4	0.029	-44.746	0.136	-29.247	0.089
5	0.009	-44.56	0.046	-29.165	0.03
6	0.014	-59.773	0.738	-38.513	0.476
7	0.006	-41.94	0.034	-24.567	0.02
8	0.015	-47.054	0.034	-28.392	0.02
9	0.023	-47.586	0.053	-28.02	0.031
10	0.001	-67.148	0.081	-36.295	0.044
11	0.001	-44.637	0.028	-22.708	0.014
12	0.018	-63.113	0.061	-34.613	0.033
13	0.121	-57.55	0.597	-29.178	0.303

Continued on next page

ID	e_X (pc)	Y (pc)	e_Y (pc)	Z (pc)	e_Z (pc)
14	0.003	-55.883	0.043	-24.544	0.019
15	0.009	-48.436	0.039	-24.527	0.02
16	0.021	-71.72	0.104	-35.501	0.051
17	0.069	-77.722	1.119	-33.472	0.482
18	0.018	-52.956	0.045	-28.059	0.024
19	0.01	-76.97	0.229	-32.239	0.096
20	0.003	-80.999	0.099	-31.845	0.039
21	0.021	-81.699	0.171	-33.669	0.07
22	0.001	-58.346	0.055	-20.206	0.019
23	0.124	-74.673	0.797	-28.518	0.305
24	0.019	-72.385	0.153	-25.261	0.053
25	0.016	-70.759	0.171	-13.495	0.033
26	0.009	-74.397	0.077	-22.053	0.023
27	0.02	-60.948	0.062	-24.999	0.026
28	0.004	-65.639	0.182	-13.288	0.037
29	0.013	-71.96	0.167	-11.597	0.027
30	0.029	-89.827	0.16	-28.778	0.051
31	0.015	-73.698	0.186	-11.47	0.029
32	0.025	-69.761	0.181	-19.711	0.051
33	0.112	-90.665	0.775	-25.256	0.216
34	0.003	-71.819	0.093	-11.109	0.014
35	0.012	-70.127	0.765	-12.556	0.137
36	0.031	-70.419	0.121	-21.938	0.038
37	0.009	-56.304	0.117	-9.492	0.02
38	0.05	-78.112	0.18	-25.386	0.058
39	0.036	-78.105	0.129	-25.383	0.042
40	0.011	-71.017	0.143	-11.876	0.024
41	0.04	-89.912	0.287	-18.993	0.061
42	0.03	-68.195	0.184	-14.807	0.04
43	0.01	-68.61	0.068	-12.305	0.012
44	0.01	-68.523	0.067	-12.289	0.012
45	0.467	-68.81	1.914	-17.798	0.495
46	0.003	-81.166	0.104	-5.63	0.007
47	0.051	-74.508	0.166	-22.629	0.05
48	0.013	-96.756	0.107	-12.498	0.014
49	0.058	-68.421	0.159	-22.956	0.053
50	0.072	-51.214	0.769	-3.471	0.052
51	1.081	-66.453	6.201	-9.549	0.891
52	0.019	-93.973	0.105	-13.049	0.015
53	0.02	-69.028	0.057	-21.651	0.018
54	0.045	-69.09	0.126	-21.667	0.04
55	0.029	-85.208	0.128	-14.73	0.022
56	0.007	-89.104	0.129	2.06	0.003
57	0.054	-70.484	0.149	-21.676	0.046
58	0.027	-70.716	0.074	-21.408	0.022
59	0.035	-70.005	0.093	-21.754	0.029
60	0.643	-86.515	4.34	-5.664	0.284
61	0.03	-80.6	0.136	-11.092	0.019
62	0.076	-67.139	0.361	-7.906	0.043
63	0.079	-71.819	0.27	-14.905	0.056
64	0.018	-79.517	0.116	-3.292	0.005
65	0.076	-88.911	0.639	2.03	0.015
66	0.127	-71.796	0.357	-18.549	0.092
67	0.018	-76.077	0.092	-4.788	0.006
68	0.067	-83.878	0.411	-0.636	0.003
69	0.038	-95.324	0.163	-5.401	0.009
70	0.09	-78.809	0.241	-19.212	0.059
71	0.143	-78.214	0.381	-19.075	0.093
72	0.01	-55.883	0.049	-1.504	0.001
73	0.005	-52.181	0.031	2.962	0.002
74	0.05	-62.739	0.231	0.476	0.002
75	0.071	-79.955	0.181	-17.802	0.04
76	0.379	-66.359	1.251	-6.213	0.117
77	0.049	-78.986	0.164	-6.418	0.013
78	0.015	-58.962	0.048	-4.628	0.004
79	0.033	-66.035	0.075	-16.734	0.019
80	0.049	-87.027	0.162	-1.92	0.004
81	0.404	-73.025	1.108	-8.349	0.127
82	0.049	-67.842	0.104	-20.308	0.031
83	0.023	-62.611	0.054	-4.619	0.004
84	1.269	-73.719	2.903	-7.469	0.294
85	0.042	-70.45	0.114	-21.674	0.035
86	0.05	-70.334	0.138	-21.639	0.042
87	0.003	-101.537	0.119	-34.463	0.04
88	0.033	-95.69	0.24	-25.207	0.063
89	0.024	-121.99	0.168	-26.706	0.037
90	0.008	-142.949	0.407	-16.203	0.046
91	0.055	-90.823	0.152	-34.36	0.057

Continued on next page

ID	e_X (pc)	Y (pc)	e_Y (pc)	Z (pc)	e_Z (pc)
92	0.016	-134.116	0.429	-14.253	0.046
93	0.01	-136.498	0.206	-13.258	0.02
94	0.001	-125.897	0.156	-5.803	0.007
95	0.009	-112.184	0.143	-11.347	0.014
96	0.017	-139.697	0.236	-15.372	0.026
97	0.051	-125.848	0.578	-11.652	0.054
98	0.262	-134.031	2.797	-11.232	0.234
99	0.016	-130.408	0.174	-1.747	0.002
100	0.085	-108.44	0.353	-15.072	0.049
101	0.008	-37.949	0.019	4.601	0.002
102	0.049	-62.928	0.08	-19.605	0.025
103	0.001	-46.189	0.024	1.718	0.001
104	0.05	-91.683	0.472	-28.952	0.149
105	0.02	-72.794	0.071	-27.034	0.027
106	0.137	-68.961	0.27	-34.575	0.135
107	0.005	-81.08	0.094	-34.036	0.04
108	0.104	-58.161	0.336	-22.471	0.13
109	0.014	-75.172	0.072	-15.235	0.015
110	0.022	-76.045	0.106	-10.606	0.015
111	0.032	-44.019	0.039	-13.022	0.011
112	0.003	-37.212	0.043	-9.134	0.011
113	0.017	-44.095	0.041	-32.344	0.03
114	0.054	-78.913	0.128	-12.146	0.02
115	0.037	-93.771	0.115	-24.572	0.03
116	0.494	-67.268	1.71	-37.111	0.943
117	0.002	-43.931	0.023	-15.586	0.008

Table A.1.: Columns 51-55

ID	U_final (km s^{-1})	e_U_final (km s^{-1})	V_final (km s^{-1})	e_V_final (km s^{-1})	W_final (km s^{-1})
0					
1	-10.59	0.05	-19.5	0.1	-5.47
2					
3					
4					
5	-10.91	0.11	-21.93	0.54	-5.03
6	-11.53	0.16	-24.5	0.08	-5.82
7	-11.51	0.04	-21.83	0.22	-5.89
8	-10.22	0.32	-22.89	0.72	-4.9
9	-15.22	1.67	-11.2	3.85	1.21
10	-11.65	0.02	-15.94	0.47	-1.2
11	-11.32	0.01	-22.46	0.03	-6.09
12	-10.66	0.02	-22.66	0.05	-4.62
13					
14	-11.42	0.01	-22.45	0.08	-5.97
15	-10.71	0.05	-23.01	0.19	-5.53
16	-12.03	0.65	-16.65	3.24	-2.63
17					
18	-10.54	0.13	-22.01	0.32	-4.9
19					
20	-11.25	0.02	-23.36	0.1	-5.72
21					
22	-11.73	0.01	-20.97	0.11	-6.2
23	-11.49	0.18	-24.02	0.19	-5.89
24	-9.65	0.03	-22.61	0.03	-5.39
25					
26	-11.28	0.59	-21.02	5.16	-5.75
27	-11.18	0.35	-20.49	1.13	-4.11
28					
29					
30	-10.5	0.58	-23.89	3.21	-6.43
31					
32	-11.75	0.74	-13.19	5.42	-3.94
33					
34	-10.65	0.03	-21.3	0.73	-5.97
35					
36	-11.5	2.6	-19.7	10.19	-4.49
37					
38					
39					
40	-13.14	0.37	17.56	4.94	0.68
41					
42					
43	-9.87	0.02	-21.83	0.12	-6.14
44	-9.89	0.4	-21.71	2.75	-5.9

Continued on next page

ID	U_final (km s^{-1})	e_U_final (km s^{-1})	V_final (km s^{-1})	e_V_final (km s^{-1})	W_final (km s^{-1})
45					
46	-9.9	0.11	-28.63	3.29	-6.79
47					
48	-10.81	0.03	-22.53	0.21	-6.11
49	-10.19	0.08	-21.4	0.18	-4.65
50					
51					
52	-10.75	0.09	-21.21	0.5	-5.86
53	-10.12	0.05	-22.71	0.14	-4.65
54	-7.77	0.99	-29.37	2.79	-7.47
55	-10.87	0.09	-20.18	0.37	-5.84
56	-11.1	0.05	-22.32	0.8	-6.29
57	-13.51	1.34	-14.06	3.66	-1.88
58	-10.31	0.22	-22	0.6	-4.67
59	-10.33	0.14	-22.48	0.38	-4.89
60					
61	-9.63	0.35	-20.68	1.59	-5.72
62	-9.79	0.18	-25.37	0.76	-6.92
63					
64	-8.71	0.65	-26.65	4.28	-6.22
65					
66	-9.88	0.12	-22.76	0.25	-5.41
67	-10.15	0.06	-17.39	0.3	-5.75
68	-8.66	0.14	-25.82	0.77	-5.38
69					
70	-10.48	0.15	-19.98	0.37	-5.36
71	-10.41	0.48	-20.6	1.25	-5.15
72	-11.63	0.15	-17.86	0.71	-5.34
73	-11.03	0.06	-20.2	0.31	-6.02
74					
75	-14.99	2.94	-9.55	7.57	-2.32
76	-9.14	0.3	-20.61	0.27	-5.08
77					
78	-9.3	0.12	-20.63	0.39	-5.78
79	-9.49	0.17	-23.31	0.38	-5.38
80	-7.74	1.44	-27.12	4.69	-5.71
81					
82	-10.69	1.35	-20.8	2.86	-4.53
83	-11.47	0.19	-17.22	0.45	-5.82
84					
85					
86					
87	-11.98	0.02	-21.41	0.67	-3.65
88	-13.27	0.13	-21.31	0.87	-3.25
89	-10.9	0.17	-22.87	1.19	-3.96
90	-10.52	0.04	-22.98	0.99	-4.43
91	-10.57	0.53	-22.49	1.44	-3.72
92	-11.39	0.3	-19.31	8.02	-3.66
93	-11.44	0.14	-22.25	2.76	-3.98
94	-11.97	0.02	-21.6	1.35	-4.84
95	-10.03	0.16	-18.2	2.55	-4.55
96	-11.32	0.18	-23.68	2.41	-4.19
97	-10.38	0.08	-21.79	0.51	-4.27
98	-7.32	0.29	-21.54	1.83	-5.37
99					
100	-16.46	0.61	-24.86	2.54	1.66
101	-11.56	1.38	-20.1	3.15	-4.46
102	-13.56	0.1	-23.98	0.16	-2.44
103	-9.83	0.08	-27.68	1.59	-3.35
104	-11.82	0.46	-18.03	4.29	-4.17
105	-15.84	2.49	-24.85	8.78	-4.41
106	-38.03	1.85	-14.11	3.63	3.25
107	-11.3	0.02	-23.02	0.04	-4.84
108	-7.28	3.96	-32.73	12.83	-9.94
109	-9.67	1.72	-27.32	9.04	-7.33
110	-10.47	4.07	-19.86	19.46	-5.96
111	-10.45	0.83	-19.35	1.01	-5.19
112	-9.17	0.36	-43.06	4.74	-9.62
113	-11.82	0.71	-19.43	1.71	-2.87
114	-9.33	0.07	-22.92	0.15	-5
115	-10.19	0.23	-22.69	0.7	-4.31
116	-12.62	0.49	-23.01	0.18	-6.35
117	-10.68	0.08	-19.75	0.8	-5.87

Table A.1.: Columns 56-60

ID	e_W_final (km s^{-1})	maha_rvfinal	maha_flag_rvfinal	bonafide_rvfinal	U_uves (km s^{-1})
0			False	False	
1	0.08	1.41	True	False	-10.48
2			False	False	
3			False	False	
4			False	False	
5	0.35	1.31	True	True	-10.91
6	0.1		False	False	
7	0.13	2.8	True	True	-11.51
8	0.43	1.31	True	True	-9.34
9	2.27		False	False	
10	0.25	112.85	False	False	
11	0.02		False	False	-11.31
12	0.03	2.83	True	True	
13			False	False	
14	0.03	3.49	True	True	-11.38
15	0.1	1.35	True	False	-10.57
16	1.6		False	False	
17			False	False	
18	0.17	1.07	True	True	-10.39
19			False	False	
20	0.04	3.79	True	True	-11.34
21			False	False	
22	0.04	3.97	True	False	
23	0.09		False	False	
24	0.02		False	False	
25			False	False	
26	1.53		False	False	
27	0.46		False	False	
28			False	False	
29			False	False	
30	1.03		False	False	
31			False	False	
32	1.53		False	False	
33			False	False	
34	0.11	1.08	True	False	
35			False	False	
36	3.17		False	False	
37			False	False	
38			False	False	
39			False	False	
40	0.83		False	False	
41			False	False	
42			False	False	
43	0.02	4.86	True	False	-9.87
44	0.49		False	False	
45			False	False	
46	0.23		False	False	
47			False	False	
48	0.03	2.91	True	True	-10.81
49	0.06	2.31	True	False	-9.99
50			False	False	
51			False	False	
52	0.07	0.63	True	False	-10.49
53	0.04	2.14	True	True	-10.12
54	0.88		False	False	
55	0.06	0.75	True	False	-10.87
56	0.02		False	False	-11.1
57	1.13		False	False	
58	0.18	1.93	True	True	-10.31
59	0.12	1.09	True	True	-10.33
60			False	False	
61	0.22		False	False	-9.63
62	0.1	22.93	False	False	-8.86
63			False	False	
64	0.18		False	False	
65			False	False	
66	0.07		False	False	-9.88
67	0.02	7.71	False	False	-10.15
68	0.04		False	False	
69			False	False	
70	0.09		False	False	-10.48
71	0.31		False	False	
72	0.02	7.17	False	False	-11.63
73	0.02	1.26	True	False	-10.9
74			False	False	
75	1.68		False	False	
76	0.13		False	False	-9.14
77			False	False	

Continued on next page

ID	e_W_final (km s^{-1})	maha_rvfinal	maha_flag_rvfinal	bonafide_rvfinal	U_uves (km s^{-1})
78	0.03	6.88	False	False	-9.3
79	0.1	4.04	True	False	-9.49
80	0.1		False	False	
81			False	False	
82	0.85		False	False	
83	0.03	6.53	False	False	-11.47
84			False	False	
85			False	False	
86			False	False	
87	0.23	24.3	False	False	
88	0.23		False	False	
89	0.26		False	False	
90	0.11		False	False	
91	0.55		False	False	
92	0.85		False	False	
93	0.27		False	False	
94	0.06		False	False	
95	0.26		False	False	
96	0.27		False	False	
97	0.06		False	False	
98	0.2		False	False	
99			False	False	
100	0.35		False	False	
101	0.38		False	False	
102	0.05	83.04	False	False	
103	0.06		False	False	
104	1.36		False	False	
105	3.26		False	False	
106	1.82		False	False	
107	0.02		False	False	
108	4.96		False	False	
109	1.83		False	False	
110	2.71		False	False	
111	0.3		False	False	
112	1.16		False	False	
113	1.26		False	False	
114	0.02	3.96	True	False	
115	0.18	4.17	True	True	
116	0.11		False	False	
117	0.28	1.24	True	False	

Table A.1.: Columns 61-65

ID	e_U_uves (km s^{-1})	V_uves (km s^{-1})	e_V_uves (km s^{-1})	W_uves (km s^{-1})	e_W_uves (km s^{-1})
0					
1	0.09	-19.75	0.2	-5.67	0.17
2					
3					
4					
5	0.11	-21.93	0.54	-5.03	0.35
6					
7	0.04	-21.83	0.22	-5.89	0.13
8	0.79	-24.87	1.77	-6.09	1.07
9					
10					
11	0.02	-22.23	0.39	-5.98	0.2
12					
13					
14	0.02	-21.86	0.15	-5.7	0.07
15	0.07	-23.64	0.29	-5.85	0.15
16					
17					
18	0.13	-22.4	0.32	-5.1	0.17
19					
20	0.05	-20.23	1.63	-4.49	0.64
21					
22					
23					
24					
25					
26					
27					
28					
29					
30					

Continued on next page

ID	e_U_uves (km s^{-1})	V_uves (km s^{-1})	e_V_uves (km s^{-1})	W_uves (km s^{-1})	e_W_uves (km s^{-1})
31					
32					
33					
34					
35					
36					
37					
38					
39					
40					
41					
42					
43	0.02	-21.83	0.12	-6.14	0.02
44					
45					
46					
47					
48	0.03	-22.53	0.21	-6.11	0.03
49	0.7	-21.93	1.92	-4.83	0.64
50					
51					
52	0.12	-22.61	0.63	-6.06	0.09
53	0.05	-22.71	0.14	-4.65	0.04
54					
55	0.09	-20.18	0.37	-5.84	0.06
56	0.05	-22.32	0.8	-6.29	0.02
57					
58	0.22	-22	0.6	-4.67	0.18
59	0.14	-22.48	0.38	-4.89	0.12
60					
61	0.35	-20.68	1.59	-5.72	0.22
62	0.61	-29.79	2.88	-7.44	0.34
63					
64					
65					
66	0.12	-22.76	0.25	-5.41	0.07
67	0.06	-17.39	0.3	-5.75	0.02
68					
69					
70	0.15	-19.98	0.37	-5.36	0.09
71					
72	0.15	-17.86	0.71	-5.34	0.02
73	0.06	-20.94	0.35	-5.97	0.02
74					
75					
76	0.3	-20.61	0.27	-5.08	0.13
77					
78	0.12	-20.63	0.39	-5.78	0.03
79	0.17	-23.31	0.38	-5.38	0.1
80					
81					
82					
83	0.19	-17.22	0.45	-5.82	0.03
84					
85					
86					
87					
88					
89					
90					
91					
92					
93					
94					
95					
96					
97					
98					
99					
100					
101					
102					
103					
104					
105					
106					
107					
108					

Continued on next page

ID	e_U_uves (km s^{-1})	V_uves (km s^{-1})	e_V_uves (km s^{-1})	W_uves (km s^{-1})	e_W_uves (km s^{-1})
109					
110					
111					
112					
113					
114					
115					
116					
117					

Table A.1.: Columns 66-70

ID	maha_uves	maha_flag_uves	bonafide_uves	Gmag (mag)	e_Gmag (mag)
0		False	False	20.016	0.009
1	2.76	True	False	5.406	0.003
2		False	False	16.508	0.003
3		False	False	19.123	0.004
4		False	False	16.325	0.003
5	2.07	True	True	14.327	0.003
6		False	False	8.267	0.003
7	3.28	True	True	12.884	0.004
8		False	False	8.915	0.003
9		False	False	14.292	0.003
10		False	False	7.37	0.003
11	2.81	True	True	8.838	0.003
12		False	False	12.449	0.003
13		False	False	18.533	0.004
14	2.41	True	True	13.459	0.003
15	2.29	True	False	8.995	0.004
16		False	False	14.572	0.003
17		False	False	18.795	0.004
18	1.06	True	True	9.777	0.003
19		False	False	15.922	0.003
20		False	False	14.373	0.003
21		False	False	15.307	0.003
22		False	False	13.859	0.003
23		False	False	14.21	0.003
24		False	False	12.508	0.003
25		False	False	15.777	0.003
26		False	False	12.583	0.003
27		False	False	12.572	0.003
28		False	False	16.193	0.003
29		False	False	15.788	0.003
30		False	False	14.799	0.003
31		False	False	15.72	0.003
32		False	False	15.337	0.003
33		False	False	16.251	0.004
34		False	False	6.618	0.003
35		False	False	18.687	0.004
36		False	False	15.295	0.003
37		False	False	16.061	0.003
38		False	False	15.62	0.003
39		False	False	14.664	0.003
40		False	False	15.646	0.003
41		False	False	15.924	0.003
42		False	False	15.75	0.003
43	5.79	False	False	13.963	0.003
44		False	False	13.987	0.003
45		False	False	19.84	0.005
46		False	False	14.383	0.003
47		False	False	15.63	0.003
48	1.93	True	True	13.184	0.004
49		False	False	5.862	0.003
50		False	False	13.15	0.003
51		False	False	20.708	0.012
52	1.8	True	True	9.747	0.003
53	3.81	True	True	13.385	0.003
54		False	False	15.087	0.003
55	0.98	True	False	13.972	0.003
56		False	False	14.415	0.003
57		False	False	13.905	0.003
58	3.38	True	True	13.444	0.003
59	2.08	True	True	14.287	0.003
60		False	False	19.723	0.013
61		False	False	14.446	0.003

Continued on next page

ID	maha_uves	maha_flag_uves	bonafide_uves	Gmag	e_Gmag
				(mag)	(mag)
62		False	False	4.482	0.003
63		False	False	16.456	0.003
64		False	False	14.389	0.003
65		False	False	17.132	0.003
66		False	False	13.897	0.005
67	15.01	False	False	14.235	0.003
68		False	False	10.584	0.003
69		False	False	14.229	0.003
70		False	False	14.6	0.003
71		False	False	12.446	0.003
72	5.67	False	False	13.811	0.003
73	0.79	True	False	9.477	0.003
74		False	False	15.475	0.003
75		False	False	14.821	0.003
76		False	False	13.525	0.006
77		False	False	13.594	0.003
78	13.24	False	False	13.555	0.003
79	4.55	True	False	13.884	0.003
80		False	False	14.737	0.003
81		False	False	17.854	0.004
82		False	False	14.123	0.003
83	6.57	False	False	12.278	0.004
84		False	False	19.95	0.005
85		False	False	7.413	0.003
86		False	False	9.193	0.003
87		False	False	10.399	0.003
88		False	False	9.704	0.003
89		False	False	10.696	0.003
90		False	False	10.228	0.003
91		False	False	10.376	0.003
92		False	False	10.552	0.003
93		False	False	11.487	0.003
94		False	False	10.227	0.003
95		False	False	9.881	0.003
96		False	False	10.603	0.003
97		False	False	10.021	0.003
98		False	False	10.147	0.003
99		False	False	10.702	0.003
100		False	False	10.213	0.003
101		False	False	9.83	0.003
102		False	False	8.173	0.003
103		False	False	10.874	0.003
104		False	False	13.71	0.008
105		False	False	11.963	0.003
106		False	False	11.526	0.003
107		False	False	12.557	0.004
108		False	False	13.104	0.003
109		False	False	11.912	0.003
110		False	False	12.833	0.003
111		False	False	11.694	0.003
112		False	False	15.146	0.003
113		False	False	11.48	0.003
114		False	False	7.324	0.003
115		False	False	10.076	0.003
116		False	False	13.36	0.005
117		False	False	10.71	0.003

Table A.1.: Columns 71-75

ID	BPmag	e_BPmag	RPmag	e_RPmag	BP-RP
	(mag)	(mag)	(mag)	(mag)	(mag)
0	21.258	0.189	18.331	0.021	2.927
1	5.626	0.003	5.041	0.004	0.585
2	18.837	0.027	15.123	0.005	3.714
3	21.279	0.17	17.614	0.014	3.665
4	18.556	0.035	14.838	0.011	3.718
5	16.2	0.005	13.032	0.004	3.168
6	8.516	0.003	7.852	0.004	0.664
7	14.38	0.012	11.69	0.007	2.69
8	9.313	0.006	8.323	0.005	0.99
9	16.072	0.006	13.025	0.004	3.047
10	7.542	0.003	7.057	0.004	0.485
11	9.292	0.006	8.21	0.006	1.082
12	13.503	0.005	11.425	0.004	2.078
13	21.222	0.159	17.021	0.009	4.201
14	15.03	0.006	12.243	0.004	2.787

Continued on next page

ID	BPmag (mag)	e_BPmag (mag)	RPmag (mag)	e_RPmag (mag)	BP-RP (mag)
15	9.383	0.009	8.442	0.007	0.94
16	16.189	0.005	13.347	0.004	2.842
17	21.317	0.095	17.269	0.011	4.047
18	10.295	0.006	9.104	0.006	1.191
19	17.932	0.014	14.593	0.005	3.339
20	15.952	0.004	13.159	0.004	2.793
21	17.099	0.005	14.036	0.004	3.064
22	15.509	0.005	12.624	0.004	2.885
23	16.03	0.005	12.896	0.004	3.135
24	13.463	0.003	11.536	0.004	1.927
25	17.858	0.015	14.436	0.004	3.421
26	13.824	0.005	11.471	0.004	2.353
27	13.774	0.006	11.48	0.005	2.294
28	18.456	0.025	14.82	0.004	3.636
29	17.789	0.009	14.464	0.005	3.325
30	16.543	0.005	13.548	0.004	2.995
31	17.782	0.012	14.381	0.004	3.4
32	17.44	0.007	13.991	0.004	3.449
33	18.364	0.011	14.782	0.004	3.582
34	6.673	0.003	6.489	0.004	0.184
35	21.243	0.148	17.149	0.008	4.094
36	17.076	0.007	14.023	0.004	3.053
37	18.404	0.016	14.674	0.004	3.73
38	17.514	0.008	14.321	0.004	3.193
39	16.572	0.006	13.359	0.004	3.213
40	17.629	0.008	14.33	0.004	3.299
41	17.91	0.011	14.604	0.004	3.306
42	18.043	0.015	14.362	0.004	3.682
43	15.596	0.006	12.729	0.004	2.867
44	15.632	0.005	12.75	0.004	2.882
45	21.611	0.144	18.257	0.019	3.354
46	16.155	0.005	13.117	0.004	3.038
47	17.61	0.015	14.305	0.005	3.305
48	14.464	0.01	12.049	0.006	2.415
49	5.842	0.003	5.871	0.004	-0.029
50	14.646	0.006	11.487	0.004	3.159
51	21.663	0.329	19.223	0.043	2.441
52	10.183	0.005	9.141	0.005	1.041
53	14.831	0.005	12.207	0.004	2.624
54	17.007	0.007	13.783	0.004	3.224
55	15.532	0.004	12.756	0.004	2.776
56	16.109	0.005	13.159	0.004	2.95
57	15.743	0.008	12.612	0.005	3.131
58	14.934	0.007	12.25	0.005	2.684
59	15.937	0.005	13.05	0.004	2.887
60	20.367	0.271	17.952	0.032	2.415
61	16.072	0.004	13.214	0.004	2.858
62	4.455	0.003	4.528	0.005	-0.073
63	18.869	0.019	15.054	0.006	3.815
64	16.075	0.008	13.138	0.005	2.936
65	19.637	0.032	15.728	0.004	3.908
66	14.992	0.036	12.438	0.028	2.554
67	15.876	0.005	12.998	0.004	2.878
68	11.072	0.003	9.933	0.004	1.139
69	15.909	0.007	12.977	0.005	2.932
70	16.263	0.008	13.337	0.005	2.926
71	13.838	0.007	11.279	0.005	2.559
72	15.555	0.004	12.548	0.004	3.007
73	10.035	0.008	8.765	0.006	1.271
74	17.515	0.008	14.144	0.004	3.371
75	16.821	0.007	13.498	0.004	3.323
76	14.989	0.01	12.139	0.006	2.85
77	15.33	0.005	12.327	0.004	3.003
78	15.105	0.004	12.347	0.004	2.758
79	15.51	0.006	12.651	0.004	2.859
80	16.529	0.004	13.46	0.004	3.069
81	21.066	0.119	16.259	0.006	4.807
82	15.76	0.006	12.887	0.004	2.873
83	13.52	0.011	11.164	0.007	2.356
84	21.789	0.237	18.403	0.02	3.386
85	7.568	0.003	7.051	0.01	0.517
86	9.365	0.32	8.561	0.026	0.804
87	10.803	0.005	9.829	0.005	0.974
88	10.038	0.005	9.188	0.005	0.85
89	11.126	0.007	10.098	0.006	1.029
90	10.547	0.005	9.738	0.005	0.809
91	10.765	0.005	9.824	0.005	0.941
92	10.96	0.006	9.977	0.005	0.983

Continued on next page

ID	BPmag (mag)	e_BPmag (mag)	RPmag (mag)	e_RPmag (mag)	BP-RP (mag)
93	11.98	0.007	10.824	0.006	1.156
94	10.594	0.006	9.688	0.005	0.906
95	10.218	0.008	9.373	0.006	0.845
96	10.959	0.005	10.073	0.005	0.886
97	10.404	0.004	9.471	0.004	0.932
98	10.532	0.004	9.583	0.004	0.95
99	11.12	0.006	10.106	0.005	1.013
100	10.583	0.005	9.671	0.005	0.912
101	10.492	0.004	9.04	0.004	1.452
102	8.402	0.003	7.784	0.004	0.618
103	11.643	0.005	10.008	0.005	1.635
104	14.544	0.011	11.942	0.006	2.601
105	12.885	0.004	11.005	0.004	1.879
106	12.365	0.006	10.615	0.005	1.751
107	13.577	0.009	11.548	0.006	2.029
108	14.782	0.006	11.858	0.005	2.924
109	12.835	0.005	10.885	0.004	1.949
110	14.324	0.004	11.636	0.004	2.688
111	12.812	0.008	10.64	0.006	2.171
112	17.451	0.007	13.772	0.004	3.679
113	12.427	0.007	10.514	0.006	1.913
114	7.429	0.003	7.111	0.004	0.318
115	10.439	0.005	9.552	0.005	0.887
116	14.041	0.015	11.475	0.009	2.565
117	11.628	0.004	9.763	0.004	1.866